HYDRODYNAMIC INTERACTIONS OF AN UNMANNED UNDERWATER VEHICLE OPERATING IN CLOSE PROXIMITY TO A MOVING SUBMARINE

by

Brady M. Hammond

M.S. Mechanical Engineering
Georgia Institute of Technology, 2017

B.S. Mechanical Engineering
Utah State University, 2013

Submitted to the Department of Mechanical Engineering and the System Design and Management Program in partial fulfillment of the requirements for the degrees of

Naval Engineer

and

Master of Science in Engineering and Management

at the

Massachusetts Institute of Technology

June 2021

Author….……...……...
Department of Mechanical Engineering
June 4, 2021

Certified by....…….…….
Themistoklis Sapsis
Associate Professor of Mechanical Engineering
Thesis Supervisor

Accepted by……..……...
Joan S. Rubin
Executive Director, System Design and Management

Accepted by……..……...
Nicolas Hadjiconstantinou
Chairman, Committee on Graduate Students

THIS PAGE INTENTIONALLY LEFT BLANK

HYDRODYNAMIC INTERACTIONS OF AN UNMANNED UNDERWATER VEHICLE OPERATING IN CLOSE PROXIMITY TO A MOVING SUBMARINE

by

Brady M. Hammond

Submitted to the Department of Mechanical Engineering
on May 14th, 2021, in partial fulfillment of the
requirements for the degrees of
Naval Engineer
and
Master of Science in Engineering and Management

Abstract

While the United States Navy has developed a strong arsenal of tools to model the hydrodynamic forces and moments of different vehicles in different conditions, they do not have a model that enables them to understand the forces and moments that an Unmanned Underwater Vehicle (UUV) experiences when operating in close proximity to a moving submarine as a result of the interactions between their potential fields and wakes. The launch and recovery of UUVs from submarines is very challenging because these hydrodynamic interactions make UUVs hard to control near submarines and my even cause collisions between the two vehicles. The mapping of these forces and moments is vital to simulate the motion of the vehicles and enable developers to create UUV control and autonomy systems that are adaptive to these hydrodynamic interactions to further enable UUV launch and recovery. Due to the complex nature of the hydrodynamic interactions, this study used computational fluid dynamics to expand the current understanding of the forces and moments between these two vehicles. A Gaussian process regression model was used to perform an optimal experimental design and map the resulting hydrodynamic interactions based on the UUVs longitudinal position, lateral position, speed, heading angle, UUV diameter, and UUV length. The model was validated using an out of sampling method and was shown to be capable of accurately predicting the hydrodynamic interactions between a submarine and UUV.

Thesis Supervisor: Themistoklis Sapsis

Title: Associate Professor of Mechanical Engineering

THIS PAGE INTENTIONALLY LEFT BLANK

Acknowledgments

I am truly grateful for the opportunity to pursue my Master's Degree at the Massachusetts Institute of Technology. I am so amazed by the brilliant achievements and selfless work ethic of people that have mentored me and worked alongside me throughout my time at MIT. Serving in the United States Navy has been one of the greatest honors of my life. I feel so blessed that I was given the opportunity to join the Naval Construction and Engineering program and join this amazing cohort.

First, I wish to thank my advisor Themistoklis Sapsis. His guidance and mentorship have been invaluable. I have no idea how one person can have such an expertise in so many different fields. Because this thesis bridged many topics, his knowledge was vital to the completion of this study.

I would also like to extend a special thanks to the following individuals.

- James B. (Burke) Murray – As the head of the Hydrodynamics and Maneuvering Simulation Branch (Code 862) of the Naval Surface Warfare Center and project sponsor, Burke identified the original need for the study and was instrumental in identifying the best ways in which the project could be carried out.
- Matthew Hait – Matt is a fellow 2N student who spent a great deal of time and resources in teaching me about CFD software, familiarizing me with industry standards, and providing me with the resources to be able to perform the simulations.
- Jose del Aguila Ferrandis – Jose played an integral role in setting me up with Star-CCM+ software and training me on its functionality.
- Antoine Blanchard – As the co-author of the GPsearch code, Antoine was essential in modifying the code to be able to meet the specific needs of this project. Without his selfless efforts, this study would not have been successful.
- Bart Paul Gerard Van Parys – Bart provided expert consultation and advice on the nonlinear optimization methods that were explored to create the parametric model.

Most importantly, I wish to thank my loving wife Jackie. The unwavering love, support, and commitment that she has given me has been the enabling power to allow me to pursue my dreams. There is no way I could have done this without her and am so grateful for her wonderful example, friendship, and strength.

THIS PAGE INTENTIONALLY LEFT BLANK

Table of Contents

THIS PAGE INTENTIONALLY LEFT BLANK

List of Figures

THIS PAGE INTENTIONALLY LEFT BLANK

List of Tables

THIS PAGE INTENTIONALLY LEFT BLANK

Abbreviations

AMC	Australian Maritime College
ASW	Anti-Submarine Warfare
AUV	Autonomous Underwater Vehicle
BSLRSM	Baseline Reynolds Stress Model
CFD	Computational Fluid Dynamics
CN3	Communication/Navigation Network Nodes
DARPA	Defense Advanced Research Projects Agency
DOE	Design of Experiments
DOF	Degree of Freedom
DSTO	Defense, Science, and Technology Organization
EFD	Experimental Fluid Dynamics
GP	Gaussian Process
ID	Identification
IO	Information Operations
ISE	International Submarine Engineering
ISR	Intelligence, Surveillance, and Reconnaissance
ITTC	International Towing Tank Conference
L&R	Launch and Recovery
MCM	Mine Countermeasures
NCMEH	National Centre for Maritime Engineering and Hydrodynamics
OED	Optimal Experimental Design
PMS 406	Unmanned Maritime Systems Program Office
RANS	Reynolds-averaged Navier–Stokes
SE	Squared Exponential
SST	Shear-Stress Transport
TCS	Time Critical Strike
UUV	Unmanned Underwater Vehicle
VPT	Virginia Payload Tube

Nomenclature

C_p	Coefficient of Pressure
D	Diameter
L	Length
K	Rolling Moment
M	Pitching Moment
MAE	Mean Absolute Error
MAPE	Mean Absolute Percent Error
N	Yawing Moment
N’	Yawing Moment Coefficient
R	Radius
R_{Lat}	Latitudinal Separation Ratio
R_{Long}	Longitudinal Separation Ratio
Re	Reynolds Number
U	Velocity
X	Surge Force
X’	Surge Force Coefficient
x	Distance in the x-direction
Y	Sway Force
Y’	Sway Force Coefficient
y	Distance in the y-direction
y^+	Non-dimensional Wall Distance
Z	Heave Force
$\Delta\delta_{eq,Y}$	Sway Equivalent Rudder Angle Difference
$\Delta\delta_{eq,N}$	Yaw Equivalent Rudder Angle Difference
μ	Dynamic Viscosity
ρ	Density
ϕ	Heading Angle
% X_{prop}	Percent of Propulsive Force

Chapter 1

1 Introduction

While the U.S. Navy has developed a strong arsenal of tools to model the hydrodynamic forces of different vehicles in different conditions, they do not have a model that enables them to understand the forces an Unmanned Underwater Vehicle (UUV) will experience when in close proximity to a moving submarine as a result of the interactions between their wakes and pressure fields. The goal of this thesis is to expand current understanding of the hydrodynamic forces and moments between these two submerged moving bodies. The mapping of these forces and moments at various positions, angles, speeds, and vehicle sizes is vital to simulate the motion of the two submerged bodies in close proximity. This thesis attempts to model these forces and moments to enable the future simulation of a UUV maneuvering in close proximity to a submarine.

1.1 Background

In 2000, the U.S. Navy released its Unmanned Undersea Vehicle Master Plan and provided updates in 2004 and 2011. This plan stressed the importance of UUVs and their capability to "continually demonstrate new possibilities that can assist our naval forces maintain maritime superiority around the world."[1] UUVs are being incorporated into the fleet because they have potential capability in nine different mission areas (or UUV "Sub-Pillars") including Intelligence, Surveillance, and Reconnaissance (ISR), Mine Countermeasures (MCM), Anti-Submarine Warfare (ASW), Inspection/Identification (ID), Oceanography, Communication/Navigation Network Nodes (CN3), Payload Delivery, Information Operations (IO), and Time Critical Strike (TCS) [1].

Due to their ability to avoid detection, submarines provide an opportune platform for the launch and recovery (L&R) of UUVs. Because of their large draft and nonexpendable nature, submarines cannot operate in littoral waters off an adversary's coastline as well as UUVs. By integrating submarines and UUVs, the UUVs can take on certain mission sets of submarines and act as force multipliers and risk reducers to manned platforms, especially in littoral waters [1]. The expertise

of the submarine crew involving underwater and covert operations is valuable to the deployment of UUVs. Submarine operational time is in high demand and enabling UUVs to accomplish certain submarine tasks will provide the submarine with flexibility and time to perform other tasks or mission sets [1]. In order to integrate submarines and UUVs, many different L&R systems have been explored to provide this new capability.

UUVs are available in four different classes. These classes are outlined in the UUV Master Plan and further expanded upon by the Unmanned Maritime Systems Program Office (PMS 406) [1], [2]. The following table describes different features of these different UUV classes.

Table 1: UUV Classification [1], [2]

UUV Master Plan Class	PMS 406 Class	Diameter (in)	Displacement (lbs)
Man-Portable	**Small or Man-Portable**	3 to 10	25 to 100
Light Weight Vehicle (LWV)	**Medium**	10 to 12.75	~500
Heavy Weight Vehicle (HWV)	**Medium**	12.75 to 21	~3000
Large	**Large**	21 to 84	~ 20,000
N/A	**Extra Large**	>84	N/A

Different classes of UUV are capable of performing different mission sets. Allowing submarines to launch and recover different size UUVs enables them to accomplish a wider variety of mission. The following table illustrates the potential mission sets that each UUV class is capable of performing. These missions are prioritized based on the importance to the Navy.

Table 2: UUV Classes vs. Mission Sets [1]

Mission Set	Priority	Man-Portable	LWV	HWV	Large
ISR	1	Special Purpose	Harbor	Tactical	Persistent
Oceanography	5	-	Special Purpose	Littoral Access	Long Range
CN3	6	Very Shallow Water/Special Operations Forces	Mobile CN3	-	-
MCM	2	(Very) Shallow Water, Search, Classify, Map, Neutralizers	Operating Area Clearance	Clandestine Reconnaissance	-
ASW	3	-	-	-	Hold-at-Risk

Inspection/ID	4	Homeland Defense/ Anti-Terrorism Force Protection	-	-	-
Payload Delivery	7	-	-	-	Special Operations Forces, ASW, MCM, TCS
IO	8	-	Network Attack	Submarine Decoy	-
TCS	9	-	-	-	Deliver Ordinance

To successfully launch and recover UUVs from submarines, these two vehicles will be operating in very close proximity to each other. The flow around the submarine and UUV in close proximity will be different than if the two vehicles are far apart. The wake, pressure field, and boundary layer created by the submarine will interact with the UUV as illustrated in the figure below.

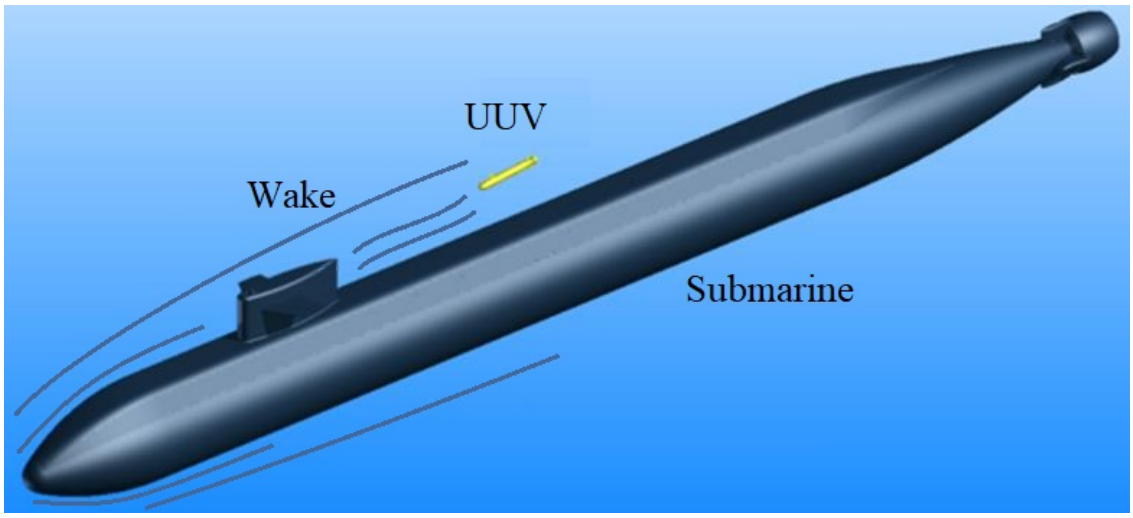

Figure 1: Submarine and UUV interactions [3]

The interactions between the submarine and UUV create forces and moments which may result in uncontrollable vehicle motions and create a challenge for the precise vehicle control required for the L&R of UUVs [4]. Because the UUV is much smaller that the submarine, the UUV would be affected much more by these unwanted forces and moments. Understanding the hydrodynamic interactions between these two vehicles will enable the Navy to better model UUV L&R methods, develop better UUV control systems, and provide them with additional insight when designing different UUV L&R architectures.

Many different UUV L&R systems have been explored. Each technique has its advantages and disadvantages. Some of these L&R system concepts include [3]–[6]:

- Deployment and Recovery via Conventional Torpedo Tubes
- Deployment and Recovery via Enlarged Torpedo Tubes
- Deployment and Recovery via Existing Missile Tubes
- Deployment and Recovery via a Dry Casing Mounted Hanger
- Deployment and Recovery via a "Wet" Casing Mounted Hangar
- Deployment and Recovery via AUV Bespoke Multiple Hangars
- Deployment and Recovery via Docking Envelopes
- Deployment and Recovery via Mechanically Actuated Submarine Mechanisms

These many different potential L&R systems each require the UUV to be in a unique position. Understanding the hydrodynamic interactions of the UUV in any location with respect to the submarine is very valuable because it allows decision makers to assess the feasibility and risk of each L&R system.

1.2 Hydrodynamic Interactions Between Two Bodies

While the hydrodynamic forces acting on a single moving submarine or UUV are well known, there are few studies in the public domain that examine the effect of the forces and moments due to the hydrodynamic interactions between a submarine and UUV operating in close proximity. As a UUV travels close to a moving submarine, the submarine's pressure field and wake cause the UUV to experience unwanted external forces and moments which make the UUV have undesirable motions and may even cause the UUV to become uncontrollable [3]. This could result in L&R failure or even a collision between the two vessels. These external forces and moments acting on the vessels operating in close proximity are known as hydrodynamic interactions. There have been many studies that investigated the hydrodynamic interactions between surface ships, but these results only minimally apply to submarines and UUVs due to their greater six degrees of freedom (DOF) motion. Due to this added complexity, the hydrodynamic interactions between submarines and UUVs have not been researched or experimentally determined as much as they have between surface ships.

Of the few studies that have been conducted, there have been a few different approaches to model these hydrodynamic interactions. One study modeled the behavior of a Phoenix Autonomous Underwater Vehicle (AUV) docking into a retractable recovery tube on a Los Angeles submarine [5]. This study assumed that the submarine was large enough with respect to the UUV to appear as a flat plate and also neglected the viscous friction drag acting on the submarine. The approach used Prandtl's boundary layer theory over a flat plat to model the parabolically shaped boundary layer along the submarine hull. Within this boundary layer, the UUV would experience a reduction in fluid velocity caused by the viscous effects of the fluid acting on the hull. While this approach was one of the first to model the UUV maneuverability near a moving submarine, the model's simplicity fails to capture the complexity needed to more accurately predict the behavior of the UUV. This approach neglects the effect of the submarine wake and potential field, which will exert forces on the UUV. Additionally, whether pressure drag or viscous drag dominates primarily depends on the length to diameter (L/D) ratio of the submarine [6]–[8]. Submarines are designed to minimize their total drag. This is a combination of their pressure drag, caused by wake formation and boundary layer separation, and their viscous drag, caused by the fluid friction on the submarine's wetted surface. The following figure shows how pressure and viscous drag are impacted by L/D.

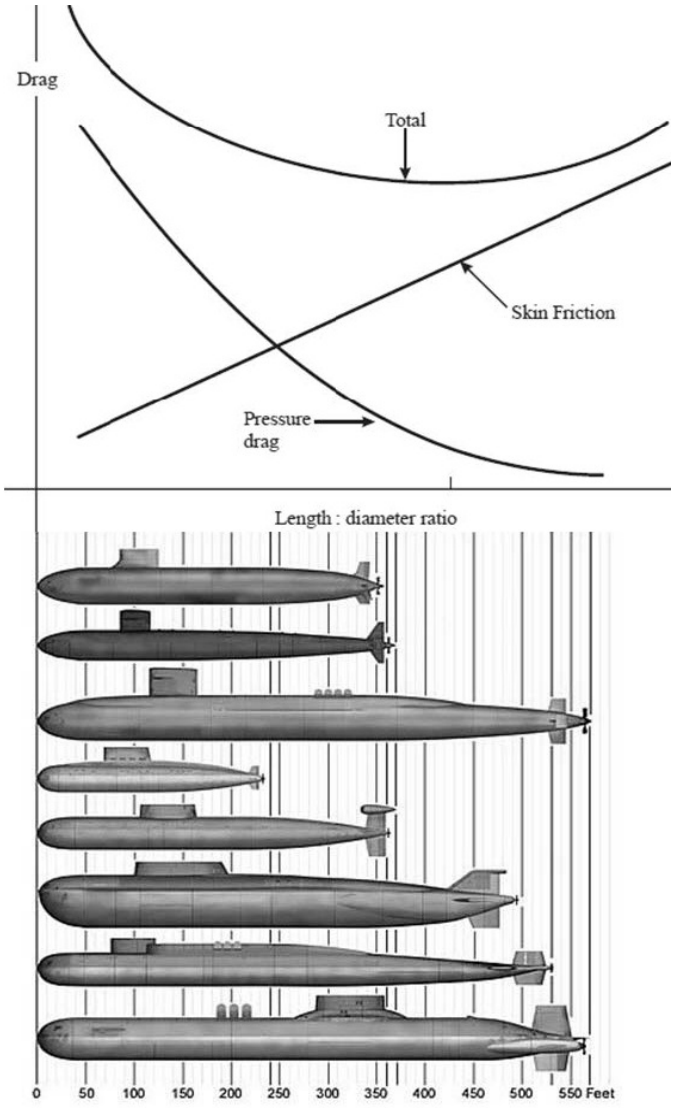

Figure 2: Optimal Submarine L/D and Various Platforms [6]

For the platforms under consideration, viscous drag should not be neglected. Also, the optimal L/D is determined for a given speed, typically the endurance speed or maximum speed. The L&R of UUVs from submarines is being investigated at much lower speeds than the endurance or maximum speed. These lower speeds result in a lower Reynold's numbers and will cause the viscous drag to be even more significant compared to the pressure drag [9].

Another approach to the problem was conducted in a study that created a partially-fixed parametric model of the hydrodynamic interaction forces and moments based on both potential theory and experimentally derived models available in the literature [10]. Much of the data was taken from the better-known interactions between surface ships and applied to submarines and UUVs.

Because the model was partially created from experimental models and validated against other data within these models, it is considered accurate for its indented use. However, due to the limited nature of the available experimental models, the results are limited to specific scenarios. The model does not have the broad level applicability to create maneuvering simulations for all of the scenarios of interest to the Navy.

An additional study investigated the hydrodynamic interactions on a UUV at a various positions relative to the sail of a moving submarine to determine which locations would allow for the best L&R of a UUV [11]. Computational Fluid Dynamics (CFD) was used to determine the hydrodynamic interactions. The study found that in the forward region of the submarine, the hydrodynamic interactions cause the UUV to be repelled and the magnitude of the force increased as the vehicles moved closer together. When the UUV was parallel and adjacent to the sail or cylindrical body, the UUV would experience attraction forces between the two vessels. This was caused by the Bernoulli effect of the flow velocity increase between the submarine and UUV. The study also found that vortices were generated by the sail which caused fluctuations in the forces. Since the scope of study was narrow in the locations and vessel diameters that it investigated, the results of this study need to be expanded and more experiments performed to be able to simulate UUV control at all areas of interest around a submarine.

All of the studies listed above provided novel incremental insights on how a UUV acts in close proximity to a submarine. However, they were limited in their breadth of variations of the relative speed, longitudinal position, lateral position, and size difference between the two vehicles. This greatly limits their applicability to a generalized maneuvering simulation of a UUV near a moving submarine. Additionally, they lacked physical experiments between two submerged bodies to validate their models.

A pioneering study initiated and partially funded by the Defense, Science and Technology Organization (DSTO) and the National Centre for Maritime Engineering and Hydrodynamics (NCMEH) at the Australian Maritime College (AMC) was able to make great progress in both areas that the other studies lacked [3]. The investigation examined the effects of the hydrodynamic forces and moments on an unappended UUV as a function of the relative speed, longitudinal position, lateral position, and size difference with respect to an unappended submarine. The work

involved the development of CFD models to simulate the hydrodynamic interactions and map the resulting forces and moments. This study also conducted tow tank experiments with two submerged bodies and used the results to validate its computational models. While this examination was much more extensive than previous studies, different length to diameter ratios and different incident angles need to be further examined to fully understand the effects of the hydrodynamic interactions to enable the simulation of the maneuvering UUV in close proximity to the submarine.

1.3 Computational Fluid Dynamics

1.3.1 Motivation

There are multiple different ways to determine the hydrodynamic forces and moments acting on moving bodies. These approaches include analytical solutions to the Navier-Stokes equations, experimentation and empirical solutions, and computational fluid dynamics (CFD). Analytical solutions to the Navier-Stokes equations are very limited. In certain geometries and applications, this set of coupled non-linear partial differential equations can be simplified and used to get exact solutions. However, a general smooth solution to the three-dimensional incompressible Navier-Stokes equations does not exist and remains one of the seven most important open problems in mathematics [12]. The geometry of this specific problem is too complicated to reach an analytical solution to the Navier-Stokes equations.

The second potential approach is to use experimental fluid dynamics (EFD) to determine the forces and moments of a UUV interacting with a moving submarine. Because this approach collects force data from physical models, usually in a tow tank, the results are generally considered valid. They often eliminate errors in computational models that exist from not capturing the real complexity of the physical world [13]. However, performing physical experiments is both challenging and expensive. In order to experimentally determine the forces and moments experienced by the submarine and UUV, the methods used on surface ships need to be upgraded to capture the 6-DOF motion capable by submerged vehicles [4], [14]. When the effects on multiple vehicles are being studied, the instrumentation and infrastructure needed increases significantly. Additionally, the facilities required to capture the range of variables studied in this experiment pose as a large obstacle. In order to have the experimental model be unaffected by the restricted water effect, the

model needs to be small enough to fit in a tow tank and allow water to flow around it without having changes in the pressure and velocity field around the hull due to the tow tank walls and bottom [15]–[17]. However, the model needs to be as large as possible to better capture the full-scale physics and reduce EFD uncertainty. For straight line tests, the ratio of the model length to tank width ratio should be 0.47 [17]. Arguments have been made this this is too large for submerged vehicles due to the proximity to the bottom of the tank, but this number will be used to illustrate the concept [15]. Models can be slightly bigger, but corrections need to be made and errors can be introduced due to blockage effects [16]. According to this model length to tank width ratio, a 2.43 meter (8 foot) wide tow tank should have a model roughly 1.15 meters long. If the submarine being modeled is an Ohio class submarine and the UUV being modeled is a 3 inch man-portable UUV, then the submarine model would need to be about 8.6 cm in diameter. To maintain the same diameter ratio between the submarine and UUV of 168, this mean the UUV model would need to be about 0.5 mm in diameter [18]. It is completely unrealistic to collect any usable data with a UUV model this small. Even if a medium or large UUV was modeled, rather than a man-portable, this would still require the model diameters to be 3.6 mm and 14 mm respectively. These have submarine to UUV diameter ratios of 24 and 6 respectively. These ratios produce model sizes that are too small to produce any good data. In a novel study that performed EFD to validate the hydrodynamic interactions between submarines and UUVs, the diameter ratio between submarine and UUV was limited to 2.239 due to the previously discussed limitations on the model sizes with respect to the size of the tow tank facility [3]. Even at this extreme diameter ratio, blockage effects were still experienced in the EFD results. This is why the facilities often drastically limit the range of submarine and UUV sizes that can be studied.

The third approach that can be taken to study the hydrodynamic interactions between a submarine and UUV operation in close proximity is to use CFD. CFD uses computers to simulate the desired physical conditions. This approach is capable of accurately prediction fluid velocities and pressures at any point in within the volume of interest and use this information to determine the forces and moments experienced by objects in the flow field. By using computer simulations, rather than physical models, there is virtually no limit to the model sizes and geometries that can be studied. Also, changing CFD models is much faster and cheaper than changing physical models.

Simulations can also be run at full scale sizes to remove complications of trying to match Reynolds and Froude numbers in physical model testing [19].

There are a wide variety of different discretization methods, turbulence models, and solution algorithms that can be applied when using CFD, and they can yield different results. For this reason, verification and validation of CFD is very important. Verification is the process of determining if a CFD simulation can accurately represent exact known analytical solutions while validation is determining if the simulation agrees with physical reality [20]. Verification is often described as “solving the equations right” while validation is described as "solving the right equations". There are many different methods and models within CFD that have been verified as accurate. However, when using these verified methods, it is important to validate simulations whenever possible to ensure that these verified models are being applied correctly to accurately reflect what happens in the real world. For this reason, the determining factor for which verified method should be used was based on which method most accurately matched the physical EFD results.

1.3.2 Grid

Because the non-linear partial differential Navier-Stokes equations cannot be solved directly in three dimensions, CFD discretizes the solution space into a grid and iterates through solutions until it converges and all points in the grid satisfy the governing equations and boundary conditions. By having a more refined and higher grid resolution, the simulation will more accurately capture the real word physics. However, increasing the grid resolution also increases the time that it takes for a solution to converge. Therefore, accuracy and computation time are two competing parameters in CFD and finding a balance between them is vital. This balance allows a study to be both accurate and quick enough to allow time for a larger number of simulations. Additionally, maintaining orthogonality of the grid at it’s boundary is recommended and even mandatory for some CFD solvers [21].

A study was conducted that validated CFD accuracy against EFD data in six different naval applications, including a bare submarine hull [22]. The CFD simulations were performed with a different number of grid cells to determine the impact that the grid resolution has on the accuracy

of the simulation. The following figure plots the pressure component of the yawing moment of a submarine hull at an 18º drift angle and a Reynold's number of $1.4x10^7$ against the number of cells in the CFD grid. Each data point in the CFD series is plotted with two percent error bars.

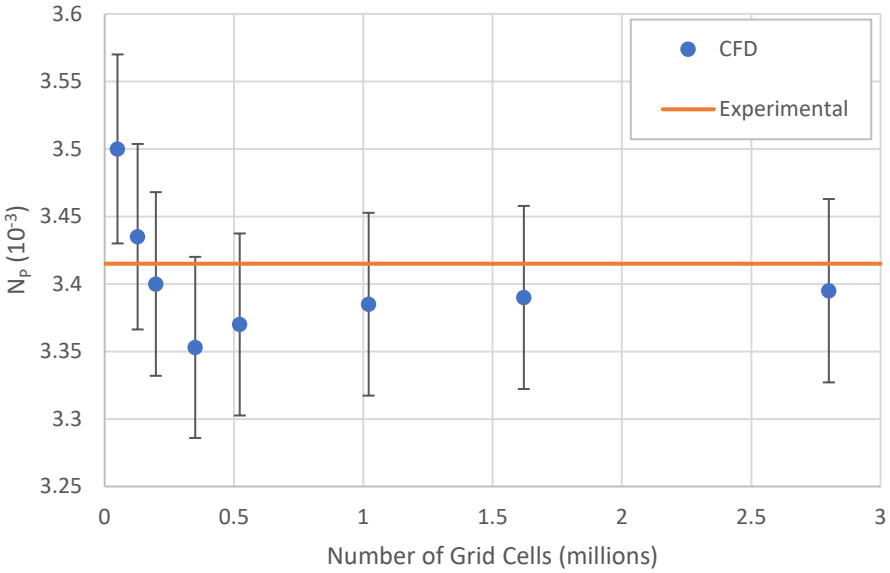

Figure 3: Comparison of Number of Grid Cells to CFD Yawing moment Accuracy for Submarine Hull [22], [23]

Overall, even relatively coarse meshes of a few hundred thousand cells were able to accurately predict the yawing moment to within two percent of the EFD results. The only simulation which had an error greater than two percent was the coarsest grid which only contained 50,000 cells. Even this grid was had an error of about 2.5%, which is still very small for practical applications. The study concluded that using highly-refined, block-structured grids, good iterative convergence, and modest inflow angles consistently yielded errors within 5% of the global EFD quantities such as force and moment coefficients. This was consistent for all of the different naval applications that were studied, although the minimum number of cells in the other applications in the study were higher [22].

Another study found slightly different results on the accuracy of the number of CFD grid cells for a bare submarine hull [24]. A simulation was run at seven different grid resolutions and validated against EFD data. In the figure below, each CFD data point is shown with a five percent uncertainty.

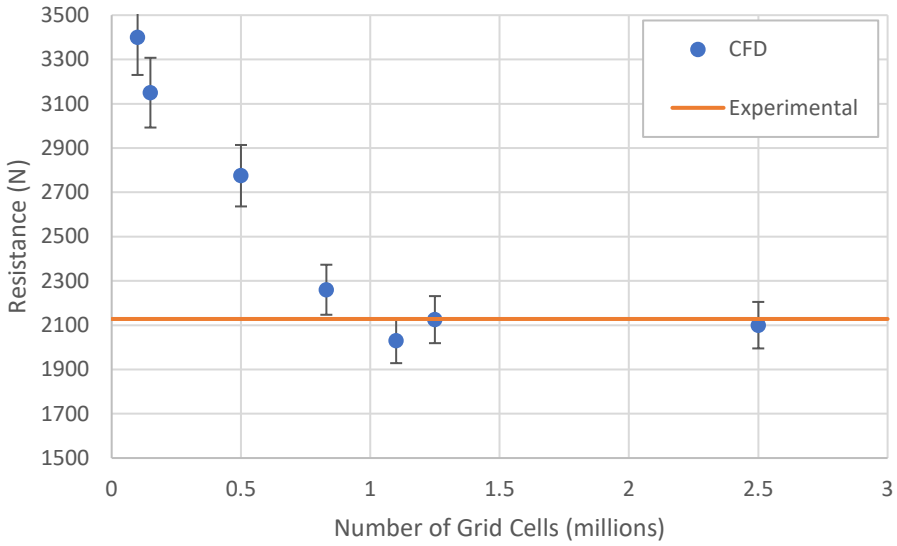

Figure 4: Comparison of Number of Grid Cells to CFD Resistance Accuracy for Submarine Hull [24]

This study concluded that grids with less than about 1.1 million cells were not accurate enough to be considered valid. The accuracy of the coarse grid resolution in the previous study may be true in that specific simulation and may not be universally applicable to other simulations. While these two studies are not in complete agreement, both agree that grid sizes of at least 1.1 million cells are likely to produce more accurate and valid results for any application. An additional CFD study on the bow shapes of submarines reached a very similar conclusion. The meshes with fewer cells were inaccurate and that the results became accurate and independent of meshing resolution after the grid reached 1.2 million cells [25]. As such, this criterion will be considered for this thesis.

1.3.3 Near Wall Turbulence Modeling

Another important parameter to consider during CFD simulation is how to model the turbulence near the boundary of the object being studied. This is especially important to determine the viscous drag on an object, which is very relevant to this study. Because turbulence is very erratic, many CFD solvers use the Reynolds-averaged Navier–Stokes (RANS) equations to take a time-average of the fluctuating quantities to make turbulence modeling more manageable. There are many different approaches to model this phenomenon but they can generally be separated into two categories, near wall modeling and wall functions. Near wall turbulence models resolve the flow at each point along the boundary while wall functions use a semi-empirical formula to determine a solution without actually resolving the flow in along the boundary [21], [26]. A non-dimensional

wall distance, known as y^+, establishes a way to measure and compare the grid resolution near the boundary of an object. Near wall modeling uses a very fine mesh to more accurately capture the laminar sub-layer and predict the values of viscous drag on the body. This near wall approach typically uses a two-equation eddy-viscosity turbulence models like the popular k-ω turbulence model. This model uses two equations to model the effects of turbulence near the boundary, one for the turbulence kinetic energy (k), and the other for its dissipation rate (ω). This approach is generally considered more accurate than using a wall function because it can better resolve the boundary layer to capture the shear stress on the wall of the object to determine the viscous drag. However, creating a fine grid near the wall greatly increases the time required to perform the simulation.

The other approach is to use wall functions to determine pressure and velocity profile along the boundary of an object. This approach typically uses k-ε turbulence model, which has a different equation for the dissipation rate than the k-ω model. This approach allows a grid that is coarser and can be solved faster. However, the semi-empirical formula used by wall functions are based on zero pressure gradients along flat plates and become less accurate when dealing with adverse pressure gradients, like those experienced on the stern of submarines and UUVs [21], [26]. The following table outlines the criteria for these two approaches.

Table 3: Near Wall and Wall Function Criteria [21]

	First Point	Expansion Ratio	Boundary Layer Points
Near wall	$y^+ \leq 1$	1.2	20
Wall Functions	$30 < y^+ < 100$	1.2	15

Because both of these approaches have been verified against numerical solutions, the best way to determine their accuracy is to validate them against EFD data.

One study was performed to determine the resistance on bare hull submarines. It used the k-ε turbulence model and a y^+ equal to 30 to calculate the resistance of multiple difference hull shapes [24]. This approach was considered valid because the CFD predictions were within a few percent of the EFD data, which is within reason for the application at hand. In this application, the adverse

pressure gradient did not have a negative impact on the results. An additional study involving the simulation of microbubble resistance reduction on the Defense Advanced Research Projects Agency (DARPA) SUBOFF hull also validated CFD models against EFD data [27]. In this study, the k-ε turbulence model was used and the y^+ value varied between about 30 to 70 at every point along the wall. This grid also contained approximately 1.1 million cells. The CFD predicted forces were very close to the experimental data so the results were considered valid.

A new turbulence model, known as k-ω Shear-Stress Transport (SST) model, was developed to try and capture the benefits of both approaches [26]. The k-ω SST turbulence model approximates the k-ε model to account for the free shear layers as it approaches the boundary layer edge. Closer to the wall, the model applies an additional equation to the k-ω model to account for the transport of the principal turbulent shear stress in adverse pressure gradient boundary layers. This reduces the errors caused by the adverse pressure gradient that exist with k-ε model. Because this model transitions from a near wall approach to approximating a wall function, the y^+ value can be in either of the ranges because the model takes care of it. Although this model has its benefits, it still takes more computational time than the k-ε model. A range of studies have validated the k-ω SST turbulence model when simulating the forces on a submarine [28]–[30]. These studies had refined grids near the boundary layer with a $y^+ < 1$ in accordance with the International Towing Tank Conference (ITTC) recommendations [21]. Additionally, studies have compared the performance of the k-ω SST model and the k-ε model on submarine hulls and determined that they are both valid based on EFD results [28], [29]. One study concluded that there is an agreement between experimental results and all of the studied RANS turbulence models for drift angles less than 10 degrees [28].

All of the studies mentioned above only involved one vehicle rather than the hydrodynamic interactions between two vehicles. One novel study performed both CFD simulations and EFD validation to determine the hydrodynamic interactions between a submarine and UUV [3], [31]. In this study, the turbulence model that was used was the Baseline Reynolds Stress Model (BSLRSM). Previous CFD and EFD work on the SUBOFF model by the same author showed the BSLRSM was more accurate than two-equation eddy-viscosity turbulence models, including the k-ε, k-ω, and k-ω SST models. This was because the BSLRSM is the most complete classical

turbulence model. The two-equation eddy-viscosity turbulence models struggled to mimic complex engineering flows involving rotational flow, flow separation, and flows that are strongly anisotropic because they are limited by the eddy-viscosity hypothesis. For this reason, the BSLRSM was used to model the hydrodynamic interactions between a submarine and UUV. This approach was determined to be valid because it accurately reflected the EFD results.

1.4 Optimal Experimental Design

In order to simulate the complex and diverse maneuverability space of a UUV in close proximity to a submarine, the forces and moments due to their hydrodynamic interactions need to be known at various speeds, longitudinal positions, lateral positions, heading angles, submarine to UUV diameter ratios, and UUV length to diameter ratios. These six variables are considered the input variables to the different CFD simulations required to create the force and moment maps necessary to enable the maneuvering simulation. Determining these forces and moments at every possible combination of these variables enables the most comprehensive maneuvering simulation.

A CFD simulation cannot be performed at every point along a continuous variable because there are an infinite number of simulations that would be needed to completely understand the solution space. Discretizing the continuous variables reduces the number of simulations needed to create the force and moment maps, but this does not provide the same accuracy between discrete points. A trade off exists between increasing the number of discrete points for each variable to improve the accuracy of the force and moment maps and decreasing the number of discrete points to reduce the number of CFD simulations needed to comprehensively explore the solution space. Even if each one of these six input variables are discretized into five values, it would take 15,625 different CFD simulations to explore every possible combination of these input variables. Considering that these CFD simulations usually take hours to days each, this approach is way too intensive to perform all of these simulations. Also, certain variables, like longitudinal position, would need to be discretized into more than five points in order to capture the multiple local extrema and inflection points that are necessary to provide good results from the model.

This dilemma between cost and benefits of experiments and simulations exists in many other fields. Design of Experiments (DOE) is the field of study that deals with planning, conducting,

and analyzing the input and output variables of an experiment. The pioneering study in this field was performed by Ronald A. Fisher in an article titled “The Arrangement of Field Experiments” [32]. The objective is to determine the response of the output variables, or response variables, based on the input variables and noise. DOE is conducted before an experiment is performed to determine how to best use the valuable experimental resources. This practice reduces the number experiments needed to create a statistically valid model. A design is considered an optimal experimental design (OED) when it has the minimum number of experimental runs needed to accurately estimate a parameter.

In the DOE field, the practice of performing an experiment for every possible combination of input variables is called a full factorial design [32], [33]. This method provides the most comprehensive exploration of the design space but is often way too resource intensive to be considered feasible, as is the case with this thesis. There are many ways on how to reduce the number of experiments needed to adequately explore the design space, but they are generally narrowed into two categories: fractional factorial design and sequential design [33]. Fractional factorial design establishes the full set of experiments that will be performed before any single experiment is performed or results are obtained. This approach is well suited to map a function within a given range of input variables and is a good method to comprehensively explore a design space. However, a disadvantage of fractional factorial design is that it may spend resources exploring regions of the design space that may be of no interest. Eliminating areas of the design space that are of no interest and adjusting the design to focus on areas of interest provides a more efficient means of conducting the experiments. This is known as sequential design. Sequential design adapts the design of experiments after every experiment is performed to try to find the maximum benefit for each new experiment. This is a more efficient approach if the intent of the experiment is to maximize the output variable rather than comprehensively explore the design space.

There are many ways to determine a fractional factorial design. The best fractional factorial designs are both balanced and orthogonal [34]. Balanced designs assign the same number of experiments to each value of the input variables which allows the design space to be well explored and provides each input variable the best opportunity to affect the response variables. A design is orthogonal if the effects of one input variable balance out the effects of the other input variables which allows the experiment to determine the impact of each input variable independent from the

others. Aliasing, also known as confounding, becomes a problem when the number of experiments is too small such that the effects of the interactions between input variables are aliased by the input variables. For example, if a study had three different input variables A, B, and C and they each could take on the value of one or negative one, the full factorial design would require eight experiments. The table below shows a half-fraction factorial design because it has four experiments. This DOE demonstrates the problem of aliasing.

Table 4: Demonstration of Aliasing [34]

	Input Variables			Interaction
Run	**A**	**B**	**C**	**A·B**
1	-1	-1	+1	+1
2	+1	-1	-1	-1
3	-1	+1	-1	-1
4	+1	+1	+1	+1

As seen in the table above, the input variable C has the exact same values as the product of A and B. This means that the DOE does not allow any differentiation between variable C and the interaction of A and B. The variables identified in this thesis have known interactions. For example, the two input variables of UUV L/D and heading angle have an interaction. If the UUV L/D ratio is one and looks like a sphere, then the sway, or lift force will be negligible regardless of heading angle. If the UUV L/D ratio increases, this will increase the sway force caused by the flow over the UUV at a non-zero heading angle. As such, the DOE needs to have enough experiments to account for these interactions. DOE allows designs to account for various levels of interactions from both continuous and discrete variables. The experimental design will include as many runs as can be performed in order to increase the accuracy of the model. This also enables the ability to determine two-way, three-way, or higher level interactions between the input variables without the impact of aliasing.

1.5 Thesis Statement

1.5.1 Objective

While the US Navy has developed a strong arsenal of tools to model the hydrodynamic forces and moments of different vehicles in different conditions, they do not have a model that enables them to understand the forces and moments that a UUV will experience when in close proximity to a moving submarine as a result of the interactions between their potential fields and wakes. These hydrodynamic interactions make the L&R of UUVs very challenging because the UUV becomes hard to control and my even collide with the submarine [35]. The goal of this thesis is to expand current understanding of the hydrodynamic forces and moments between these two submerged bodies. The mapping of these forces is vital to simulate the motion of the submerged bodies in close proximity. These force maps will enable developers to create control systems that are adaptive to these hydrodynamic interactions and enable the UUV to stay on a desired trajectory while being launched or recovered from a submarine. In order to enable the simulation of a UUV and submarine moving in close proximity, there needs to be a drastic reduction in the time it takes to determine the forces and moments caused by the hydrodynamic interactions. While most CFD simulations take hours to days, the UUV control system responds within milliseconds in order to maintain a desired trajectory. The UUV needs to be able to rapidly determine these estimated forces and moments based on its position, heading, speed, and vehicle geometry. As such, OED methods will be used to develop parametric models from the CFD results and allow these forces and moments do be rapidly determined from the UUV's position, speed, heading, and size relative to the submarine. Additionally, the force and moment mapping will be used to access the feasibility of existing L&R architectures. The feasibility analysis will be based on the difficulty of overcoming the hydrodynamic interactions with the submarine hull. Recommendations will be made on potential L&R architectures and methods. The objectives are summarized and prioritized below.

Objectives:

1. Create force and moment maps of the hydrodynamic interactions between a moving submarine and UUV operating in close proximity.

2. Develop a parametric model from the CFD results capable of predicting forces and moments based on any relative speed, longitudinal position, lateral position, heading angle, and size difference between the two vehicles.
3. Provide recommendations on the feasibility of different L&R architectures and methods based on the developed force and moment maps.

1.5.2 Methodology

The following methodology will be used to achieve the objectives listed above.

1. Perform a literature review on the hydrodynamic interactions between a submarine and UUV operating in close proximity and the methods to achieve the objectives.
2. Create a CFD simulation that determines the hydrodynamic forces on a single submerged vehicle.
3. Validate the CFD results of a single submerged body against EFD results in literature.
4. Expand the CFD simulation to determine the forces and moments due to the hydrodynamic interactions caused by the wakes and pressure fields of the two vehicles.
5. Validate the CFD results of the hydrodynamic interactions between the two vehicles with EFD results found in literature.
6. Expand the CFD simulations to predict the hydrodynamic forces and moments at any relative speed, longitudinal position, lateral position, heading angle, and size difference between the two vehicles. Use OED to determine how these variables will be changed between simulations.
7. Develop a model that predicts the forces and moments based on the relative speed, longitudinal position, lateral position, heading angle, and size difference between the two vehicles.
8. Perform out of sample validation to ensure that the model is accurate.
9. Use the model to create comprehensive force maps and use them to evaluate different L&R options and make recommendations.

1.5.3 Novelty

This study offers novel contributions to current research in the following three areas.

1. *Geometry*. There are few studies available on the hydrodynamic interactions between a UUV and submarine in the public domain. The only variables that have been explored are how the relative speed, longitudinal position, lateral position, and size difference between the two vehicles affects the hydrodynamic interactions [3]. This thesis will expand the explored geometry in the following two ways.
    a. *UUV Length to Diameter Ratio.* Available UUVs have different L/D ratios. The impact of UUV L/D ratio on the hydrodynamic interaction will be explored during this study.
    b. *Angle.* The available studies have only looked at hydrodynamic interactions of a UUV that is parallel to a submarine. This study will investigate the effect of varying the UUV heading angle on the hydrodynamic interactions.
2. *Parametric Modeling*. While the available studies provided limited results on the hydrodynamic interactions between UUVs and submarines, they do not develop these results into a parametric model that can rapidly predict the forces and moments based on the inputs of the relative speed, longitudinal position, lateral position, heading angle, and size difference between the two vehicles. This is vital for the maneuvering simulation of a UUV in close proximity in to a submarine.
3. *Feasibility Analysis*. While feasibility analyses of L&R recovery methods have been performed, they have been limited in the regions and variables that they consider [11]. This study will evaluate L&R architectures and methods based on more detailed and complex force and moment maps.

Chapter 2

2 Single Body Hydrodynamic Analysis

2.1 Introduction

The objective of this study is to create maps that can predict the forces and moments due to the hydrodynamic interactions between a moving UUV and submarine operating in close proximity. These maps enable the forces and moments to be determined based on the any relative speed, longitudinal position, lateral position, heading angle, and size difference between the two vehicles. Due to the complex and resource intensive nature of the objective, CFD was used to determine these forces and moments caused by the hydrodynamic interactions. Before these hydrodynamic interactions can be explored, the forces and moments needed to be accurately captured on a single body. Without verifying and validating the accuracy of the results on a single body, error could be introduced due to the CFD simulation setup for a single body which would propagate into all of the subsequent results.

In order to complete the objectives of this study, there were numerous CFD simulations that needed to be performed. Ideally, a mesh independence study, turbulence model independence study, and boundary layer independence study would be performed for each configuration and simulation in the study. Due to the limited resources available to perform these necessary CFD simulations, the results of various independence studies in literature were leveraged to ensure that accurate results would be obtained. Resources were best spent examining the novel aspects of the study as well as deepening the understanding and resolution of the solution space rather than performing these independence studies. Additionally, CFD simulations were validated against EFD results to confirm their accuracy which removes the need for independence studies.

In 1989, the Submarine Technology Program Office of DARPA developed a submarine hull geometry known as the SUBOFF model. The purpose of this standardized submarine hull geometry was to allow both CFD and EFD analysis to be performed by different entities. The DARPA SUBOFF model is a relevant submarine hull shape and has since been studied extensively

using both CFD and EFD approaches [27], [29], [36]–[39]. As such, the DARPA SUBOFF submarine hull model was the ideal candidate with which to validate the single body CFD methods and procedures for this study.

2.2 CFD Simulation

To begin the CFD simulation, the unappended SUBOFF model was created in Siemens Solid Edge, a three-dimensional computer aided design (CAD) modeling software. This model was then analyzed in a commercially available CFD simulation software known as Simcenter STAR-CCM+. The SUBOFF model has a length of 4.356 meters and a maximum diameter of 0.508 meters. The following illustration shows the geometry of the SUBOFF model.

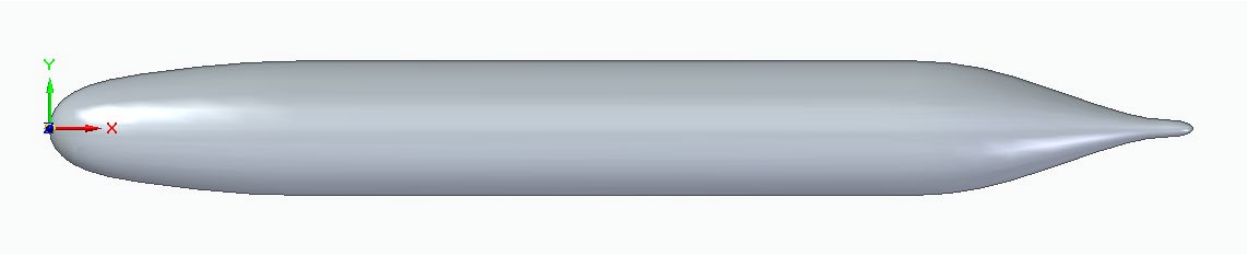

Figure 5: DARPA SUBOFF Hull Model [36]

2.2.1 Domain

The domain of the CFD simulation is the region in which the solver applies the governing physics and equations to determine the flow around the object. The accuracy of CFD simulations depends on the size of the domain. The ITTC suggests that the domain inlet, outlet, and side walls all be at least one model length away from the object [21]. The domain of the single body simulations all fell within these minimum values. The inlet and outlet should be placed at least 10 and 20 model lengths away respectively if significant lift forces are expected. This is not the case for these simulations, even at the largest drift angles. Additionally, the outlet boundary was placed at a distance of three lengths away from the SUBOFF model following the CFD techniques of other studies [24], [25], [29]. The following figure illustrates the simulation domain.

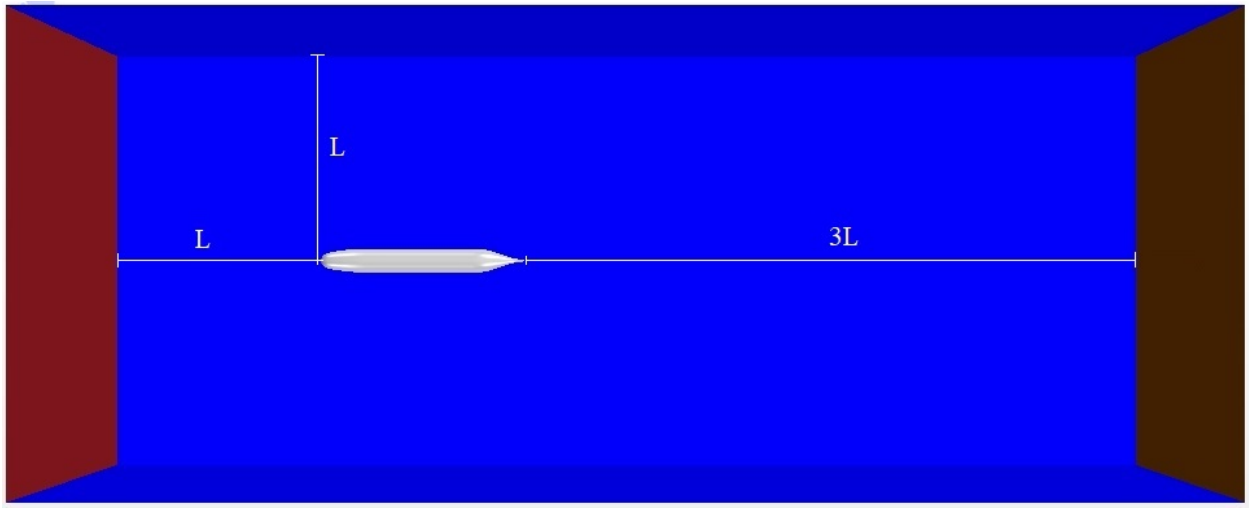

Figure 6: SUBOFF Model Simulation Domain

Additionally, symmetry was used to reduce the necessary size of the domain and, therefore, the time to complete the simulation. Because the SUBOFF model is axisymmetric, the domain size could be drastically reduced by only examining a small wedge about the model axis. However, when a second axisymmetric vehicle is added to the domain, there is only one plane of symmetry, that plane which contains the axes of both vehicles. As such, the domain was limited to only one plane of symmetry which cuts the model in half. This was performed to be consistent with the other simulations in this study. The domain wall that intersected the SUBOFF model was assigned a symmetric boundary condition in order to capture the physics of the full model. All forces and moments were doubled to account for the full model, rather than the half model within the domain. The following figure illustrates the symmetry.

Figure 7: SUBOFF Model Domain Symmetry

2.2.2 Mesh

The mesh of the CFD simulation was established to ensure that it met the necessary criteria to obtain accurate results. According to mesh independence studies in literature, the mesh resolution needed at least 1.2 million cells in domains of similar size to create accurate results [22], [24],

[25]. The mesh in this study had 1.1 million cells, meaning it has the same resolution as a mesh with 2.2 million cells in a domain where symmetry was not utilized. This simulation used an unstructured mesh because it more easily accommodates mesh deformation and restructuring [3]. These meshing features were required when multiple vehicles were added, scaled, and repositioned in future simulations. An unstructured mesh approach has also been proven to be just as accurate as a structured mesh [40]. Additionally, to increase the resolution around the SUBOFF model, the surface growth rate of the mesh was reduced. This makes the cells size grow at a slower rate as they move away from the SUBOFF model. This technique better captures the physics of the flow around the hull and improves the accuracy of the simulation. The figure below shows the basic mesh of the simulation.

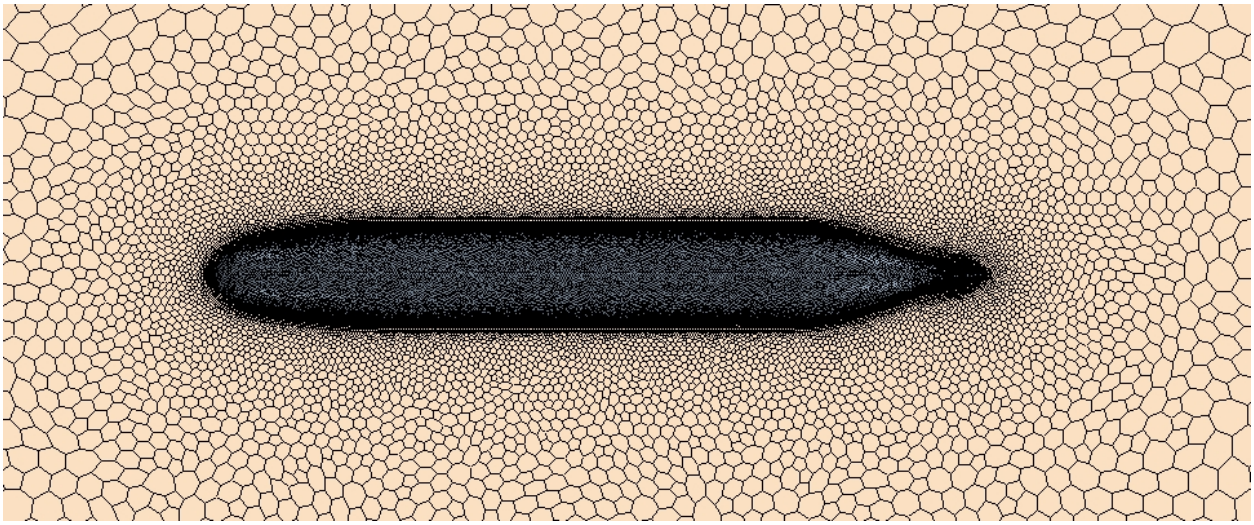

Figure 8: SUBOFF Model Simulation Mesh

2.2.3 Boundary Layer and Turbulence Modeling

Based on recommendations from the ITTC, two-equation turbulence models are by far the most common models that are applied to ship hydrodynamics and have consistently provided accurate predictions. This includes the k-ε and k-ω turbulence models. These different turbulence models have different recommended boundary layer criteria recommended by the ITTC [21]. Additionally, the k-ω SST turbulence model is effective and can be used to interpolate between these two models when the simulation falls in between these two criteria. For this simulation, the k-ω turbulence model was selected because it is more accurate in adverse pressure gradients like those experienced on the stern of the model [21], [26]. The boundary layer was able to be

developed according to the ITTC k-ω criteria so that there was no need to apply the k-ω SST model. The total boundary layer thickness was determined using Prandtl's turbulent boundary layer thickness over a flat plate which is $0.16L/Re_L^{1/7}$, where L is the length of the vehicle and Re_L is the Reynolds number for this characteristic length. This boundary layer mesh was set up using 48 prism layers with an expansion ratio of 1.2. The following figure illustrates the boundary layer mesh.

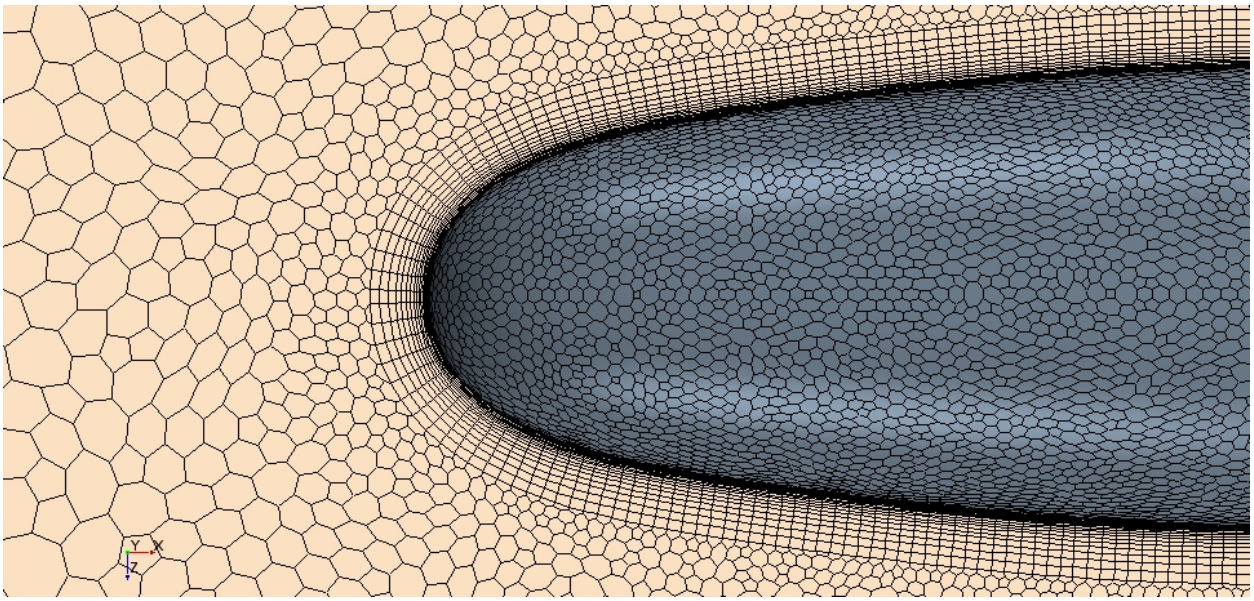

Figure 9: SUBOFF Model Boundary Layer Mesh

In order to satisfy the ITTC criteria for the k-ω turbulence model, the non-dimensional wall distance y^+ has to be less than one at all points along the model. On average, the y^+ value along the model was about 0.15 with a maximum of 0.21. The figure below shows the value of y^+ along the surface of the SUBOFF model and that this ITTC criteria was satisfied.

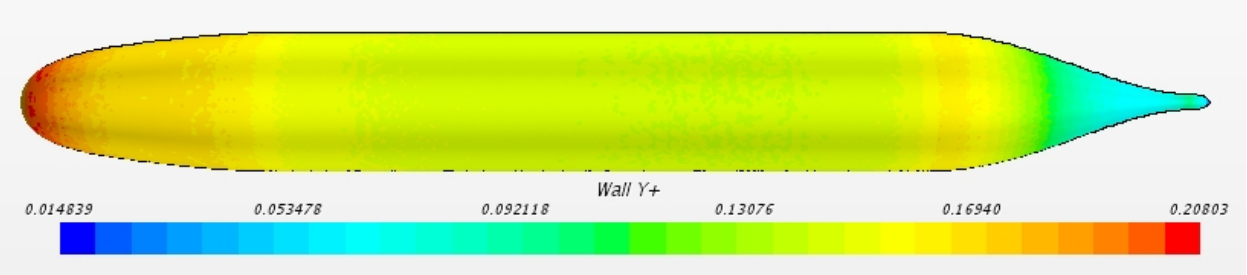

Figure 10: SUBOFF Model Non-Dimensional Wall Distance y+

2.2.4 Angled SUBOFF Model Simulations

One of the novel aspects of this study is to explore the hydrodynamic interactions of a UUV that is at a non-zero heading angle while operating in close proximity to a moving submarine. Before the effects of the hydrodynamic interactions caused by the non-zero heading angle could be determined, the effects of the heading angle were examined on a single body. Again, the DARPA SUBOFF model was used to simulate the forces and moments on the vehicle at various heading angles because of the readily available EFD data on this model. Multiple simulations were conducted and various heading angles up to 10.05°. Overall, the same domain and mesh setup was used on the angled model simulations. The ITTC procedure recommends increasing the distance between the model and the inlet to 10 model lengths and the distance between the outlet and the model to 20 model lengths if significant lift forces are expected [21]. Simulations were conducted at the 10.05° heading angle with the larger domain to see if the lift forces caused the results to vary from the small domain. The surge (X) and sway (Y) forces and yawing moment (N) were only about 0.3% different between the large and small domain so the smaller domain was used to conserve resources for future simulations. The following figures show example meshes for the angled simulations.

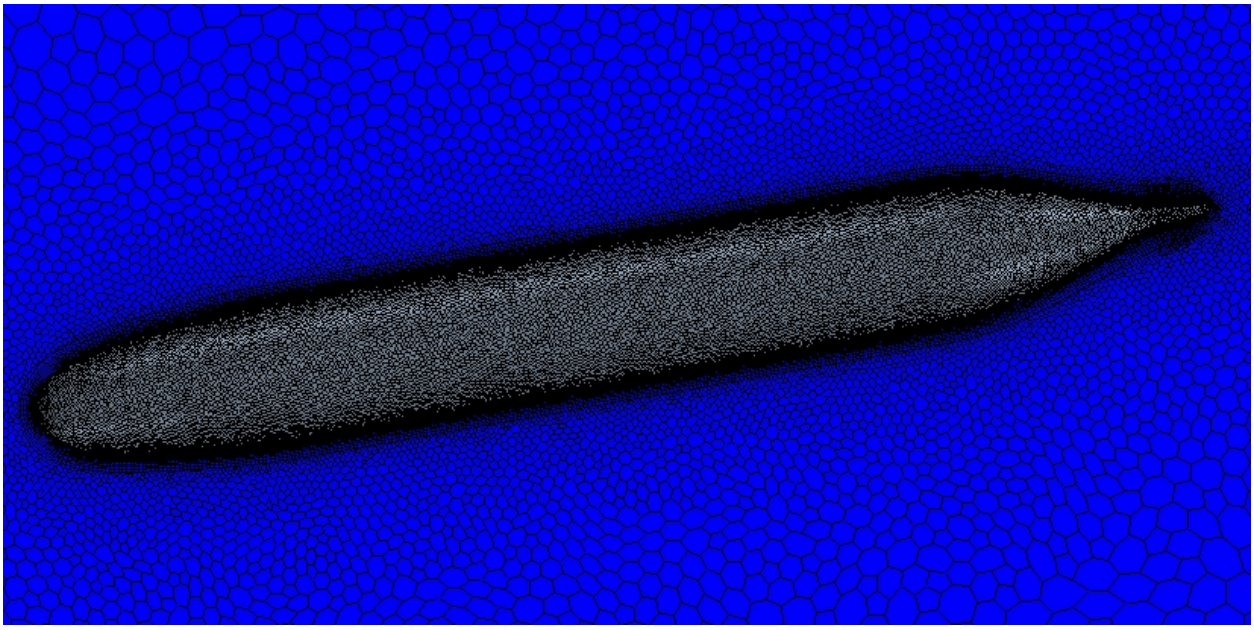

Figure 11: Angled SUBOFF Model Simulation Mesh

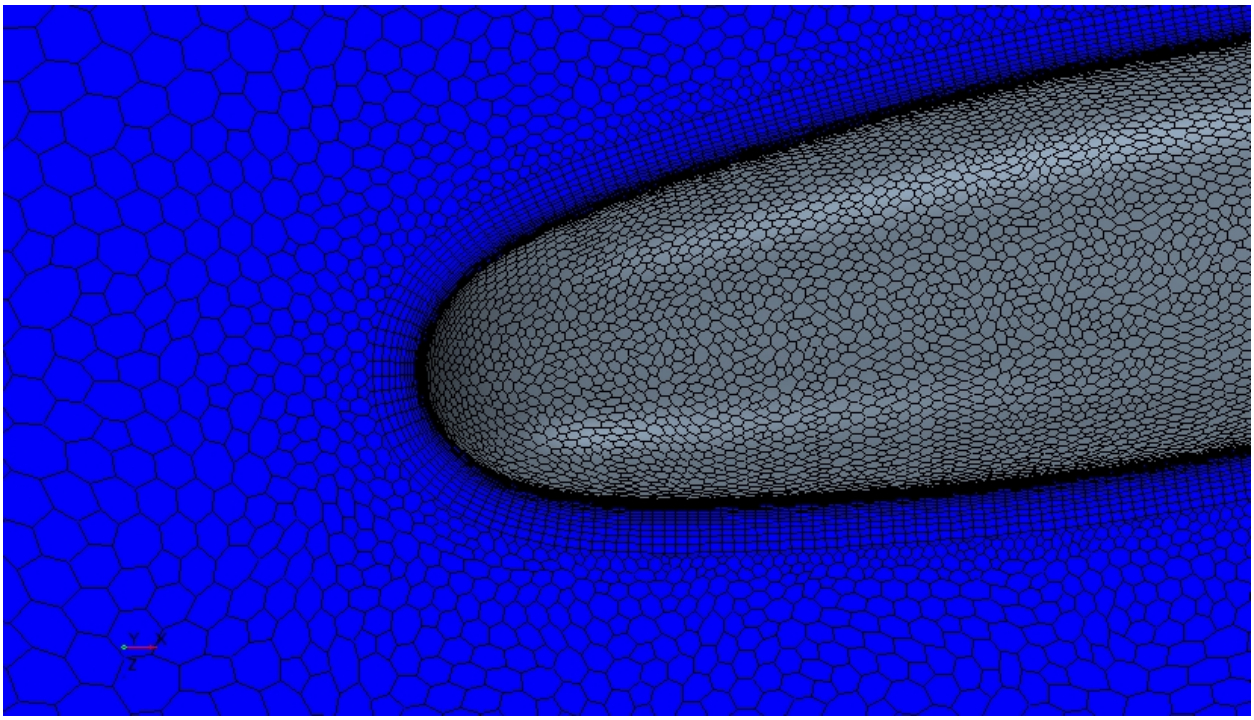

Figure 12: Angled SUBOFF Model Boundary Layer Mesh

Just like the non-angled simulations, the non-dimensional wall distance y^+ for the angled simulations were determined to ensure that they followed the ITTC recommendations. The average y^+ value was about 0.15 with the maximum being 0.202. The figure below shows the y^+ values along the surface of the angled SUBOFF model.

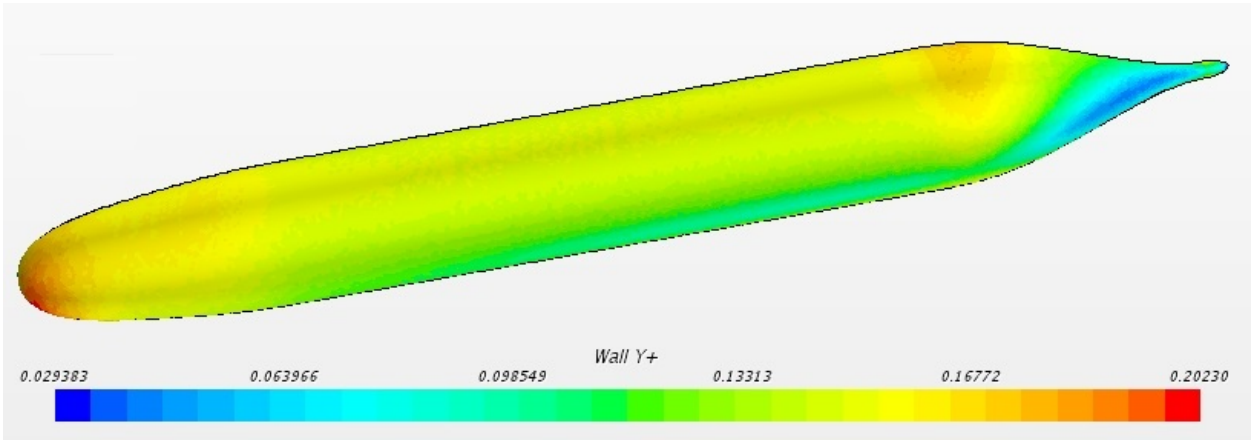

Figure 13: Angled SUBOFF Model Non-Dimensional Wall Distance y+

2.3 Results and EFD Validation

Do to the aforementioned symmetry of the domain, the results of the simulation were reduced from a 6 DOF system to a 3 DOF system. The heave force (Z), roll (K), and pitch (M) moments are zero leaving only the surge, sway, and yaw as non-zero values. Additionally, because the non-angled SUBOFF model was axisymmetric, the system was reduced to a single DOF system leaving the surge force as the only non-zero force acting on the model.

The following table shows the results of the non-angled SUBOFF CFD simulation compared to published EFD results, including the non-dimensional surge force coefficient (X') [39]. The percent error between the CFD and EFD results was 2.06% which validated that the CFD simulation was able to accurately predict the forces on the non-angled SUBOFF model.

Table 5: CFD and EFD Results of Non-angled SUBOFF Model

Model	Speed	CFD X	CFD X'	EFD X	EFD X'	Percent Error
SUBOFF	3.046 m/s	-85.60 N	-9.745×10^{-4}	-87.40 N	-9.950×10^{-4}	2.06%

Determining the hydrodynamic interactions of a UUV at a non-zero heading angle operating in close proximity to a submarine was a novel objective of this study. Validating the forces and moments on a single body angled submersible was a critical intermediate step to ensure the accuracy of the CFD simulations. Many simulations were performed at different heading angles and validated against published EFD results [38]. The figure below shows the force and moment coefficients at various heading angles.

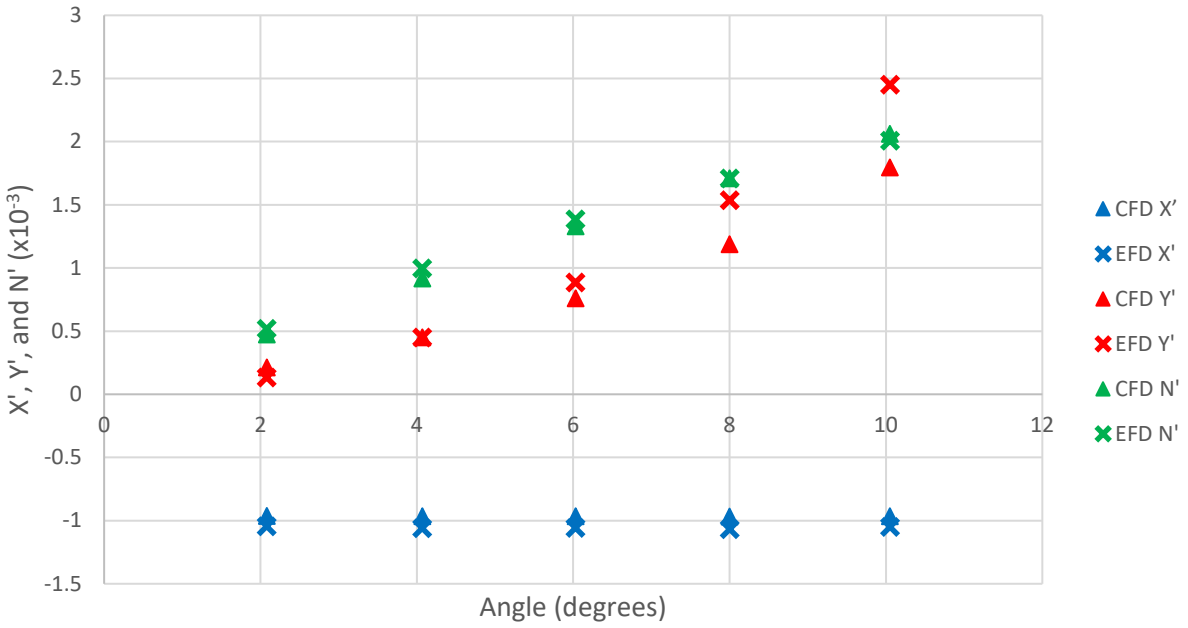

Figure 14: CFD and EFD Results of the Surge, Sway, and Yaw Coefficients versus Heading Angle of the SUBOFF Model

This figure shows that the CFD simulations of the angled SUBOFF model were validated by the EFD results. The difference between the CFD and EFD results were within single digit percent error with the exception of the sway force coefficient at larger heading angles. The EFD results did not contain any uncertainty analysis for the bare hull configuration of the SUBOFF model but provided an approximate margin of error of about 4-10% on other SUBOFF model configurations [38]. Additionally, other literary sources estimated uncertainty of this EFD data at 10%, meaning that the CFD results were within the uncertainty of the EFD results [11], [41]. As the heading angle increased, so did the error of the sway coefficient between the CFD and EFD results. This finding was consistent with other results found in literature [29]. For this reason, this study did not investigate angles larger than 10 degrees. Additionally, large heading angles are much less likely to be experienced in the L&R of UUVs compared to shallow or zero degree heading angles. Also, the percent error of the sway force coefficient at 2.08 degrees was also very large, but this was much less of a concern because of the small value of the force. The sway force experienced at very shallow angles was so close to zero that small errors in the magnitude of the force resulted in large percent errors. Because the motion of the UUV is dependent on the magnitude of the sway force rather than the percent error, the small total error between the very shallow angle CFD and EFD

results is acceptable, even with a larger percent error. The table below shows the percent error of between the CFD and EFD results for each force and moment coefficient.

Table 6: SUBOFF Model CFD and EFD Results and Error of the Force and Moment Coefficients at Various Heading Angles

Angle	CFD			EFD			Percent Error		
(deg)	X' x10^{-3}	Y' x10^{-3}	N' x10^{-3}	X' x10^{-3}	Y' x10^{-3}	N' x10^{-3}	X'	Y'	N'
2.08	-0.962	0.213	0.473	-1.045	0.134	0.517	7.92%	59.5%	8.52%
4.07	-0.964	0.452	0.916	-1.061	0.449	0.996	9.13%	0.78%	8.04%
6.03	-0.966	0.760	1.329	-1.059	0.886	1.385	8.77%	14.19%	4.06%
8.00	-0.968	1.189	1.709	-1.069	1.536	1.708	9.41%	22.61%	0.08%
10.05	-0.966	1.796	2.062	-1.049	2.450	2.008	7.94%	26.71%	2.67%

Overall, the methods used in the CFD simulations were able to accurately predict the forces and moments experienced on a single body. The next step of this study according to the methodology outlined in section 1.5.2 was to expand these CFD simulations to capture the hydrodynamic interactions between two vehicles and validate these new CFD simulations.

Chapter 3

3 Multiple Body Hydrodynamic Interactions

3.1 Introduction

As a submarine moves through the water, it produces a wake and pressure fields around its body. To better enable the L&R of a UUV from a submarine, the hydrodynamic forces and moments need to be determined for the UUV as it maneuvers through the submarine wake and pressure field. If these hydrodynamic interactions are not taken into account, the UUV may become uncontrollable which could make L&R unlikely or even cause the UUV to collide with the submarine [35]. Although both the submarine and UUV would experience these hydrodynamic interactions while operating in close proximity, these forces and moments would only significantly impact the UUV because it is much smaller than the submarine. As such, a major objective of this study is to determine these hydrodynamic forces and moments and create force maps for different vehicle configurations, which are vital to simulate the motion of the submerged bodies in close proximity.

In order to ensure that the CFD simulations were able to predict the actual forces and moments caused by the hydrodynamic interactions between the two vehicles, multiple simulations were run and validated against EFD results. As discussed in section 1.3.1, there are major challenges and expenses to conducting EFD studies on the hydrodynamic interactions between these two vehicles. The methods and facilities used for standard surface ship tow tanks need to be upgraded to capture the 6-DOF motion capable by submerged vehicles. Additionally, tow tank facilities need to be large enough so that experimental models remain unaffected by the restricted water effect [15]–[17]. Because submarines are substantially larger than UUVs, there are problems in selecting model sizes that are small enough to avoid the restricted water effect while being large enough to capture accurate UUV model force measurements with reasonably small uncertainty. As such, there was only a limited EFD data set available against which the CFD simulations could be validated.

The EFD data used to validate this portion of the study were generated by Leong [3]. The submarine to UUV diameter ratio for the study was 2.239. In reality, this is too small represent the size difference between a US submarine and a large UUV but was necessary to ensure that the uncertainty was small enough to keep the results both relevant and accurate. Even with the models being as small as practicable, the submarine and UUV models were still large enough to experience restricted water effects in the tow tanks.

The two vehicles used in this EFD study were the DARPA SUBOFF model as the UUV and a scale model of the International Submarine Engineering (ISE) Explorer AUV acting as the submarine [42]. The bow of the Explorer model is an ellipsoid while the stern is a paraboloid. The equation of the elliptical cross section of the bow is as follows where x is the distance along the vehicle axis, y is the perpendicular distance from the axis, and R is the radius of the vehicle.

$$\left(\frac{x}{2R}\right)^2 + \left(\frac{y}{R}\right)^2 = 1 \tag{1}$$

Likewise, the equation for the parabolic cross section of the stern is listed below.

$$\left(\frac{x}{4R}\right)^2 + \frac{y}{R} = 1 \tag{2}$$

3.2 CFD Simulation

3.2.1 Vehicle Configuration

The EFD data used to validate the two vehicles was gathered at a submarine to UUV diameter ratio of 2.239. This same diameter ratio was used for the CFD simulations. The length and diameter of the Explorer submarine model were L_{Sub} = 2.935 m and D_{Sub} = 0.405 m respectively. To maintain the same diameter ratio as the EFD experiments, the length and diameter of the UUV SUBOFF model were determined to be L_{UUV} = 1.552 m and D_{UUV} = 0.181 m respectively. The simulations were run at a forward speed of U = 0.75 m/s with a water density of ρ = 997 kg/m^3 and dynamic viscosity of $\mu = 8.899 \times 10^{-4}$ Pa·s. Using the both the submarine and UUV lengths over all (LOA) as the characteristic lengths L, the Reynolds Numbers were determined to be $Re_{Sub} = 2.47 \times 10^6$ and $Re_{UUV} = 1.31 \times 10^6$. All of these parameters were held constant across the different CFD simulations to align with the EFD methods.

Two non-dimensional parameters known as the lateral and longitudinal separation ratios, R_{Lat} and R_{Long}, were used to refer to the distances between the two vehicles. The equations for these two parameters are as follows.

$$R_{Lat} = \frac{y_{Dist}}{L_{Sub}} \tag{3}$$

$$R_{Long} = \frac{x_{Dist}}{L_{Sub}} \tag{4}$$

The relative lateral distance x_{Dist} and relative longitudinal distance y_{Dist} are measured between the centers of buoyancy CB of the two vehicles. R_{Long} is positive when the CB of the UUV is located in front of the CB of the submarine. The following figure illustrates the geometry and arrangements of the CFD simulations.

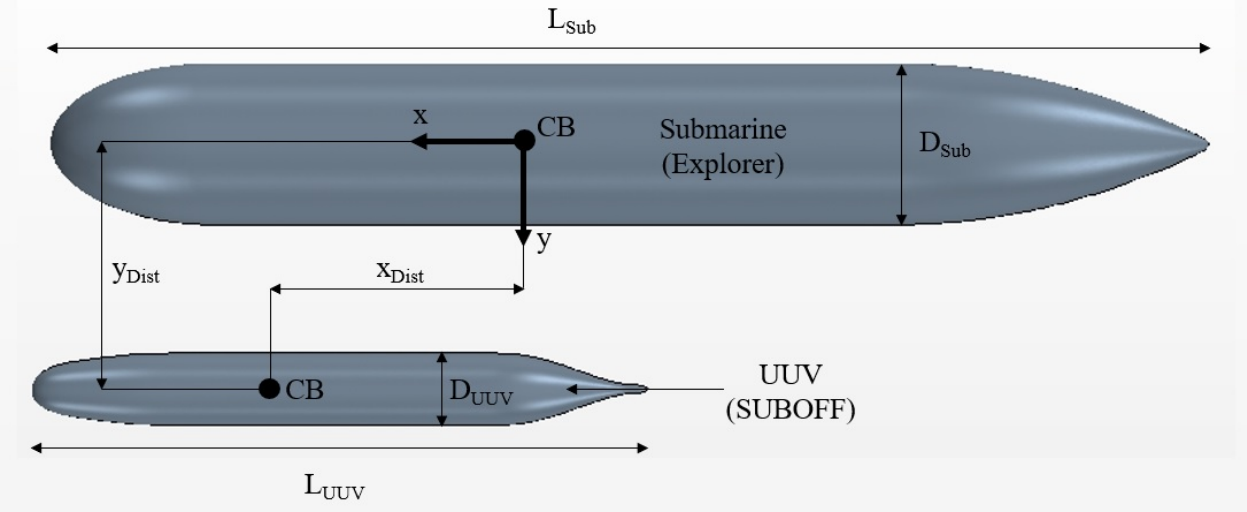

Figure 15: Geometry and Orientation of CFD Simulations

3.2.2 Domain

The domain of the CFD simulations with the two vehicles was similar to that outlined in section 2.2.1. The domain was made symmetric about the plane that intersects the axes of the two vehicles. This meant that the forces and moments were simulated on half of the bodies and then doubled to account for the forces and moments experienced on the full bodies. This allowed the domain to be half the size of a domain that does not take advantage of this symmetry. This reduced the required computational time and allowed for a more robust exploration of the future OED solution space by enabling more simulations to be performed.

The ITTC guidelines are not tailored for studies involving multiple bodies but a conservative approach was taken to ensure that the minimum distance between the domain boundaries and vehicles was maintained according to ITTC recommendations [21]. The same domain was used for each simulation, even as the UUV was repositioned. The domain was made large enough to account for the appropriate spacing, even as the UUV was repositioned between simulations. The following figure shows the design of the domain.

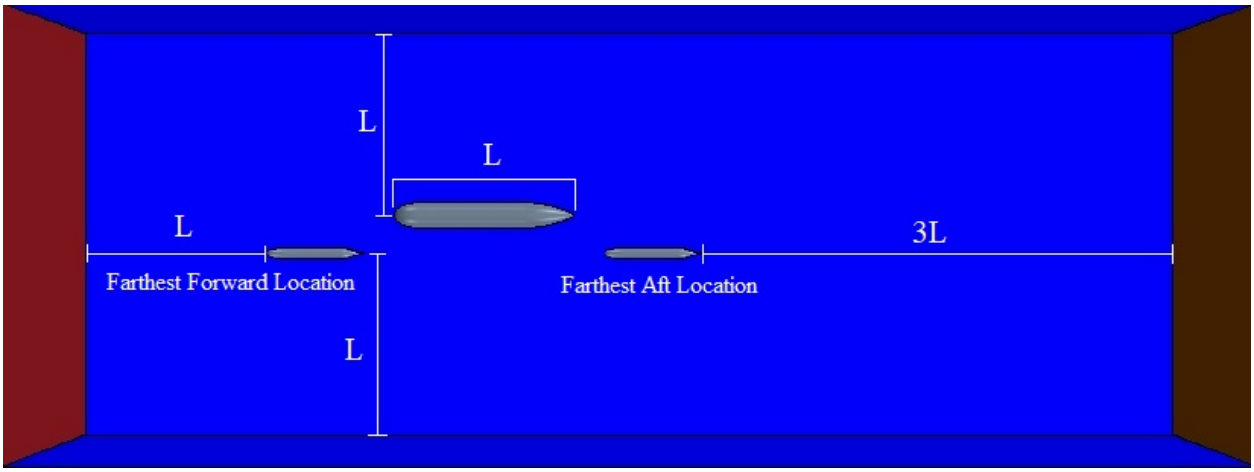

Figure 16: CFD Domain for Two Vehicle Simulations

3.2.3 Mesh

The mesh of the CFD simulation was designed to comply with a mesh independence study in the literature in order to ensure that the results were accurate [3]. This mesh independence study showed that at 3.9 million elements and above, the force and moment predictions were within 2% of the finest mesh investigated. This domain did not take advantage of the symmetry of the problem, meaning that the same mesh resolution would be reached at about 1.9 million cells for the symmetric domain in this study. Also, this mesh independence study was also for a much larger domain than used in this study, meaning that a higher resolution mesh could be achieved with fewer cells. As such, 1.9 million cells was a target for the mesh cell count but was not a hard requirement because of the size difference between the domains.

This simulation used an unstructured polyhedral mesh because it more easily accommodates mesh deformation and restructuring as the UUV is repositioned between simulations [3]. Once again, the resolution around the Explorer and SUBOFF models was increased by reducing the surface

growth rate of the mesh to better capture the flow around the hull. The figure below shows the basic mesh of one of the simulations.

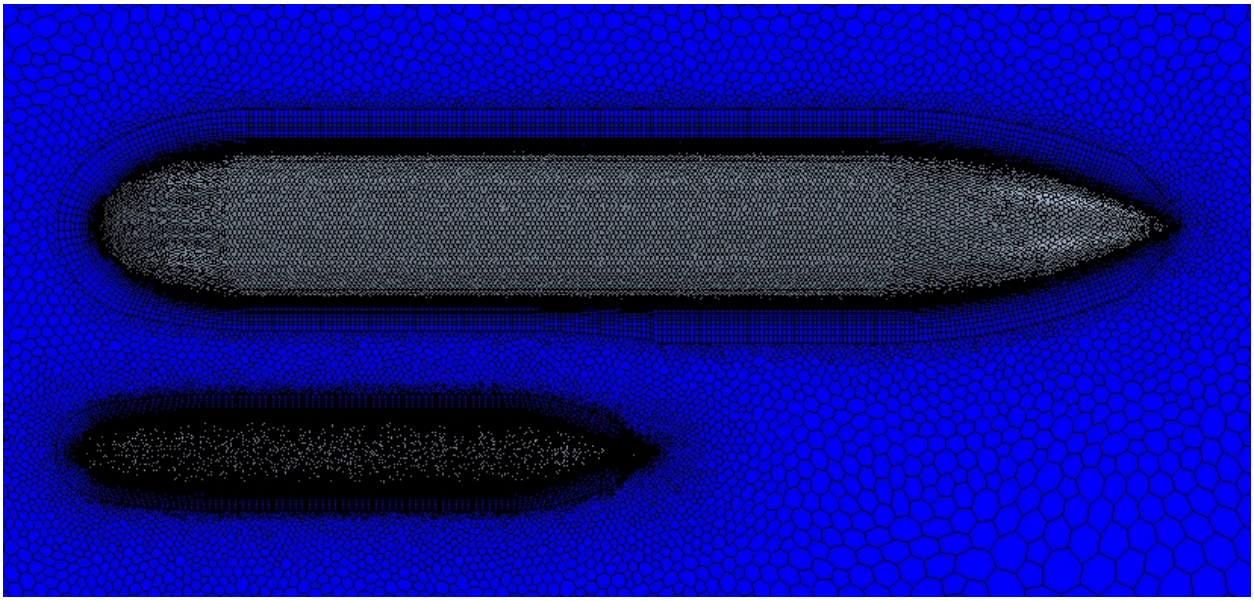

Figure 17: CFD Mesh for Simulation of RLat = 0.21 and RLong = 0.234

3.2.4 Boundary Layer and Turbulence Modeling

For the reasons outlined in section 2.2.3, these simulations used the k-ω turbulence model because of its accuracy. The boundary layer was able to be developed according to the ITTC procedures [21]. Per the recommendation of the Leong, the total boundary layer thickness was calculated using twice the Prandtl's turbulent boundary layer thickness over a flat plate or $2x0.16L/Re_L^{1/7}$ [31]. This was doubled from that in section 2.2.3. The additional thickness of the boundary layer mesh provided a higher resolution mesh farther away from the boundary, which provided a better opportunity for the prism layer mesh to capture the flow in this area of interest. This boundary layer mesh was set up using 46 and 43 prism layers on the submarine and UUV models respectively, each with an expansion ratio of 1.2. The following figure illustrates the boundary layer meshes.

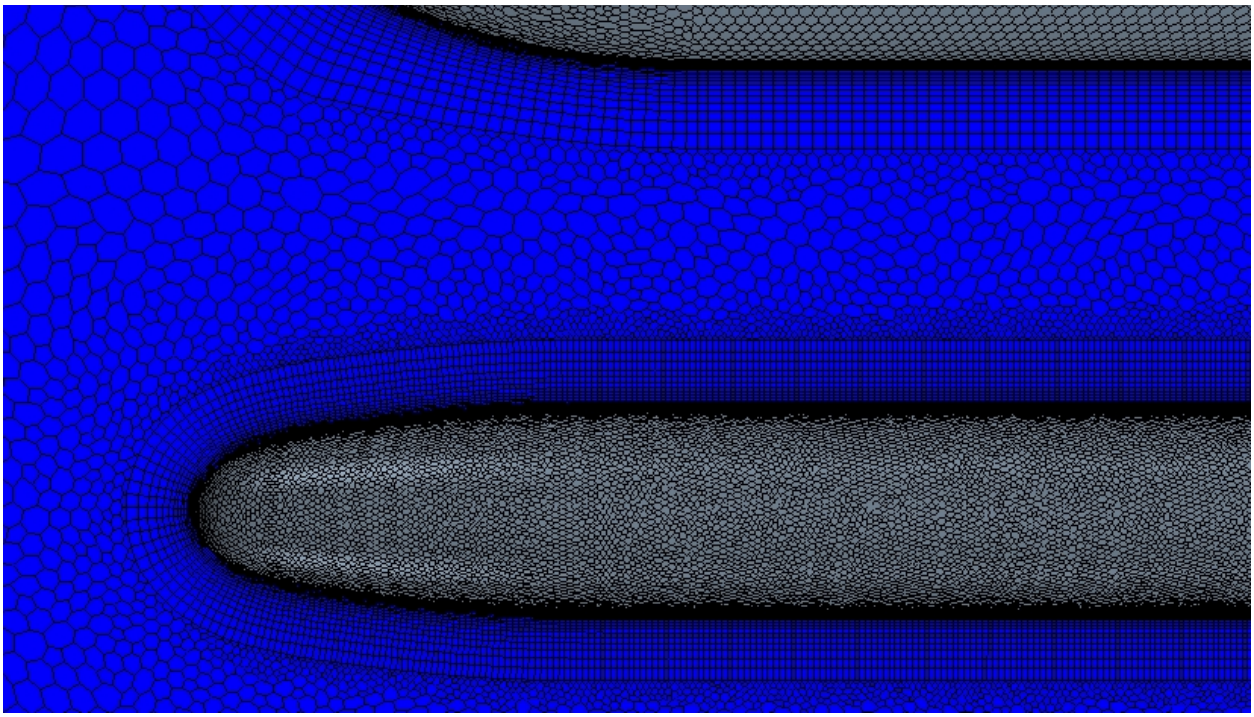

Figure 18: Submarine and UUV Model Boundary Layer Meshes

The non-dimensional wall distance y^+ values along the boundary of the submarine and UUV models were determined to ensure that they were less than one in accordance with the ITTC guidelines [21]. The figure below shows that the y+ values at every point along the boundary of these two models is within these guidelines.

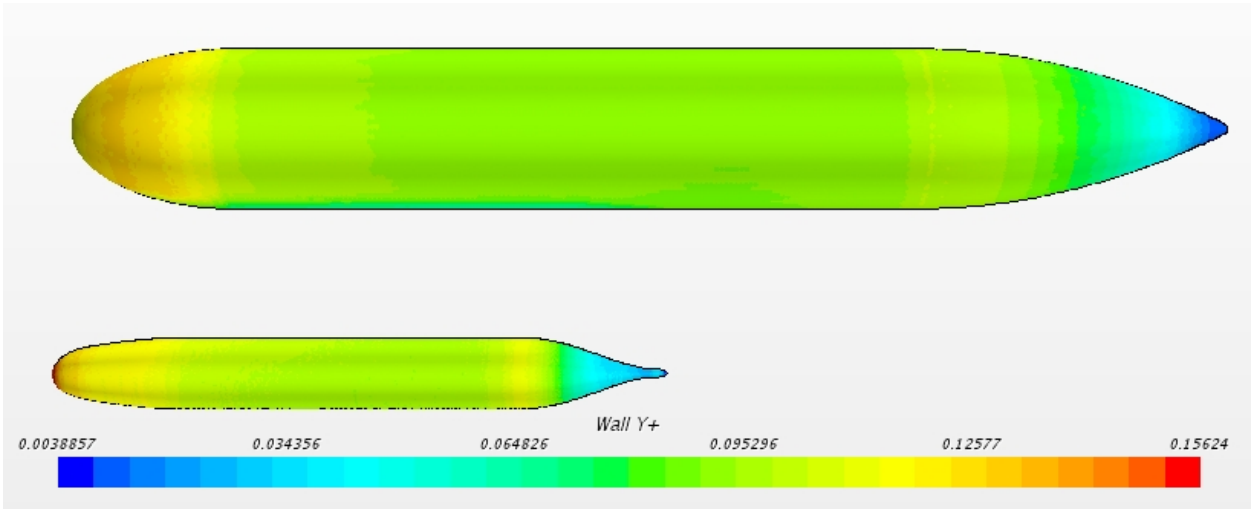

Figure 19: Submarine and UUV Model Non-Dimensional Wall Distance y+

3.3 Results and EFD Validation

As discussed in section 3.1, the EFD data that could be used to validate these CFD results were very limited. The EFD experiments were performed by Leong at a submarine to UUV diameter ratio of 2.239 and various longitudinal positions [3]. Leong was able to create EFD experiments to measure the surge and sway forces and yawing moment on the UUV. The experimental uncertainty of the study was 2.252×10^{-4} for the surge and sway force coefficients and 1.446×10^{-4} for the yawing moment coefficient. However, due to the limitations of the facilities and model sizes, these EFD results were influenced by the blockage or restricted water effect. The walls of the tow tank were close enough to the models that the presence of the wall limited the ability of the water to flow freely around the models. This had an impact on the measured forces and moments. When Leong performed his CFD simulations, he was able to model the tow tank walls into the domain of his CFD simulations. When Leong accounted for the tow tank walls in his CFD simulations, the CFD was able to accurately predict the measured forces and moments within the experimental uncertainty. In order to determine the forces and moments without the restricted water effects, Leong expanded his CFD domain and removed the tow tanks walls from his simulation. By removing the tow tank walls from the CFD studies, the assumption was made that his CFD simulations were still able to capture the real world physics between the submarine and UUV model because no changes were made to this part of the simulation. As such, the Leong's CFD results with no blockage or restricted water effects were considered to be valid. The figure below shows the results of this CFD study plotted beside the Leong's validated results. The error bars on Leong's results indicate the experimental uncertainty of his tow tank tests.

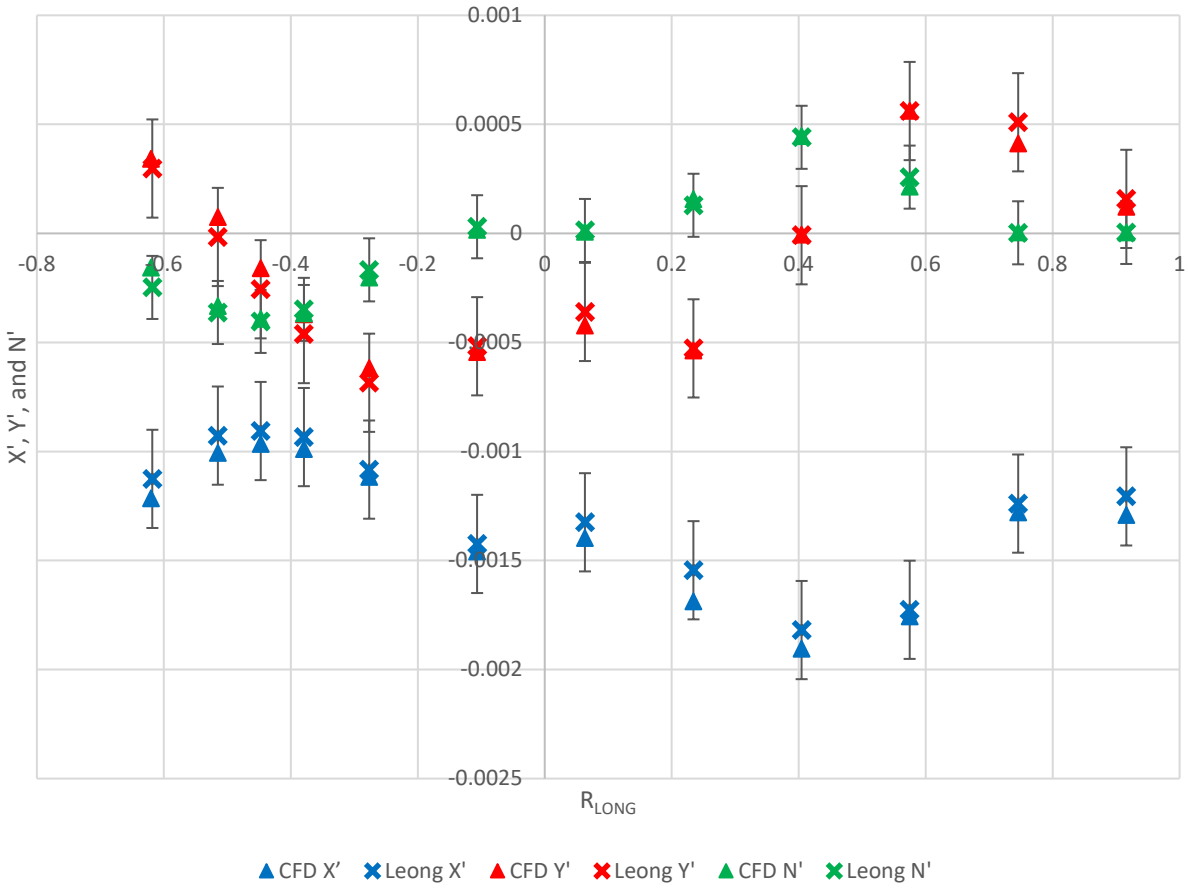

Figure 20: Surge, Sway, and Yaw Force and Moment Coefficients at Various Longitudinal Positions for the CFD simulations and Validated Leong Results [3].

As seen in Figure 20, the CFD results of this study were within the experimental uncertainty of Leong's validated results. The CFD simulations were able to capture the large degree of change in the force and moment coefficients as the longitudinal position of the UUV was varied. Putting all of this together, the methods and results of the CFD simulations were considered valid for the limited data.

No EFD data were available for experiments where a UUV at a non-zero heading angle was operating in close proximity to a moving submarine. As such, no validation could be performed for this specific set of the CFD simulations explored in this study. However, the CFD results for a single UUV at a non-zero heading angle and the CFD results for a UUV at a zero degree heading angle operating in close proximity to a moving submarine were both validated against EFD data. For this reason, the CFD methods were still assumed to be accurate enough to continue with this study, even though they could not be experimentally validated.

Chapter 4

4 Optimal Experimental Design and Modeling

4.1 Introduction

As discussed in section 1.4, the two main ways by which a set of experiments may be optimized are by using a fractional factorial design method or sequential design method. The fractional factorial design method generates the entire set of experimental runs without incorporating any feedback from the results of the experiment. These methods are well suited when the output function is of a known form. If the output function were to change from a linear model to a polynomial, exponential, or response surface model, this would change the design of the experiments. Additionally, the degree of the interactions between input variables needs to be determined before the experiment is designed. This allows the experiment to be designed to account for any aliasing between input variables and interactions.

The limitations of the fractional factorial design method are not well suited for this CFD study. Because the form of the output function was unknown, optimally designing a set of experiments for a specific output function was unlikely to be optimal for the unknown output function. Additionally, because the number of runs would be predetermined for a fractional factorial design, this would not likely capture the maximum number of CFD simulations that could be run. As such, a sequential design method was used. This method takes the results from previous experiments and uses this information to determine the optimal next experiment. This enabled the number of CFD simulations to be as many as could be run in the allotted time.

The specific sequential design method that was used in this study was a Gaussian process (GP) regression model that used a Bayesian optimization and active learning method with likelihood-weighted acquisition functions [43]. A code that uses the GPy python framework from the Sheffield machine learning group was created by Sapsis and Blanchard and made available to the general public. This GP method uses the results of previous CFD simulations to determine the input variables for the next simulation. By using a squared exponential (SE) covariance function

between the input and output variables, this method simulates a Bayesian linear regression model with an infinite number of basis functions. In other words, the SE covariance function can be formed from a linear combination of an infinite number of Gaussian-shaped basis functions [44]. Because an infinite number of these basis functions can determine the form of any output function, this method is well suited for this study with an unknown form of the output function. The GP method does not need any estimations about the form of the output function because an infinite number of basis functions can predict any output function. Instead of optimizing experiments to fit a predetermined output function, the GP method searches for the location in the design space where there is the largest amount of uncertainty. By performing a simulation at this location, the uncertainty is reduced and the method then looks for the next location with the largest amount of uncertainty. This is how the GP method was used to conduct the OED.

Two major adaptations to the code created by Sapsis and Blanchard were implemented to make it more applicable to this study. The exact changes to the code are recorded in the appendix. These adaptations are as follows:

1) The CFD study has three different forces and moments as output variables. The standard GP code optimizes the inputs based off of one single output. Assuming that 90 simulations could be performed with the allotted resources, the original code could be used to run 30 simulations for the first output variable, another 30 simulations for the second output variable, and then another 30 simulations for the third variable. Because the GP method identifies the next optimal experiment based on one output variable, it has no way of determining the optimal experiment for three variables. However, instead of splitting the number of total simulations into three independent studies of each output variable, the code was modified to alternate the output variable to which the experimental design was being optimized. Instead of three separate studies, the code was modified to enable the three output variables to be handled as one study. This way 30 simulations would be optimized for each output variable, but it would be able to use the data from the other simulations that were suboptimal for a particular output variable to design the experiment. Overall, 30 optimal simulations and 60 suboptimal simulations for a given output variable would provide better data than only using the 30 optimal simulations for each output variable.

2) The second adaptation to the code was the incorporation of constraints into the input variable design space. Not all possible combinations of the input variables were capable of being run. For example, if the smallest lateral distance between submarine and UUV and the largest diameter UUV were selected, these two vehicles would partially overlap. This problem could have been mitigated by reducing the bounds on the input variables but the bounds were set based on real world application. Reducing the bounds would have made important parts of the design space go unexplored. Instead, the code was modified to allow non-negative inequalities to act as constraints to the input variables. This allowed for the elimination of any undesired combinations of input variables.

The CFD simulations that were conducted as part of this OED were performed with the same methodology and setup used in chapter 3 with a few minor changes. In order to recreate a more realistic representation of a submarine and UUV interaction, the submarine was switched to the DARPA SUBOFF model while the UUV was switched to the Explorer AUV model. Each of these models better reflect the geometry of the vehicles they represent in this setup. For this series of CFD simulations, the SUBOFF model was scaled to represent a full size submarine. The diameter was set as 34 feet (10.36 m) which is the same diameter as the Virginia class submarine [45]. The Virginia class submarine was selected instead of the Ohio class submarine because the L/D ratio of the Virginia class submarine is closer to that of the SUBOFF model. This means that the SUBOFF model was better suited to mimic the Virginia class submarine that the Ohio class. Additionally, the mission of the Virginia class submarine is much more likely to incorporate the L&R of UUVs than the Ohio class. Once the SUBOFF model was scaled to a diameter of 34 feet (10.36 m), it had a LOA of 291.55 feet (88.86 m). This is shorter than the 377 feet (114.91 m) LOA of the actual Virginia class submarine. Also, the Explorer AUV model was scaled to different lengths and diameters for each simulation. By scaling the Explorer AUV model to different lengths and diameters, the curvatures of the bow and stern were scaled as well. This was done so that a new CAD model would not need to be created for each simulation by extending or reducing the parallel midbody section of the model to maintain the bow and stern curvature while satisfying the

custom UUV L/D ratio. Additionally, shorter length UUVs tend to have a more blunt shaped bow and stern so this scaling tends to more accurately depicted the various UUV models [11].

4.2 Input Variables

For this experimental design, the following six different input variables were considered.

1. Longitudinal Separation Ratio. This is defined in Equation (3) and Figure 15 as the longitudinal distance between the centers of buoyancy of the submarine and UUV divided by the length of the submarine. The bounds of this variable were set between -1.5 and 1.5 based on when the effect of the interaction forces and moments are present [3].

2. Lateral Separation Ratio. This is defined in Equation (4) and Figure 15 as the lateral distance between the centers of buoyancy of the submarine and UUV divided by the length of the submarine. The bounds of this variable were set between 0.064 and 0.65 based on when the effect of the interaction forces and moments are present [3]. The interaction forces and moments are still experienced beyond a lateral separation ratio of 0.65 but they became very small. Focusing on areas closer to the submarine makes the study more relevant to the L&R of UUVs.

3. Speed. The speed of the UUV and submarine were varied between 2 and 5 knots (1.029 and 2.572 m/s). These numbers were based on the maximum speed attainable by most commercially available UUVs and the minimum speed at which submarines are operated to maintain controllability [11]. The three output variables of the surge and sway force coefficients and the yawing moment coefficient were non-dimensionalized based on the speed. This means that these output variables should be relatively independent of speed, as experienced by Leong in his study [3]. However, none of Leong's simulations or EFD experiments were conducted with the UUV at an angle. If the speed affects the potential flow separation along an angled UUV, this would affect the output variables. Non-angled UUVs retain a similar flow pattern which keeps the output variables independent of speed. While the output variables may be independent of speed in this study, the speed was still kept as an input variable to be conservative and capture any unexpected phenomenon.

4. Heading Angle. For this study, the heading angle is defined as the angle between the longitudinal axes of the submarine and UUV where a positive angle denotes the bow of the UUV is pointed away from the submarine. The bounds of the heading angle were limited between -10 and 10 degrees based on the accuracy of the CFD models as shown in Figure 14 and Table 6 and the unlikely nature that a UUV would have larger heading angles during L&R operations.

5. Submarine to UUV Diameter Ratio. The following table shows a compilation of different UUV sizes taken from various sources [11], [42], [46]–[49]. The UUV diameters were compared to the Virginia class and Ohio class submarine diameters. In order to account for all of these submarine to UUV diameter ratios, the bounds of this parameter were set from 5 to 100.

Table 7: Sizes of Various UUVs[11], [42], [46]–[49]

Size	Name	Manufacturer	Length (m)	Diameter (m)	UUV L/D	D_{Sub}/D_{UUV} (Virginia)	D_{Sub}/D_{UUV} (Ohio)
S	REMUS 100 (Swordfish)	Hydroid	1.60	0.19	8.42	54.53	67.37
M	REMUS 600 (LBS AUV, Kingfish, Razorback)	Hydroid	3.25	0.32	10.03	31.98	39.51
L	REMUS 6000	Hydroid	3.84	0.71	5.41	14.59	18.03
L	HUGIN 1000	Kongsberg	4.50	0.75	6.00	13.81	17.07
L	HUGIN 3000	Kongsberg	5.50	1.00	5.50	10.36	12.80
L	HUGIN 4500	Kongsberg	6.00	1.00	6.00	10.36	12.80
S	Bluefin Sandshark	Bluefin	1.09	0.12	8.79	83.55	103.23
M	Bluefin 12	Bluefin	3.00	0.33	9.09	31.39	38.79
M	Bluefin 21 (Knifefish)	Bluefin	5.80	0.53	10.94	19.55	24.15
M	Bluefin 21	Bluefin	3.30	0.53	6.23	19.55	24.15
M	AUV 62 Sapphires	SAAB	7.00	0.53	13.21	19.55	24.15
L	Autosub	Uni. Southamton	7.00	0.90	7.78	11.51	14.22
S	IVER3	L3Harris	1.52	0.15	10.37	70.48	87.07
L	Explorer	ISE	5.36	0.74	7.24	14.00	17.30
L	Innovative Naval Prototype - Snakehead	ONR	5.25	1.22	4.30	8.49	10.49
L	Maximum Possible	N/A	10.00	2.13	4.69	4.86	6.01

6. UUV Length to Diameter Ratio. The table above shows various different UUV L/D ratios. The bounds of this variable were set from 4.3 to 13 in order to reflect the various UUV designs.

The following table summarizes the input variables and their different bounds.

Table 8: Summary of Input Variables

Variable	Symbol	Description	Units	Bounds
$\mathbf{X_1}$	R_{Long}	Longitudinal Separation Ratio	None	[-1.5, 1.5]
$\mathbf{X_2}$	R_{Lat}	Lateral Separation Ratio	None	[0.064, 0.65]
$\mathbf{X_3}$	U	Speed	Knots	[2, 5]
$\mathbf{X_4}$	ϕ	Heading Angle	Degrees	[-10, 10]
$\mathbf{X_5}$	D_{Sub}/D_{UUV}	Submarine to UUV Diameter Ratio	None	[5, 100]
$\mathbf{X_6}$	L/D_{UUV}	UUV Length to Diameter Ratio	None	[4.3, 13]

4.3 Constraints

As discussed in section 4.1, constraints were used within the design space to ensure that all of the simulations were feasible and reflected realistic scenarios. If the input variables with these given bounds were varied without constraint, the submarine and UUV could overlap, creating an infeasible simulation. A lateral constraint was established using the following first order and small angle approximate geometric setup. Rather than make the lateral constraint dependent on the sinusoidal function of one of the input variables, the maximum heading angle was used to determine the constraint in order to reduce this function to a constant and simplify the resulting expression.

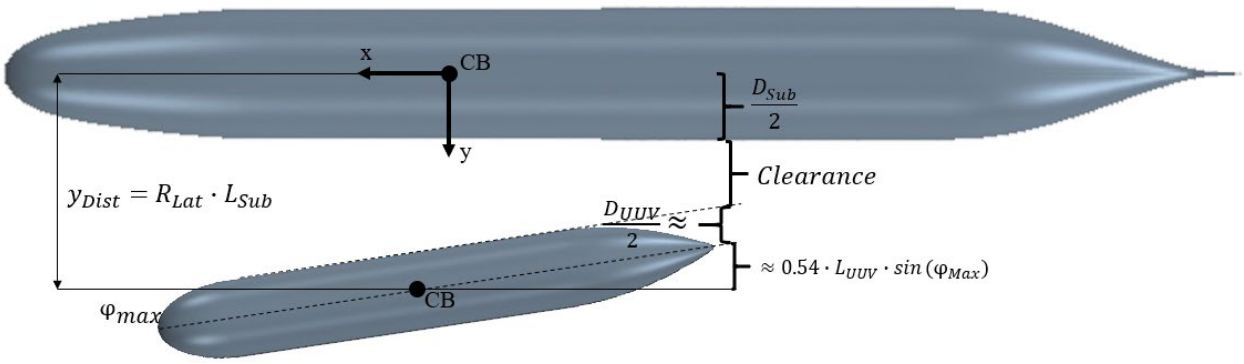

Figure 21: Geometric Configuration of Lateral Constraint

The clearance between the two vehicles, denoted as the variable c, was determined using the following equation.

$$c = R_{Lat} \cdot L_{Sub} - \frac{(D_{Sub}+D_{UUV})}{2} - 0.54 \cdot L_{UUV} \cdot sin\,\varphi_{Max} \quad (5)$$

The minimum clearance between the two vehicles was set as 0.25 meters. By applying the simulated submarine dimensions from section 4.1 into this equation and making it non-dimensional, the following constraint was developed from the input variables in Table 8.

$$8.575 \cdot x_2 - \frac{1}{2}{x_5}^{-1} - 0.09277 \cdot {x_5}^{-1} \cdot x_6 - 0.5241 \geq 0 \quad (6)$$

There were also simulations that were infeasible based on the relationship between the length and diameter of the UUVs. In order to determine the viable relationship between the UUV L/D ratios and the submarine to UUV diameter ratios, all of the UUV architectures in Table 7 were plotted in the following figures. Constraints were developed to reflect viable UUV designs. For example, if a large diameter UUV, like the snakehead, had a large L/D ratio, then is would be longer than the diameter of the submarine. Eliminating these kinds of configurations allows a more thorough study of the design space at hand. The first figure represents the constraints based on the UUV diameter while the second figure makes this parameter dimensionless to match the input variables in Table 8.

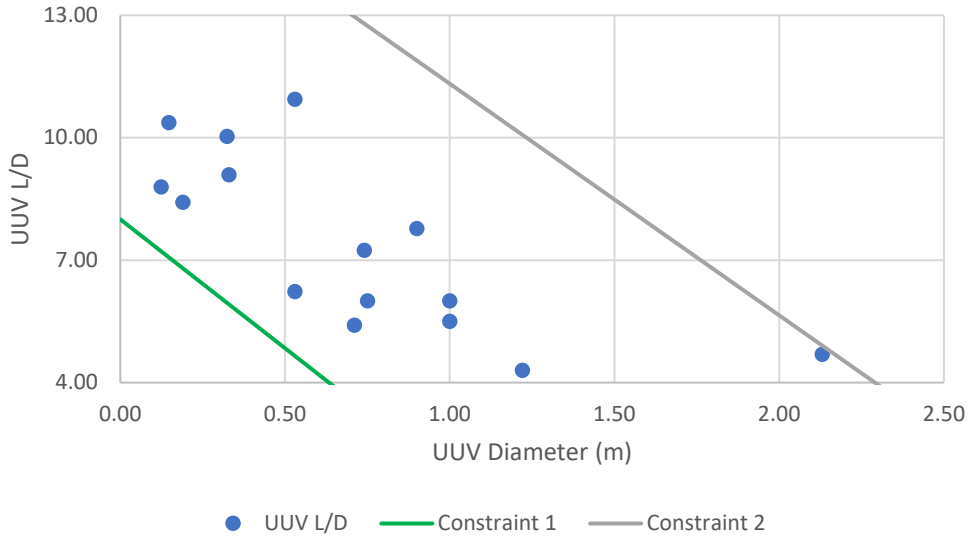

Figure 22: Dimensional UUV Geometric Constraints

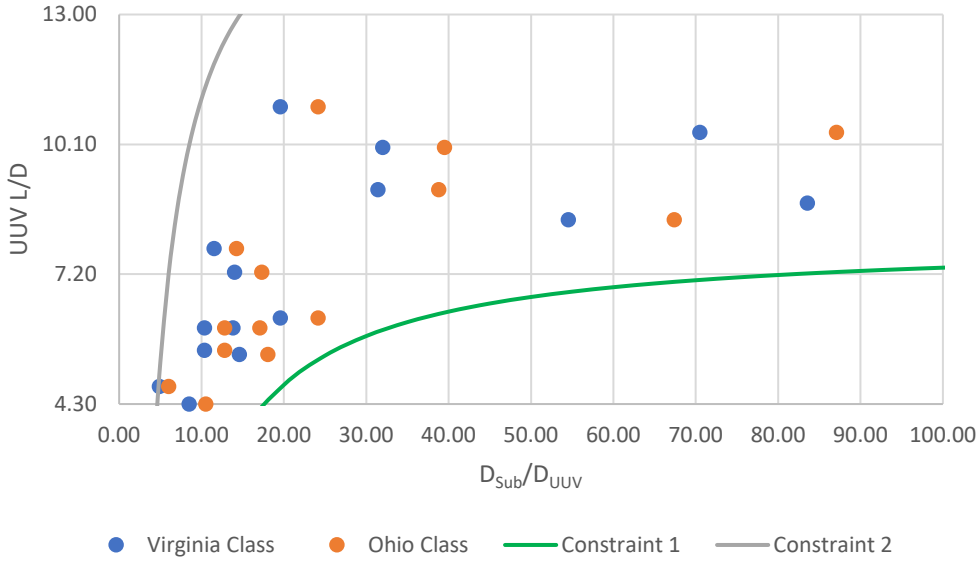

Figure 23: Non-dimensional UUV Geometric Constraints

The UUV geometric constraints were made non-dimensional to match the input variables in Table 8. The following equations represent these constraints based on the input variables.

$$65.442 \cdot {x_5}^{-1} + x_6 - 8 \geq 0 \quad (7)$$

$$-58.810 \cdot {x_5}^{-1} - x_6 + 17 \geq 0 \quad (8)$$

The implementation of these equations into the GP source code can be seen in the appendix.

4.4 Optimal Experimental Design

The values of the input variables were determined for each simulation using the GP method discussed above. In order to begin the process, an initial set of experiments were conducted to provide data that could be used to initialize the optimization algorithm. Six different simulations were run at random values for the input variables. This number of runs was chosen because there were six different input variables. The remainder of the simulations were initialized so that the values for the input variables were optimized to one of the three output variables. The three output variables were rotated between experiments as the output to which the experiments were optimally designed. The raw data for these experiments can be found in the appendix.

4.4.1 Simulations

The simulations were conducted using the validated procedures in chapters 2 and 3. Due to the large number of simulations and the variations in their geometries, each individual simulation could not be independently validated. However, because they used the same CFD code that was validated, the assumption was made that the results from these simulations were accurate. Similar assumptions have been accepted in literature. When Leong removed the tow tank walls from his CFD studies, the assumption was made that his CFD simulations were still able to capture the real world physics between the submarine and UUV model because no changes were made to this part of the simulation [3].

The sway force at large heading angles is likely to be lower than experimental results as shown in section 2.3. Additionally, the geometries of these simulations are much more extreme than those performed in the EFD studies. For example, current EFD work was conducted at a submarine to UUV diameter ratio of 2.239. The simulations for this study explored submarine to UUV diameter ratios up to 100. There is the possibility that the extreme values of the simulations at hand introduce results that were not able to be captured in the previous work. For this reason, EFD validation of the results of model is recommended as future work.

4.5 Results

4.5.1 Gaussian Process Regression Model

A Gaussian process regression model was used to map the surge, sway, and yaw coefficients based on the six input variables. A total of 200 CFD simulations were performed at various input variables as part of the OED. Because the design space is very vast and results cannot be displayed in six dimensions, the plots below vary two of the input variables across the entirety of the domain while keeping the other four input variables fixed. Just because a plot that compares two variables looks a certain way does not mean that it will look that way if the fixed variables were at different values. For this reason, the fixed values were chosen at points near the center of the domain to minimize the discrepancies between plots with different values for the same fixed variables. This is intended to allow better understanding of the model as a whole.

For all of the plots in this study, a positive heading angle means the bow of the UUV is pointed away from the submarine. Likewise, the yawing moment is positive when it causes the bow of the UUV to rotate away from the submarine and the sway force is positive when it pushes the UUV away from the submarine. The following plots show how the sway and yaw coefficients are affected by changes in heading angle and speed while keeping the other four input variables fixed at their specified values.

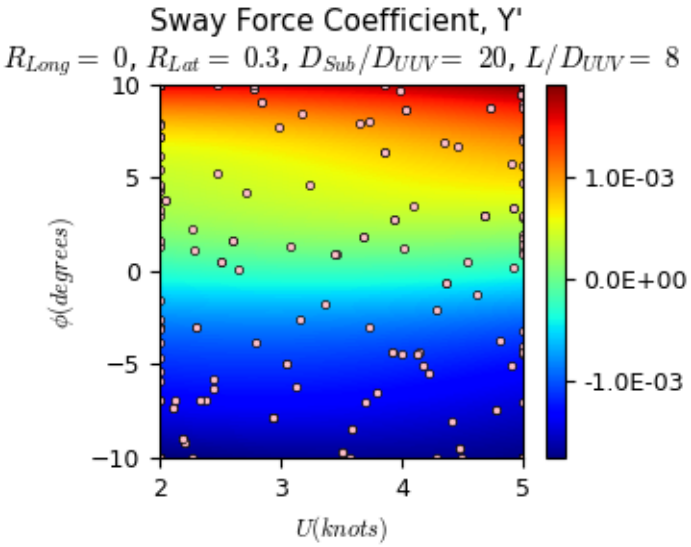

Figure 24: Sway Force Coefficient at Various Heading Angles and Speeds at Specified Fixed Input Variables

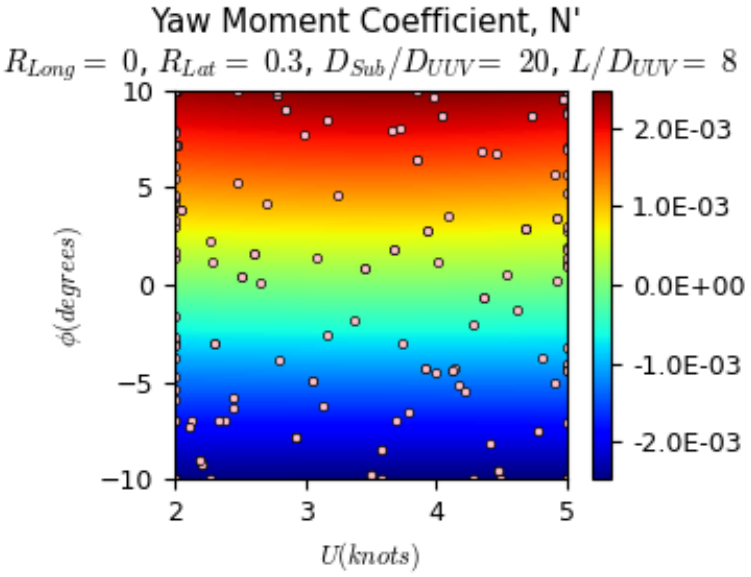

Figure 25: Yawing moment Coefficient at Various Heading Angles and Speeds at Specified Fixed Input Variables

The impact of the heading angle and speed on the sway and yaw coefficients was consistent with expectations of slender bodies. Much like how airfoils experience near linear increases in lift as angle of attack is increased below the point of flow separation, the UUV experienced similar near linear dependency of the sway and yaw coefficients on the heading angle. This is consistent with literature and findings in section 2.2.4 [29], [38]. The heading angle across this domain has a larger impact on the magnitude of the output variables than any of the other input variables. Additionally, because the sway and yaw coefficients were non-dimensionalized based on speed, these outputs were expected to be nearly independent of speed. These plots show that the speed of the UUV has little impact on the output variables.

The figure below shows how the surge coefficient is impacted by the L/D_{UUV} and the D_{Sub}/D_{UUV}. This domain of this specific plot was also constrained as discussed in section 4.3.

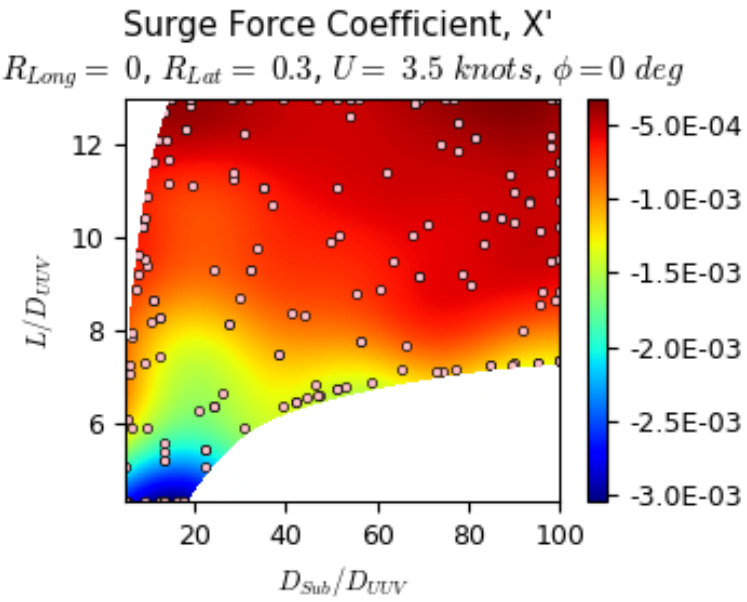

Figure 26: Surge Force Coefficient at Various L/D_{UUV} and D_{Sub}/D_{UUV} at Specified Fixed Input Variables

This figure illustrates the impact of the L/D_{UUV} on the surge force coefficient of the UUV. As shown in Figure 2, when the L/D_{UUV} is relatively small, the UUV acts like a bluff body and the form drag force becomes very large. As the UUV becomes longer, it acts more like a slender body which cases the form drag to decrease while the skin friction force increases. This results in an optimal L/D ratio for parallel midbody vessels around seven or eight. Unlike Figure 2, the figure above shows the surge force coefficient rather that the total drag. This means that the results were non-dimensionalized by the square of the length of the UUV. As such, the characteristic minimum at an L/D_{UUV} of seven or eight is not seen in this figure although this illustration represents the same phenomenon.

The previous plots have shown how the L/D_{UUV} and heading angle have large impacts on the output variables and tend to dominate other input variables like speed and D_{Sub}/D_{UUV}. The L/D_{UUV} and heading angle interaction is illustrated in the figures below.

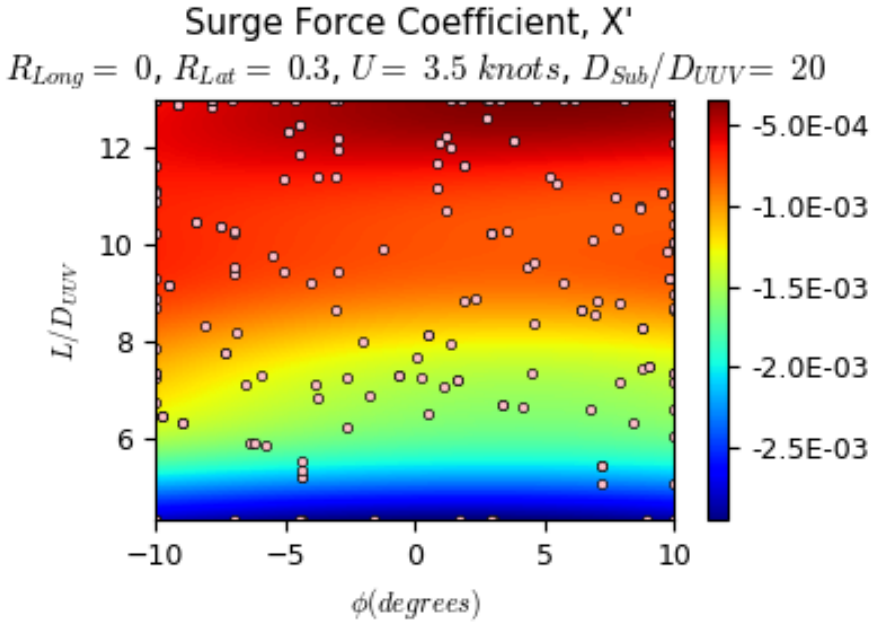

Figure 27: Surge Force Coefficient at Various L/D_{UUV} and Heading Angles at Specified Fixed Input Variables

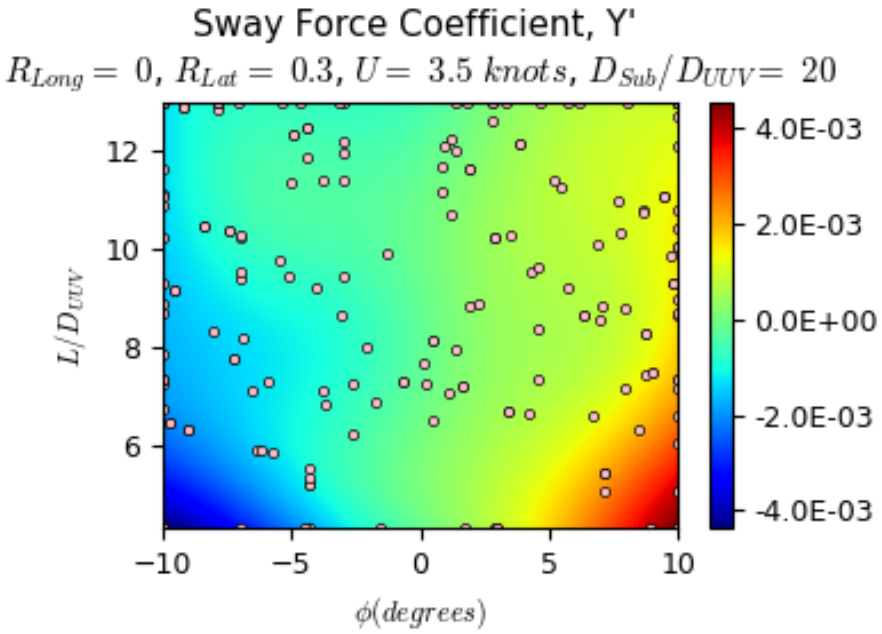

Figure 28: Sway Force Coefficient at Various L/D_{UUV} and Heading Angles at Specified Fixed Input Variables

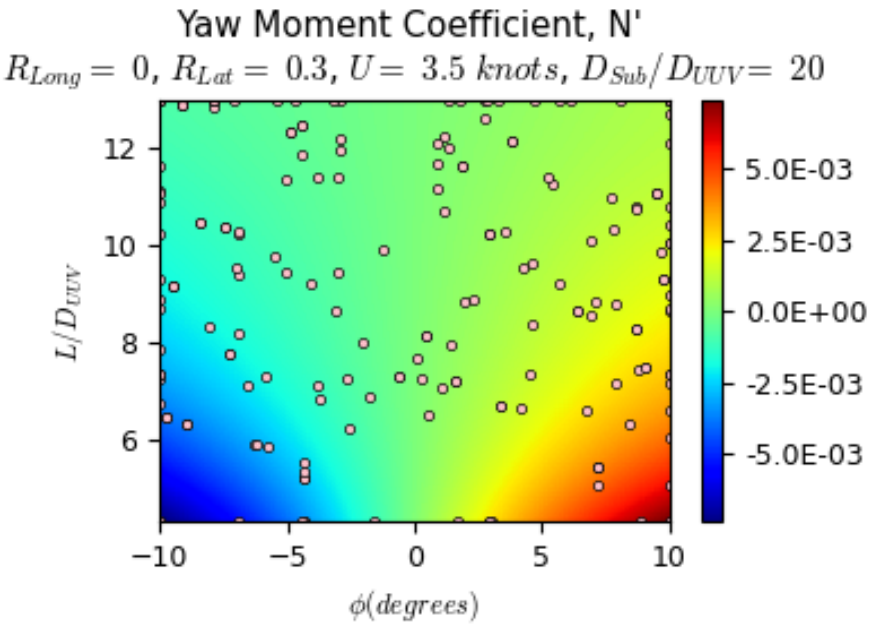

Figure 29: Yaw Moment Coefficient at Various L/DUUV and Heading Angles at Specified Fixed Input Variables

Once again, the model shows that the surge force coefficient decreases as the L/D_{UUV} increases. Additionally, the model predicts that the heading angle will not have a large impact on the surge force coefficient. This is consistent with Figure 14. As for the sway and yaw coefficients, both of them again show how the outputs vary nearly linearly with the heading angle. However, in these plots, the steepness of the slope of the relationship between the heading angle and the outputs decreases as the L/D_{UUV} increases. When the L/D_{UUV} is small, the heading angle has a large impact on the sway and yaw coefficients. When the L/D_{UUV} is very large, the heading angle has a much smaller impact on the outputs. When the sway and yaw coefficients were dimensionalized, this trend meant that the longer UUVs at a non-zero heading angles generated larger sway forces and yaw moments than shorter UUVs.

The design space of this study was much more vast than previous explorations of the hydrodynamic interactions between submarines and UUVs. As such, there is very little EFD validated data against which the model can be tested. Leong conducted a study that performed EFD validation of CFD models of a simulation between a submarine and UUV with a D_{Sub}/D_{UUV} of 2.239 [3]. This was much smaller than any simulations explored in this study. Leong used this small of a ratio because of the experimental constraints discussed in section 1.3.1. While Leong

was only able to use EFD validation on the simulations with a ratio of 2.239, he also performed CFD simulations on a ratio of 14.634. This overlapped a small portion of the domain used in this study, although, the heading angle, L/D_{UUV}, and Re_{Sub} were fixed at zero, 8.575, and $9.49x10^7$ respectively while this study explored the effects of varying heading angle, L/D_{UUV}, and speed. Overall, the results of Leong's study cannot be used to directly validate this model, but some of the trends and values that Leong discovered are also predicted by the GP model. The figures below show some of the trends confirmed by Leong. The figures below show the results of the sway coefficient. The yaw coefficient results were very similar.

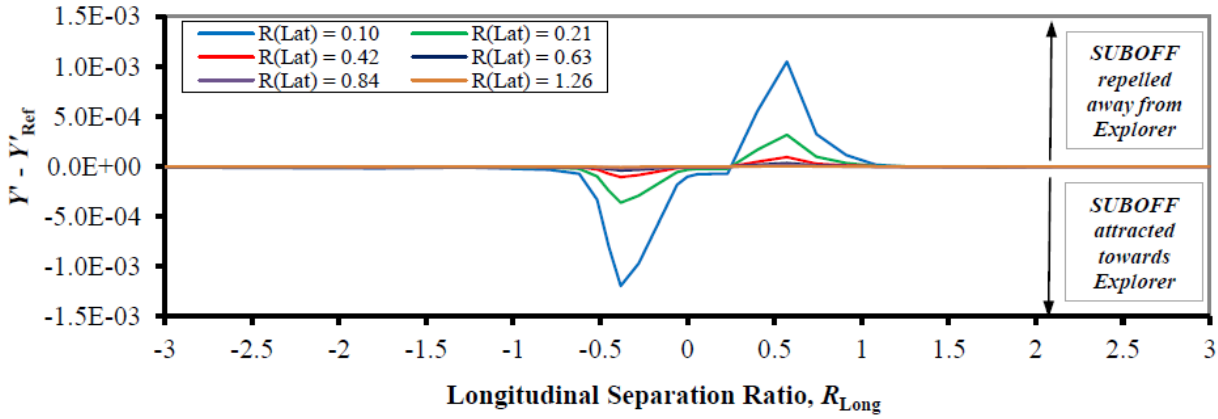

Figure 30: Sway Force Coefficient at Various R_{Long} and R_{Lat} with D_{Sub}/D_{UUV} = 14.634, L/D_{UUV} =8.575, φ = 0 degrees, Re_{Sub} = $9.49x10^7$, and Re_{UUV} = $7.68x10^6$ [3].

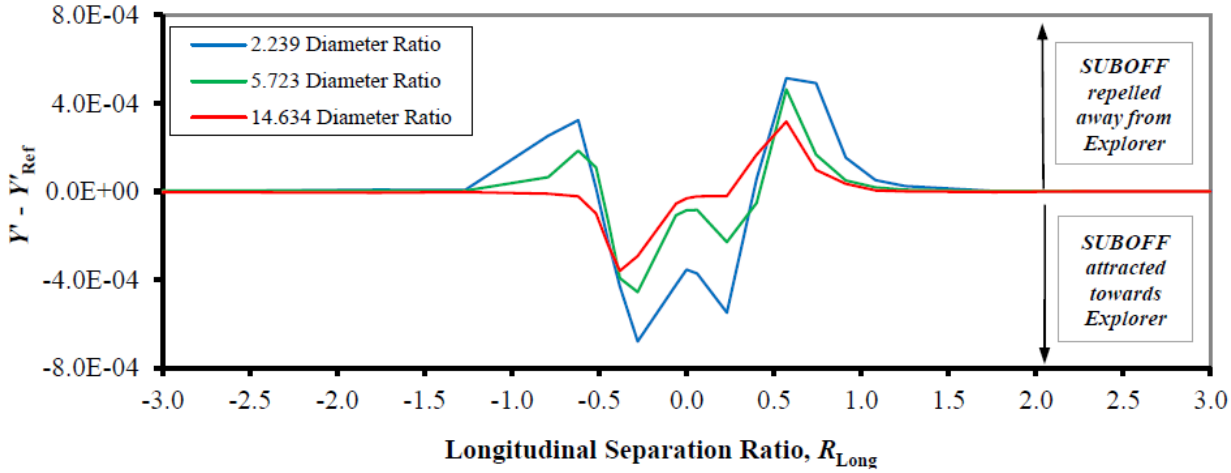

Figure 31: Sway Force Coefficient at Various R_{Long} and D_{Sub}/D_{UUV} with R_{Lat} = 0.21, L/D_{UUV} =8.575, φ = 0 degrees, and Re_{Sub} = $9.49x10^7$[31].

The following plot shows how the GP model predicts the R_{Lat} and D_{Sub}/D_{UUV} will impact the sway force coefficient.

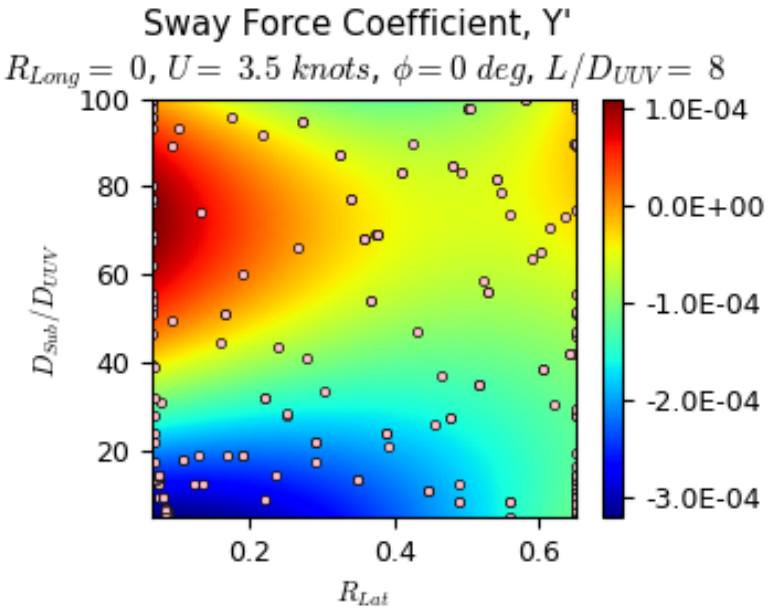

Figure 32: Sway Force Coefficient at Various D_{Sub}/D_{UUV} and R_{Lat} at Specified Fixed Input Variables

The figure above shows two trends that were confirmed by Leong and illustrated in both Figure 30 and Figure 31. When the R_{Long} and heading angle were both zero, at a small D_{Sub}/D_{UUV} and R_{Lat}, there was a sway force that pulled the UUV toward the submarine. Leong showed that as the D_{Sub}/D_{UUV} or R_{Lat} increased, this sway force decreased. The GP model showed the same sway scenario of comparable magnitude that pulled the UUV toward the submarine. The model also showed the trends that this force decreased in magnitude as the either the D_{Sub}/D_{UUV} or R_{Lat} increased.

While the model was able to capture some of the trends shown by Leong in Figure 30 and Figure 31, it was not able to match the complexity and subtlety of the effects of R_{Long} in this very small portion of the domain. The following figures shows the how model predicts the R_{Long} and R_{Lat} will impact the sway and yaw coefficients.

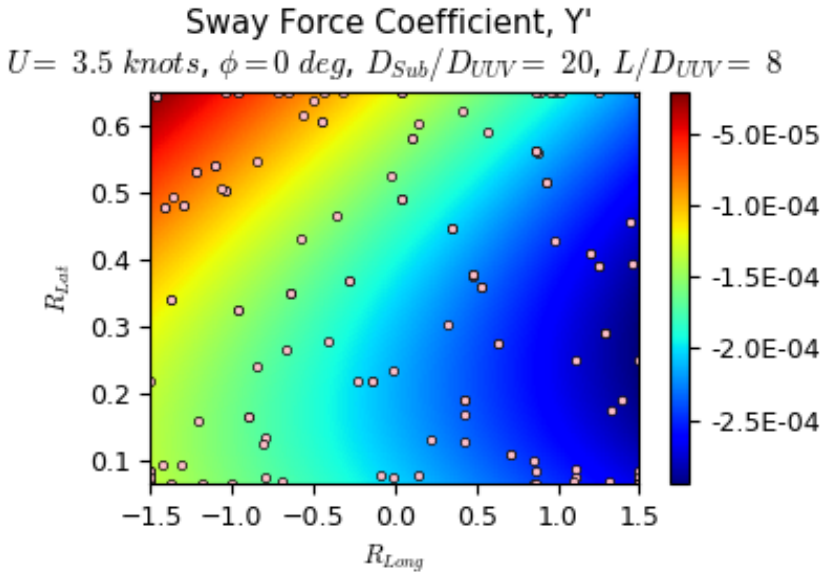

Figure 33: Sway Force Coefficient at Various R_{Long} and R_{Lat} at Specified Fixed Input Variables

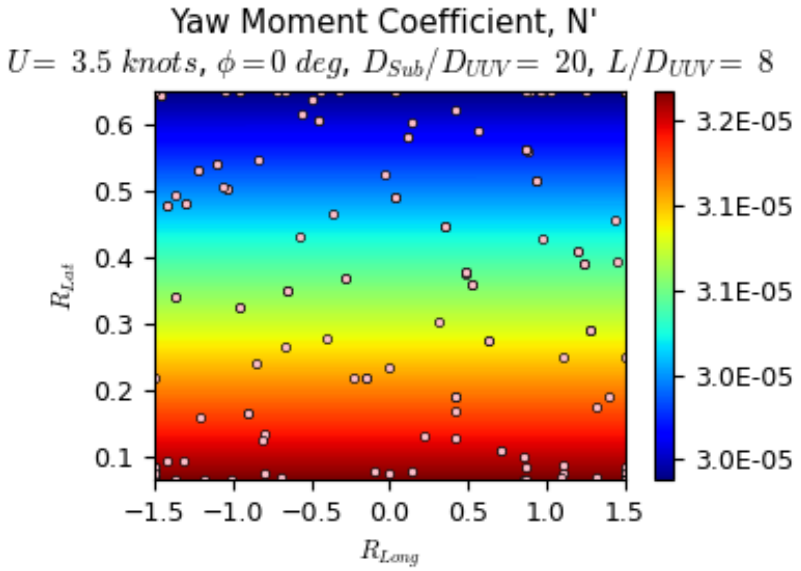

Figure 34: Yawing moment Coefficient at Various R_{Long} and R_{Lat} at Specified Fixed Input Variables

These figures show that the GP model does not predict the multiple local extrema and inflection points in R_{Long} as seen in Figure 30 and Figure 31. This is for a combination of multiple reasons. First, the size of the sway and moment coefficients within this region of the design space were one to two orders of magnitude smaller than those shown in Figures 24 to 29. The subtlety of these results compared to other regions of the design space, especially at large non-zero heading angles,

made these interactions difficult to predict. The small signal to noise ratio masks the true results within the uncertainty of the variables with larger impacts on the output variables. Also, this interaction only occurs at very small R_{Lat} and D_{Sub}/D_{UUV} and regions near the bow and stern, just off-center of the R_{Long} domain. Because there were areas in the design space with larger uncertainty, only about 5% of the simulations were in areas where these interactions would be large enough to have measurable impacts. This is likely much too scarce to accurately capture the complexity of this interaction that depends on three different input variables, contains multiple local extrema and inflection points, and requires the filtering of the other more significant effects. In order to overcome these challenges, the domain of the input variables could be reduced to this specific portion if the design space in future work. The heading angle could be reduced as to not dominate the output. Additionally, more simulations could be performed to allow enough data to reduce noise and capture the multiple local extrema and inflection points. Lastly, the difference in hull shapes between this study and the results produced by Leong may have an impact on the results. Leong's study used the Explorer and SUBOFF models as the submarine and UUV respectively. This study switched the models because the Explorer is an actual AUV while the SUBOFF model was created with the intention of modeling a submarine hull. The following plot shows the coefficient of pressure (C_p) between one of the simulations performed by Leong and a simulation conducted in the OED process that best matched Leong's setup. The Cp was clipped between -0.045 and 0.045 to better illustrate the pressure fields throughout the entire domain.

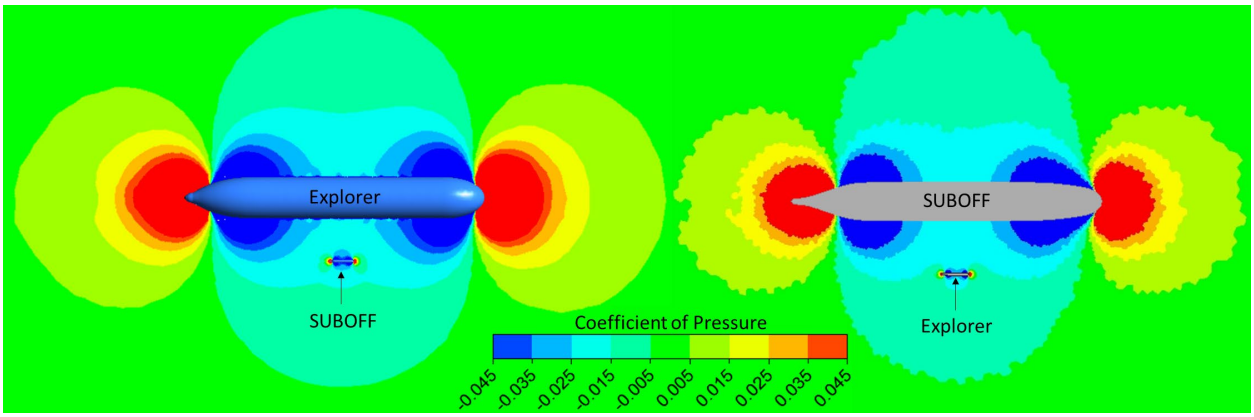

Figure 35: Coefficient of Pressure between Different Hull Geometries[3]

While the overall pressure fields look similar, there are some differences that have an impact on the forces and moments experienced by the UUV as a result of the hydrodynamic interaction

between the two vehicles. The bow of the SUBOFF model was designed to be more elongated than the ellipsoid bow of the Explorer in order to reduce the drag force. This more hydrodynamic design results in a low pressure field that is more contoured along the bow. A more contoured flow pattern reduces the impact on the UUV. The pressure gradient is much steeper just off the bow of the Explorer than it is off of the SUBOFF model. When a UUV is operating in this region, the bow of the UUV may experience a higher pressure while the stern experiences a lower pressure, resulting in a yawing moment that rotates the bow away from the submarine. Because the pressure gradient is reduced on the SUBOFF model, the resulting yawing moment is reduced. This difference in hull geometries acts as another factor in why the GP model struggled to capture all of the complexity of the interactions illustrated in Figure 30 and Figure 31.

In literature, the UUVs were often much larger than what could be considered for actual L&R operations with existing submarines. The effects of the bow and stern hydrodynamic interactions became much more relevant with an exaggerated UUV size. In this study, the UUVs were sized based on commercially available models, which made these hydrodynamic interactions much smaller than the impact of the heading angle in the majority of the studied domain. Throughout literature, the lateral separation between two vehicles was nondimensionalized by the larger vehicle's length or beam/diameter. The pressure field around a vehicle is affected within about one vehicle length. The general school of thought has been once the smaller vehicle enters the pressure field of the larger vehicle, the hydrodynamic interactions will begin. This has shown to have an impact but does not represent the entirety of the hydrodynamic interaction. When the smaller vehicle's pressure field is significantly altered by the larger vehicle's presence, this too has an impact. There is no separate parameter to measure this distance in terms of the smaller vehicle's size. This means the hydrodynamic interactions can change at the same lateral separation between two different sized vehicles so the model needs to capture this phenomenon as in interaction between these two input parameters. When the two vehicles are similar sizes, there is no need for this distinction. However, when one vehicle is substantially smaller than the other, this distinction becomes more important in understanding and mapping the hydrodynamic interactions.

4.5.2 Attempts at Model Improvement

The GP regression process uses length scale and variance hyperparameters to develop the model. These hyperparameters are optimized to make the model as accurate and precise as possible. These hyperparameters can be changed by either altering their initial values or using Bayesian inference. The initial values of the different hyperparameters were altered and the GP model was retrained. The data set was large enough and the optimizer was robust enough that varying the initial values of the hyperparameters had no impact on the results of the GP model. Rather than altering initial values, a prior statistical distribution could be assigned to each hyperparameter to alter the results of the model. Priors were formulated in order guide the model towards the complex subtle interaction that the model was not fully able to capture. When an prior Gaussian distribution of N(0.1,0.001) was used for the R_{Long} length scale hyperparameter, the model was able to predict some of the behavior illustrated in Figure 30. The figure below shows how the model predicts the yawing moment coefficient will be impacted by R_{Long} and R_{Lat}. The yawing moment coefficient had a very similar shape to Figure 30 and was shown rather than the sway force coefficient because the model was better able to predict this output.

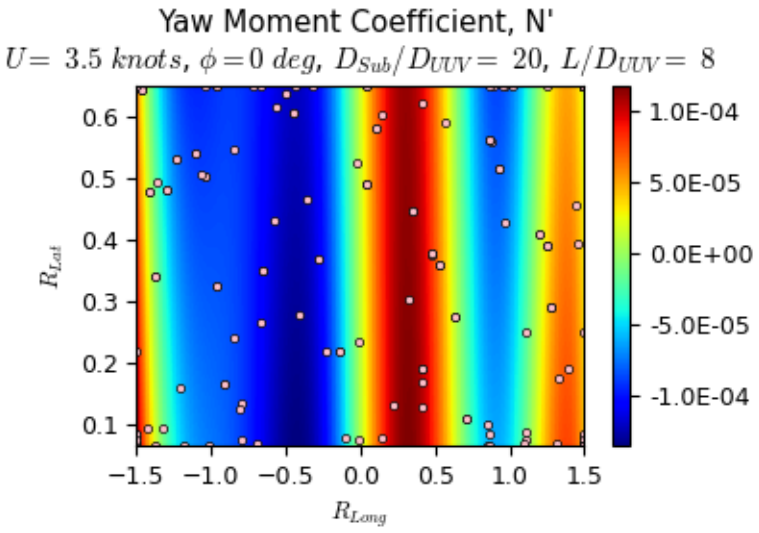

Figure 36: Yawing moment Coefficient at Various R_{Long} and R_{Lat} at Specified Fixed Input Variables with Prior Length Scale Distribution

By assigning a prior with a smaller value expected value, the optimizer solves for the ideal length scales while considering the assigned prior distribution on the R_{Long} variable. This allowed the

model to give the R_{Long} input the necessary flexibility to capture the complexity illustrated by Leong. Similar to Figure 30, the model predicts a positive peak around 0.35 and a negative peak around -0.45. Rather than asymptotically approaching zero as the $|R_{Long}|$ increases toward 1.5, the model over corrects and predicts oscillations as the output approaches zero. While this may better represent the R_{Long} parameter at this location in the design space, constraining the R_{Long} length scale hyperparameter with a prior introduced more error into the model. The model's accuracy in predicting the outputs based on the other input variables was reduced. For this reason, no priors were assigned to any hyperparameters for the final model.

GP regression models simulate an infinite number of basis functions, so they are capable of modeling an output function of any form without any prior knowledge of its general shape. This was a huge advantage in this study when the shape was unknown and complex as in this study. However, in the event that the form of an output function is known, there is no way to incorporate this information into the GP model. As such, a non-linear regression model was made to try and improve the accuracy of the GP model by using the trends of the GP model and the complexity of the outputs shown in Figure 30 and Figure 31 to predict the outputs. Several attempts at this non-linear model were conducted. A basis function for each input variable was represented as either exponential, power, polynomial, or, in the case of R_{Long}, an eight parameter function developed by Perez [10]. These functions were selected based on literature and results from the GP model. Each of these functions had several coefficients that would alter the shape to match the output. Several different non-linear combinations of these basis functions were optimized to try and find coefficients that would represent a model that would outperform the GP model. However, despite many attempts, and using the results of all of the figures above, the GP model was able to outperform any nonlinear models that were created. The nonlinear models were not able to accurately capture the complexity of the design space with the given data. Overall, this demonstrates just how beneficial the GP model was in conducting this study.

4.5.3 Model Validation and Error

An out of sample testing method was used to validate the GP model. Because the model becomes more accurate with more data, one randomly selected data point was removed from the 200 data points of CFD simulation results. The model was trained with the remaining 199 data points and

then used to predict the out of sample data point. The model's prediction of the output variables was then compared the actual CFD results. The data point was then replaced back into the training data and the process was repeated for a new random data point. This was performed on 30 different data points. This process was used because of the large amount of time and resources necessary to complete each simulation. Running 30 simulations for the purpose of validation without being able to use the results as training data would reduce the accuracy of the model. Additionally, during the OED process, the GP search algorithm selected the values of the input variables based on the locations in the domain that have the largest uncertainty. As such, every set of input variables that was used for the out of sample validation testing was selected because of the large amount of uncertainty at that point. This means that the model was more likely to have larger uncertainty at these points that randomly generated points within the input domain. This resulted in a more robust validation process.

GP models not only predict the output variables, but they also estimate the accuracy of their predictions. For each output variable prediction for a given set of input parameters, there is an associated variance of the model. This variance was used to create a 95 percent confidence interval for each predicted output. The figure below compares the GP model predicted outputs with their associated 95% confidence intervals to the actual CFD simulation data. These are the results for all three output variables for all 30 out of sample data points.

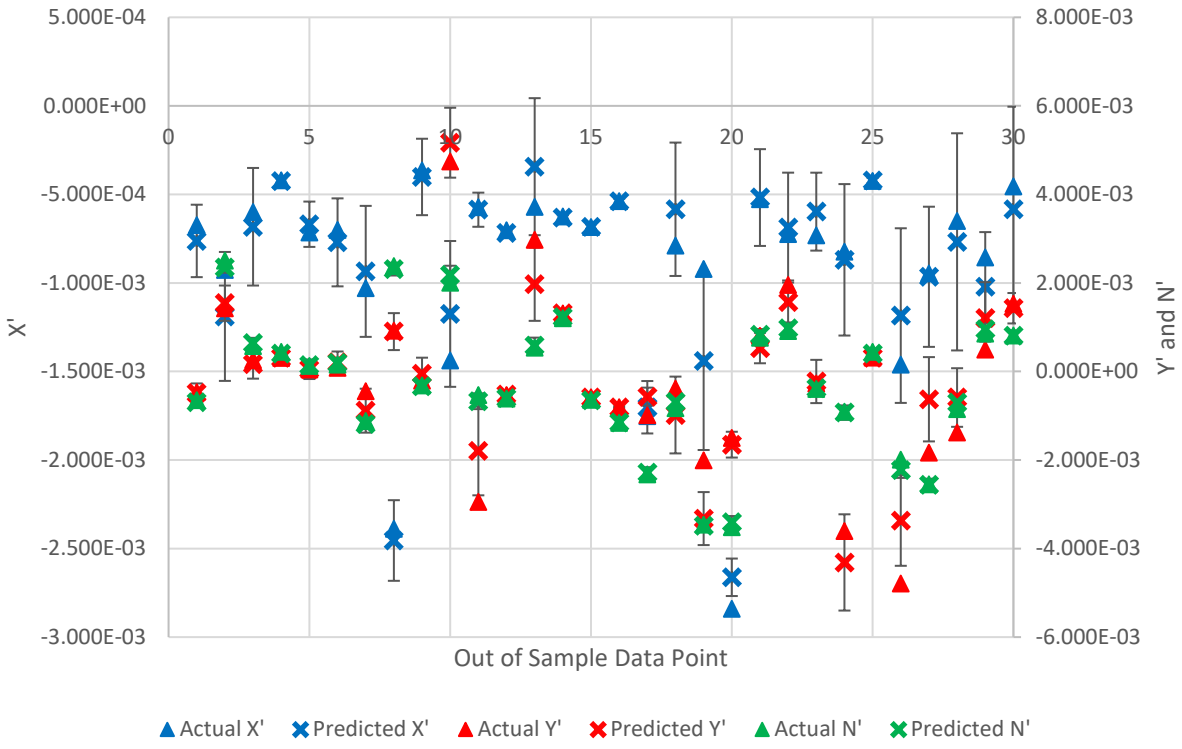

Figure 37: Gaussian Process Model Predicted Versus Actual Results of the Surge, Sway, and Yaw Force and Moment Coefficients for the Out of Sample Data Evaluation

Overall, the model was considered valid because it consistently predicted the output variables over a wide range of values within the 95% confidence interval. There were a handful of actual outputs that were outside of the 95% confidence interval but that is to be expected in a sample of 90 outputs.

While the model demonstrated that it was able to predict the output variables within its expected variance, the model was also checked for accuracy between the predicted and actual outputs of the out of sample data. The table below shows both the mean absolute error (MAE) and mean absolute percent error (MAPE) between the predicted and actual outputs. Another way to think of the MAE is in terms of the control system of the UUV and how capable it is to overcome and respond to these errors. This was done to help conceptualize the accuracy of the model. The sway and yaw coefficient MAE can be represented as an equivalent rudder angle difference $\Delta\delta_{eq,Y}$ or $\Delta\delta_{eq,N}$. This is how much the rudder angle would need to change to produce the force or moment equivalent to the MAE. If the UUV control system wanted to produce a force or moment at the predicted value, this is how much the rudder angle would need to change to become the actual value. Likewise, the

surge MAE can be thought of as a percentage of the propulsive force of the UUV (% X_{prop}). The hydrodynamic coefficients to compute these error equivalents were taken from the Remus 100 UUV [50].

Table 9: Error between GP Model Predicted and CFD Actual Outputs

Output	Mean Absolute Error	Mean Absolute Percent Error	Error Equivalents
X'	1.057E-04	12.30%	1.447% X_{prop}
Y'	3.906E-04	38.55%	$\Delta\delta_{eq,Y}$ = 0.961 degrees
N'	6.623E-05	7.94%	$\Delta\delta_{eq,N}$ = 0.343 degrees

Considering both the MAPE and the MAE are important. While MAPE illustrates accuracy with respect to the magnitude of the output, the MAE represents the difference between predicted and actual resulting forces and moments that will be experienced by the UUV. The magnitude of these forces and moments errors represented by MAE is what determines how the UUV will be impacted by the hydrodynamic interaction between the UUV and submarine. The MAPE can also be a little misleading when dealing with small forces and moments. As demonstrated in Table 6 and Figure 14, when the forces and moments are small, especially at very small heading angles, a small difference between the predicted and actual results can result in large percent error. For example, consider run 30 and run 199 which are two of the out of sample data points. Run 30 had a very small actual sway coefficient of Y' = 7.943E-05. The model predicted a value that was off by 1.323E-04 which was smaller than the MAE, but resulted in a percent error of 166.6%. This was the largest percent error in the validation study. Run 199 had a much larger actual sway force coefficient of Y' = 1.531E-03. The model was off by a similar amount of 1.018E-04, but resulted in a percent error of only 6.65%. Overall, the model was able to predict all three outputs with a relatively small MAE.

Chapter 5

5 Conclusions and Recommendations

5.1 Summary

The purpose of this study was to simulate the forces and moments due to the hydrodynamic interactions between a moving submarine and UUV operating in close proximity. The modeling of these forces and moments is vital to simulate the motion of these submerged bodies. Due to the complex nature of the hydrodynamic interactions, CFD was used to determine the surge, sway and yaw experienced by the UUV. The CFD methods were validated against as much EFD data as was available. Once the validated CFD methods were established, an OED was performed that used a GP search algorithm to design 200 different CFD simulations at various speeds, longitudinal positions, lateral positions, heading angles, and size differences between the two vehicles. The GP regression model was then trained to predict the surge, sway and yaw coefficients based on the different input variables. This model was validated using out of sample testing and checked for accuracy. The GP model was able to accurately predict the surge, sway, and yaw coefficients but struggled to capture some complex and subtle interactions in a narrow region of the design space. This was largely due to the sampling scarcity in this region and the subtlety of these interactions compared to regions that had larger impacts on the output variables.

5.2 Conclusions

The heading angle had the largest impact on the output variables compared to the other input variables. Even heading angles of a few degrees were able to produce larger sway forces and yawing moments than the extreme cases of the hydrodynamic interactions near the bow and stern of the submarine. The extent of the impact of the heading angle was largely dependent on the L/D_{UUV}. If the UUV had a smaller L/D_{UUV}, then the heading angle would have a larger impact on the nondimensionalized output variables. When the sway and yaw coefficients were dimensionalized, this trend meant that the longer UUVs at a non-zero heading angles generated larger sway forces and yaw moments than shorter UUVs. The model was also able to predict the

trend of how UUVs with a smaller L/D_{UUV} have much larger pressure drag. The speed of the vehicles had little discernable impact on the surge, sway, and yaw coefficients. Additionally, because the CFD was more accurate in determining the yawing moment than the sway force, the GP model was also better able to predict the yawing moment coefficient than the sway force coefficient.

When a UUV is operating near the bow and stern of the submarine, there can be a significant sway force and yawing moment caused by the hydrodynamic interaction between these two vehicles. However, these sway forces and yawing moments decreased drastically as the UUV decreased in diameter or increased in the lateral separation from the submarine. Because the range of UUVs in this study were much smaller than other studies in literature, the vast majority of the domain that was explored had results that were dominated by heading angle rather than these hydrodynamic interactions. The model was unable to predict these more subtle and complex interactions without a denser sampling in the small region of the domain where these forces and moments dominate. The lateral separation between the UUV and the submarine was nondimensionalized by the submarine length to be consistent with literature. This was chosen based on the concept that the pressure field is affected around the submarine within about one submarine length. While this does have an impact, the sway forces and yawing moments experienced by the UUV operating near the bow and the stern of the submarine tend to dominate when the lateral separation is on the order of the length of the UUV, rather than the length of the submarine. In literature, the UUVs were extremely large in order to be validated by EFD. This made the sway and yaw effects much more relevant throughout the domain. In this study, the UUVs were sized based on actually commercially available models which were substantially smaller than the submarine. As such, these sway forces and yawing moments were much subtler and the GP algorithm explored other areas of the domain with larger uncertainty, like heading angle and L/D_{UUV}.

5.3 Feasibility and Recommendations

The feasibility of the L&R of UUVs from submarines depends on many factors. Recovery operations are much harder to conduct because of the high degree of accuracy to which the UUV needs to maintain its course while combatting the hydrodynamic interactions between the two bodies. The control planes of the UUV have a major impact on whether the UUV will be able to

overcome these hydrodynamic interactions. In Leong's study, the SUBOFF model was used as the UUV. Roddy determined that the N' values due to the stern rudders being at a maximum angle of 15 degrees was approximately 7.0×10^{-4} [3], [38].

Leong determined that the UUV would need to be operated with heading angles less than two degrees different than the submarine when operating near the bow or stern. Beyond these angles, the rudders would not be able to provide enough of a moment to overcome the yawing moment due to the angle of attack. The additional yawing moment due to the hydrodynamic interactions near the bow and stern of the UUV would cause it to become uncontrollable beyond headlining angles of two degrees. However, different UUVs have different hydrodynamic coefficients. Using the REMUS 100 coefficients, the equivalent N' value due to the stern rudders being at a maximum angle of 15 degrees would be 2.89×10^{-3}, over four times larger than the SUBOFF model [50]. This yawing moment coefficient corresponds to a nine degree heading angle for the REMUS 100 UUV. This UUV is more maneuverable than the fully appended SUBOFF model and the control surfaces provide a much greater capability to overcome the forces and moments experienced at larger heading angles. Additionally, the REMUS 100 is at a D_{Sub}/D_{UUV} of 54.5 compared to the hull diameter of the Virginia class submarine. The forces and moments due to the hydrodynamic interactions near the bow and stern of the submarine for this small UUV are smaller than those experienced by a larger UUV. While the parallel midsection of the submarine is a region where these hydrodynamic interaction forces are minimal and provides a better L&R site, overcoming the forces and moments experienced near the bow and stern will not be as challenging for the smaller highly maneuverable UUVs. Overall, these smaller and more maneuverable UUVs provide a greater opportunity for successful L&R operations due to the capability of the control surfaces to overcome undesirable forces and moments and the fact that smaller UUVs experience smaller hydrodynamic interactions at a given lateral separation.

Whether the vehicles were traveling at a speed of two or five knots, there was a negligible difference in the surge, sway, or yaw coefficients. Even the smallest and slowest UUV had a large enough Reynolds number to be considered far into the turbulent regime. This meant there were no major differences in the boundary layer development to cause different frictional forces and flow separation between simulation. Because the speed had no significant impact on the hydrodynamic interactions between the vehicles, L&R operations may take place anywhere in this operating

envelope. Because submarine stability and UUV maneuvering responsiveness both increase as the speed increases, L&R operations are recommended to take place at speeds near the higher end of UUV capability.

When considering different L&R systems, the torpedo tubes, Virginia Payload Tubes (VPT), hangers, and other external mechanisms are options though with L&R is being considered. Many different L&R architectures would have external objects, like hangers, retractable machinery, or the submarine sail, that would have an impact on the flow. This study only looked at unappended vehicles so the effects of these objects were unexplored. In terms of the regions where the hydrodynamic interactions are less likely to interfere with the motion of the UUV, the parallel midbody section provides a region in which these interactions are smaller than areas near the bow or stern. However, smaller and more maneuverable UUVs have shown increased potential to overcome these hydrodynamic interactions. Additionally, L&R systems need to consider many design decisions like integration with existing submarine and UUV systems, communications, mission impact, UUV size and mission limitations, cost, risk, etc. The impact of the hydrodynamic interaction forces and moment on the L&R of a UUV should be evaluated in conjunction with these other criteria before making any design decisions.

5.4 Future Work

There are many avenues of future work that arise from this study. The following list discusses different areas of of study that may be explored to expand the current understanding of the problem.

- *Improve the Ability of the Model* – Because the sway force and yawing moment hydrodynamic interactions near the bow and stern were very subtle in the vast majority of the domain, the GP model was not able to capture all of the complexity of this interaction. For future work, the domain could be drastically reduced to focus on the region where these forces and moments tend to dominate.
- *Different Hulls for the UUV and Submarine* – In chapters 2 and 3, the submarine was represented by the Explorer AUV hull geometry while the UUV was represented by the DARPA SUBOFF model. This was done to align with available EFD studies to validate

the CFD simulations. In chapter 4, the models were switched so that the SUBOFF model was the submarine and the Explorer AUV model was the UUV. This switch was performed to more accurately reflect the actual geometries of a real submarine and UUV. Different hull geometries of different submarine and UUV models could be used to more accurately reflect a specific UUV and submarine hull.

- *Bow Force and Moment Exploration* – This study did not explore any UUV positions that were forward of the submarine and within the length of the radius of the submarine from the submarine's centerline. Because the L&R of UUVs from torpedo tubes is a real consideration, refining and further exploring the hydrodynamic interactions along the bow of the submarine would be valuable to enable this capability.
- *Transients Analysis* – This work was performed with the submarine and UUV traveling at the same speed. L&R operations require these vehicles move at different speeds. This study assumed that the relative speed between the two vehicles was small enough that the forces would be very similar to those experienced if the two vehicles were moving at the same speed. This would allow motion could be simulated as quasi-static. The model could be extrapolated to account for transient analysis by applying the results from EFD Leong data to the parameterization like performed by Perez [3], [10]. Additionally, the simulations and modeling could be reperformed to capture the relative speed between the vehicles.
- *Simulation and Incorporation into UUV Autonomy* – Now that the forces and moments have been successfully mapped, they can be incorporated into the equations of motion to see how a UUV would respond when it experiences these forces and moments. The UUV autonomy could be adapted to anticipate these forces and moments to enable the vehicle to become controllable in the wake and pressure field of the submarine [3].
- *Large Heading Angle Sway Corrections* – Because the EFD validation showed that the CFD was less accurate at predicting sway forces at angles more than 5 degrees, further work could be done the try and improve the accuracy in this area. The UUV could be kept at heading angles less than 5 degrees during L&R operations to avoid this problem but improving accuracy without restricting performance is the better approach. Additionally, the large heading angle had the tendency to dominate the other input variables. This caused the model to spend less time exploring some of the more complex and subtle interactions

of the other input variables. More simulations could be run within a smaller domain to help capture these subtleties and improve accuracy.

- *Communication* – How the UUV determines its position relative to the submarine was considered beyond the scope of this study. However, these inputs are necessary for the UUV to be able to anticipate the forces and moments that it will experience when operating in close proximity to a moving submarine. Future work may include how the UUV determines its relative position from the submarine and how it feeds that into its autonomy architecture.
- *Appendages and Propellers* – This study used bare hulls with no propellers to model the submarine and UUV. Appendages like the control surfaces and sail will have a significant impact on the forces experienced by the UUV in certain regions. The propeller sucks in water from around the hull which can cause the boundary layer separation to occur farther down the hull and reduce the effects of the adverse pressure gradient on the stern of the submarine and UUV. This could change the hydrodynamic forces experienced by the vehicle. The CFD simulations could be improved to incorporate these appendages and propellers.
- *Additional EFD validation* – The EFD that has been performed involving the hydrodynamic interactions between a submarine and UUV is very limited for reasons discussed in section 1.3.1. Much more EFD could be performed to validate the results of this study, especially at much larger submarine to UUV diameter ratios.

6 Bibliography

[1] J. A. Walsh and R. M. Smith, “The Navy Unmanned Undersea Vehicle (UUV) Master Plan.” United States Navy, Nov. 09, 2004.

[2] P. Small, “Unmanned Maritime System Update,” Jan. 15, 2019.

[3] Z. Q. Leong, “Effects of Hydrodynamic Interaction on an AUV Operating Close to a Moving Submarine,” p. 192.

[4] K. S. Varyani’ and M. Vantorre’, “New Generic Equation for Interaction Effects on a Moored Containership Due to a Passing Tanker,” *JOURNAL OF SHIP RESEARCH*, p. 11, 2006.

[5] K. M. Byrne, “Real-time modeling of cross-body flow for torpedo tube recovery of the Phoenix Autonomous Underwater Vehicle (AUV),” p. 241.

[6] R. Burcher and L. J. Rydill, *Concepts in Submarine Design*. Cambridge University Press, 1995.

[7] M. Moonesun, A. Mahdian, Y. M. Korol, M. Dadkhah, M. M. Javadi, and A. Brazhko, “Optimum L/D for Submarine Shape,” *INDIAN J. MAR. SCI.*, vol. 45, no. 1, p. 6, 2016.

[8] M. Moonesun, “INTRODUCTION OF IRANIAN HYDRODYNAMIC SERIES OF SUBMARINES (IHSS),” p. 9.

[9] D. E. Alexander, “3.1.4 The Reynolds Number,” p. 38.

[10] T. Perez, A. Donaire, and F. Valentinis, “Parametric Modelling of Interacting Hydrodynamic Forces in Underwater Vehicles Operating in Close Proximity,” *IFAC-PapersOnLine*, vol. 51, no. 29, pp. 92–97, 2018, doi: 10.1016/j.ifacol.2018.09.475.

[11] R. Fedor, “Simulation of a Launch and Recovery of an UUV to an Submarine,” p. 62.

[12] A. M. Jaffe, “The Millennium Grand Challenge in Mathematics,” vol. 53, no. 6, p. 9, 2006.

[13] L. Eça and M. Hoekstra, “A procedure for the estimation of the numerical uncertainty of CFD calculations based on grid refinement studies,” *Journal of Computational Physics*, vol. 262, pp. 104–130, Apr. 2014, doi: 10.1016/j.jcp.2014.01.006.

[14] J.-Y. Park, B. Jun, P. Lee, and J. Oh, “Development of Test-Bed AUV ‘ISiMI’ and Underwater Experiments on Free Running and Vision Guided Docking,” in *Underwater Vehicles*, A. V., Ed. InTech, 2009.

[15] M. Mackay, “Estimation of Submarine Near-Bottom Hydrodynamic Loads and Squat,” p. 54.

[16] “Report of the Resistance and Flow Committee,” Sep. 1990.

[17] “Captive Model Test Procedures,” Sep. 2014.

[18] R. O’Rourke, “Navy Columbia (SSBN-826) Class Ballistic Missile Submarine Program: Background and Issues for Congress,” p. 60.

[19] “1978 ITTC Performance Prediction Method,” Sep. 2017.

[20] “Overview of CFD Verification & Validation.” https://www.grc.nasa.gov/WWW/wind/valid/tutorial/overview.html (accessed Aug. 11, 2020).

[21] “Practical Guidelines for Ship CFD Applications,” Sep. 2014.

[22] C. M. Klaij and G. Vaz, “NUMERICAL UNCERTAINTY ESTIMATION IN MARITIME CFD APPLICATIONS,” p. 11.

[23] S. Toxopeus and G. Vaz, “Calculation of Current or Manoeuvring Forces Using a Viscous-Flow Solver,” presented at the 28th International Conference on Ocean, Offshore and Arctic Engineering (OMAE), Jul. 2010.

[24] M. Moonesun, Y. Korol, and H. Dalayeli, “CFD Analysis on the Bare Hull Form of Submarines for Minimizing the Resistance,” p. 16, 2015.

[25] M. Moonesun, Y. M. Korol, V. A. Nikrasov, A. Ursalov, and A. Brajhko, “CFD analysis of the bow shapes of submarines,” p. 16, 2016.

[26] F. R. Menter, “Two-equation eddy-viscosity turbulence models for engineering applications,” *AIAA Journal*, vol. 32, no. 8, pp. 1598–1605, Aug. 1994, doi: 10.2514/3.12149.

[27] X. Lyu, H. Tang, J. Sun, X. Wu, and X. Chen, “SIMULATION OF MICROBUBBLE RESISTANCE REDUCTION ON A SUBOFF MODEL.” Brodogradnja, Jun. 2014.

[28] D. A. Pook, D. B. Clarke, M. Jones, H. Quick, and D. Ranmuthugala, “RANS based CFD Prediction of Submarine Hydrodynamic Loads,” p. 4.

[29] K. Takahashi and P. K. Sahoo, “Fundamental CFD Study on the Hydrodynamic Performance of the DARPA SUBOFF Submarine,” in *Volume 2: CFD and FSI*, Glasgow, Scotland, UK, Jun. 2019, p. V002T08A052, doi: 10.1115/OMAE2019-96190.

[30] M. Moonesun, M. Javadi, P. Charmdooz, and K. U. Mikhailovich, “Evaluation of submarine model test in towing tank and comparison with CFD and experimental formulas for fully submerged resistance,” *INDIAN J. MAR. SCI.*, vol. 42, no. 8, p. 8, 2013.

[31] Z. Leong, K. Saad, D. Ranmuthugala, and J. Duffy, “Investigation into the Hydrodynamic Interaction Effects on an AUV Operating Close to a Submarine,” p. 11.

[32] J. F. Box, “R. A. Fisher and the Design of Experiments, 1922-1926,” p. 8, 2020.

[33] M. Friedman and L. J. Savage, “PLANNING EXPERIMENTS SEEKING MAXIMA,” in *Selected Techniques of Statistical Analysis for Scientific and Industrial Research, and Production and Management Engineering*, New York and London: McGraw-Hill, 1947, pp. 363–373.

[34] *Engineering Statistics Handbook*. National Institute of Standards and Technology, 2012.

[35] T. Hardy and G. Barlow, “Unmanned Underwater Vehicle (UUV) deployment and retrieval considerations for submarines,” p. 15, 2008.

[36] N. C. Groves, T. T. Huang, and M. S. Chang, “Geometric Characteristics of DARPA SUBOFF Models.” David Taylor Research Center, Mar. 1989.

[37] T. T. Huang, H.-L. Liu, and N. C. Groves, “Experiments of the DARPA SUBOFF Program.” David Taylor Research Center, Dec. 1989.

[38] R. F. Roddy, “INVESTIGATION OF THE STABILITY AND CONTROL CHARACTERISTICS OF SEVERAL CONFIGURATIONS OF THE DARPA SUBOFF MODEL (DTRC MODEL 5470) FROM CAPTIVE-MODEL EXPERIMENTS.” David Taylor Research Center, Sep. 1990.

[39] H.-L. Liu and T. T. Huang, “Summary of DARPA Suboff Experimental Program Data.” Naval Surface Warfare Center, Carderock Division, Jun. 1998.

[40] B. M. Duda, F. R. Menter, T. Hansen, and M.-J. Esteve, “Scale-adaptive simulation of a hot jet in cross flow,” *J. Phys.: Conf. Ser.*, vol. 318, no. 4, p. 042050, Dec. 2011, doi: 10.1088/1742-6596/318/4/042050.

[41] R. Pankajakshan, M. G. Remotigue, L. K. Taylor, M. Jiang, W. R. Briley, and D. L. Whitfield, “Validation of Control-Surface Induced Submarine Maneuvering Simulations using UNCLE,” p. 16.

[42] “Explorer AUV,” *International Submarine Engineering*. https://ise.bc.ca/product/explorer/ (accessed Sep. 08, 2020).

[43] A. Blanchard and T. Sapsis, *gpsearch*. MIT.

[44] C. E. Rasmussen and C. K. I. Williams, *Gaussian processes for machine learning*. Cambridge, Mass: MIT Press, 2006.

[45] “NSSN Virginia-Class Attack Submarine,” *Naval Technology*, Accessed: Jan. 08, 2021. [Online]. Available: https://www.naval-technology.com/projects/nssn/.

[46] “AUV System Spec Sheet.” AUVAC, Accessed: Jan. 08, 2021. [Online]. Available: https://auvac.org/226-2/.

[47] “Bluefin SandShark Unmanned Underwater Vehicle (UUV).” General Dynamics Mission Systems, Accessed: Jan. 08, 2021. [Online]. Available: https://gdmissionsystems.com/products/underwater-vehicles/bluefin-sandshark-autonomous-underwater-vehicle#:~:text=The%20Bluefin%20SandShark%C2%AE%20is,platform%20for%20the%20next%20generation.

[48] “IVER 3 AUV Specifications.” Ocean Server, Accessed: Jan. 08, 2021. [Online]. Available: https://auvac.org/files/uploads/platform_pdf/iver3_auv_brochure.pdf.

[49] K. Owens, “New Navy Class III Undersea Drone to be in the Water by 2019,” *Defense Systems*, Apr. 2017, Accessed: Jan. 08, 2021. [Online]. Available: https://defensesystems.com/articles/2017/04/06/uuv.aspx.

[50] N. E. Winey, *Modifiable Stability and Maneuverability of High Speed Unmanned Underwater Vehicles (UUVs) Through Bioinspired Control Fins*. Woods Hole, MA: Massachusetts Institute of Technology and Woods Hole Oceanographic Institution, 2020.

7 Appendix

7.1 Changes to the gpsearch code

The following code show the new main.py, utils.py, and post_pro.py files that were used in conjunction with the gpsearch code found at https://github.com/ablancha/gpsearch .

```
# file = main.py
# authors = Antoine Blanchard and Brady Hammond

import numpy as np
from utils import run_experiment


if __name__ == "__main__":

    # Parameter range
    domain = [ [ -1.5, 1.5],    # 0 - Longitudinal Position
               [ 0.064, 0.65], # 1 - Lateral Position
               [ 2, 5],         # 2 - Speed (knots)
               [ -10, 10],      # 3 - Heading Angle (degrees)
               [ 5, 100],       # 4 - Sub to UUV Diameter Ratio
               [ 4.3, 13] ]     # 5 - UUV L/D Ratio

    # (Non-negative) constraints for parameter values
    constraints = ({"type": "ineq", "fun": lambda x:  6.315*10.363*x[4]**(-1) + x[5] - 8},
                   {"type": "ineq", "fun": lambda x:  -5.675*10.363*x[4]**(-1) - x[5] + 17},
                   {"type": "ineq", "fun": lambda x:  8.575*x[1] - 0.5*x[4]**(-1) - 0.09377*x[4]**(-
1)*x[5] - 0.5241})

    # Number of random simulations for bootstrapping
    n_init = 6

    # Acquisition function for sample selection
    acquisition = "US"

    # Run sampling algorithm
    run_experiment(domain, constraints, n_init, acquisition)
```

```
# file = utils.py
# author = Antoine Blanchard and Brady Hammond

import numpy as np
import GPy
import random
from gpsearch import UniformInputs, RBF
from gpsearch.core.acquisitions.check_acquisition import check_acquisition
from scipy.optimize import minimize
from joblib import Parallel, delayed
from matplotlib import pyplot as plt


np.set_printoptions(precision=6)


def run_experiment(domain, constraints, n_init, acquisition, seed=2):
    """Optimize next experiment to run"""

    np.random.seed(seed)
    n_dim = len(domain)
```

```
    inputs = UniformInputs(domain)

    try:
        data = np.genfromtxt("previous_runs.dat")
        ss = " Found `previous_runs.dat` with %d data points! "%(len(data))
        print("-"*len(ss) + "\n" + ss + "\n" + "-"*len(ss))
        X = data[:,0:n_dim]
        Y = data[:,n_dim::]
        print("Training GP models...")
        models = train_gp(X,Y)
        idx = (X.shape[0]-n_init) % Y.shape[1] # Alternate between models
        acq = check_acquisition(acquisition, models[idx], inputs)
        print("Optimizing next sample using Y%d as target..."%(idx))
        xopt = funmin(acq.evaluate, acq.jacobian, inputs, constraints=constraints,
                      num_restarts=n_dim*10, parallel_restarts=True, n_jobs=10)
        print("Run the following simulation " \
              + "and manually append (X,Y) pair to `previous_runs.dat`:")
        print("   ", xopt)

    except:
        print("-"*18 + "\n Boostrap needed! \n" + "-"*18)
        print("Run the following %d simulations "%(n_init) \
              + "and manually write (X,Y) pairs to `previous_runs.dat`:")
       #X = inputs.draw_samples(n_init, "lhs")
        for ii in range(n_init):
            X = funmin(lambda x: 1, lambda x: np.zeros(x.shape), inputs,
                       constraints=constraints, num_restarts=20)
            print("   ", X)


def train_gp(X, Y):
    """Train one GP model for each output dimension"""
    model_list = []
    ker = RBF(input_dim=X.shape[1], ARD=True)
    # ker = RBF(input_dim=X.shape[1], ARD=True, lengthscale=[0.5,5,3.5,10,2,1], variance=10)
    for ii in range(Y.shape[1]):
        Yi = np.atleast_2d(Y[:,ii]).T
        m = GPy.models.GPRegression(X=X,
                                    Y=Yi,
                                    kernel=ker,
                                    normalizer=True,
                                    noise_var=0.0)
        # m.Gaussian_noise.variance.fix(0.0) # Fix noise if needed
        # Set Prior Expected Values and Variance
        # m.kern.lengthscale[[0]].set_prior(GPy.priors.Gamma.from_EV(1,0.1))
        # m.kern.lengthscale[[1]].set_prior(GPy.priors.Gamma.from_EV(1,0.1))
        # m.kern.lengthscale[[2]].set_prior(GPy.priors.Gamma.from_EV(10,0.5))
        # m.kern.lengthscale[[3]].set_prior(GPy.priors.Gamma.from_EV(10,1))
        # m.kern.lengthscale[[4]].set_prior(GPy.priors.Gamma.from_EV(2,0.08))
        # m.kern.lengthscale[[5]].set_prior(GPy.priors.Gamma.from_EV(1,0.1))
        # m.kern.variance.set_prior(GPy.priors.Gamma.from_EV(15,1.5))
        m.optimize_restarts(num_restarts=10, optimizer="bfgs",
                            max_iters=1000, verbose=False)
        model_list.append(m.copy())
        # print(m.rbf.lengthscale)
        # print(m.rbf.variance)
    return model_list


def funmin(fun, jac, inputs, constraints=(), args=(), kwargs_op=None,
           num_restarts=None, parallel_restarts=False, n_jobs=10):
    """Scipy-based minimizer allowing multiple parallel restarts"""

    if kwargs_op is None:
        kwargs_op = dict(options={"disp":False})

    if num_restarts is None:
        num_restarts = min(100, 10*inputs.input_dim)

    n_guess = num_restarts + 1
    x0 = inputs.draw_samples(n_guess, "lhs")
```

```
    if parallel_restarts:
        res = Parallel(n_jobs=n_jobs, backend="loky")(
                       delayed(minimize)(fun,
                                         np.atleast_2d(x0[i]),
                                         args=args,
                                         jac=jac,
                                         constraints=constraints,
                                         bounds=inputs.domain,
                                         **kwargs_op)
                       for i in range(x0.shape[0]) )

    else:
        res = [ minimize(fun,
                         np.atleast_2d(x0[i]),
                         args=args,
                         jac=jac,
                         constraints=constraints,
                         bounds=inputs.domain,
                         **kwargs_op)
                for i in range(x0.shape[0]) ]

    idx = np.argmin([r.fun for r in res])
    xopt = res[idx].x

    return xopt


def plot_results(domain, fixed_vars):
    """Visualize results with 2-D plots"""
    assert len(domain) == len(fixed_vars) + 2

    # Seed model
    seed_number = 11
    np.random.seed(seed_number)
    random.seed(seed_number)

    # Load models
    data = np.genfromtxt("previous_runs.dat")
    ss = " Found `previous_runs.dat` with %d data points! "%(len(data))
    print("-"*len(ss) + "\n" + ss + "\n" + "-"*len(ss))
    n_dim = len(domain)
    X = data[:,0:n_dim]
    Y = data[:,n_dim::]
    print("Training GP models...")
    models = train_gp(X,Y)

    # Make grid
    n_grid = 101
    fix_vars = [ v[0] for v in fixed_vars ]
    val_vars = [ v[1] for v in fixed_vars ]
    plt_vars = [ ii for ii in np.arange(n_dim) if ii not in fix_vars ]
    plt_doma = [ domain[ii] for ii in plt_vars ]
    grd = np.mgrid[ [slice(bd[0], bd[1], n_grid*1j) for bd in plt_doma] ]
    pts = (grd.T).reshape(-1, len(plt_vars))
    ones = np.ones((pts.shape[0],1))
    X_test = np.ones((pts.shape[0],n_dim))
    X_test[:,plt_vars] = pts
    X_test[:,fix_vars] = X_test[:,fix_vars] * val_vars

    # Create label
    string = ""
    separator = ", "
    for i in range(len(fix_vars)):
        txt = str(val_vars[i])
        if i == len(fix_vars) - 1:
            separator = ""
        if fix_vars[i] == 0:
            string = string + '$R_{Long} = $' + ' ' + '$' + txt + '$' + separator
        elif fix_vars[i] == 1:
            string = string + '$R_{Lat} = $' + ' ' + '$' + txt + '$' + separator
```

```
        elif fix_vars[i] == 2:
            string = string + '$U = $' + ' ' + '$' + txt + '$' + ' ' + '$knots$'+ separator
        elif fix_vars[i] == 3:
            string = string + '$\phi = $' + '$' + txt + '$' + ' ' + '$deg$' + separator
        elif fix_vars[i] == 4:
            string = string + '$D_{Sub}/D_{UUV}  = $' + ' ' + '$' + txt +'$' + separator
        elif fix_vars[i] == 5:
            string = string + '$L/D_{UUV}  = $' + ' ' + '$' + txt + '$' + separator

    # Plot results
    for ii in range(Y.shape[1]):
        plt.figure(figsize=(3.2,3))
        mu, var = models[ii].predict(X_test)
        np.savetxt('mu.txt', mu)
        pp = plt.imshow(mu.reshape((n_grid,)*len(plt_vars)),
                   extent=sum(plt_doma,[]), origin='lower', cmap='jet', aspect='auto')
        # cmap='RdYlBu' is good too
        plt.plot(models[ii].X[:,plt_vars[0]], models[ii].X[:,plt_vars[1]], 'o',
                 markersize=3, markerfacecolor="pink", markeredgecolor="k",
                 markeredgewidth=0.5)
        cbar = plt.colorbar(pp, orientation='vertical', format='%.1E')
        output = mu.reshape((n_grid,)*len(plt_vars))
        np.savetxt("x=x_" + str(plt_vars[0]+1)+"_y=x_" + str(plt_vars[1]+1)+"_F_" +
str(ii+1)+".txt", output)


        if plt_vars[0] == 0:
            plt.xlabel('$R_{Long}$')
        elif plt_vars[0] == 1:
            plt.xlabel('$R_{Lat}$')
        elif plt_vars[0] == 2:
            plt.xlabel('$U  (knots)$')
        elif plt_vars[0] == 3:
            plt.xlabel('$\phi  (degrees)$')
        elif plt_vars[0] == 4:
            plt.xlabel('$D_{Sub}/D_{UUV}$')
        elif plt_vars[0] == 5:
            plt.xlabel('$L/D_{UUV}$')

        if plt_vars[1] == 0:
            plt.ylabel('$R_{Long}$')
        elif plt_vars[1] == 1:
            plt.ylabel('$R_{Lat}$')
        elif plt_vars[1] == 2:
            plt.ylabel('$U  (knots)$')
        elif plt_vars[1] == 3:
            plt.ylabel('$\phi  (degrees)$')
        elif plt_vars[1] == 4:
            plt.ylabel('$D_{Sub}/D_{UUV}$')
        elif plt_vars[1] == 5:
            plt.ylabel('$L/D_{UUV}$')

        if ii == 0:
            plt.title("Surge Force Coefficient, X' \n" + string)
        elif ii == 1:
            plt.title("Sway Force Coefficient, Y' \n" + string)
        elif ii == 2:
            plt.title("Yaw Moment Coefficient, N' \n" + string)

        plt.tight_layout()
    plt.show()


def predict_results(domain, predict_vars):
    """Predict outputs at specified inputs"""
    assert len(domain) == len(predict_vars)
    input_vars = np.ones(shape=(2,len(predict_vars)))
    input_vars[0] = predict_vars
    input_vars[1] = predict_vars

    # Seed model
```

```
    seed_number = 11
    np.random.seed(seed_number)
    random.seed(seed_number)

    # Load models
    data = np.genfromtxt("previous_runs.dat")
    ss = " Found `previous_runs.dat` with %d data points! "%(len(data))
    print("-"*len(ss) + "\n" + ss + "\n" + "-"*len(ss))
    n_dim = len(domain)
    X = data[:,0:n_dim]
    Y = data[:,n_dim::]
    print("Training GP models...")
    models = train_gp(X,Y)
    print("Models Trained\n" "Input Varables\n" + str(predict_vars) + "\n" + "-
"*len(str(predict_vars)))

    # Predict results
    print("Output Varables" + "\n" + "mu and var for Y0, Y1, and Y2 respectively")
    mu_out = np.ones(len(range(Y.shape[1])))
    var_out = np.ones(len(range(Y.shape[1])))

    for ii in range(Y.shape[1]):
        mu, var = models[ii].predict(input_vars)
        mu_out[ii] = mu[0]
        var_out[ii] = var[0]

    print("%10.5E, %10.5E, %10.5E" % (mu_out[0], mu_out[1], mu_out[2],))
    print("%10.5E, %10.5E, %10.5E" % (var_out[0], var_out[1], var_out[2],))
```

```
# file = post_pro.py
# author = Antoine Blanchard and Brady Hammond

import numpy as np
from utils import plot_results
from utils import predict_results


if __name__ == "__main__":

    # Parameter range, same as in `main.py`
    domain = [ [ -1.5, 1.5],      # 0 - Longitudinal Position
               [ 0.064, 0.65],    # 1 - Lateral Position
               [ 2, 5],           # 2 - Speed (knots)
               [ -10, 10],        # 3 - Heading Angle (degrees)
               [ 5, 100],         # 4 - Sub to UUV Diameter Ratio
               [ 4.3, 13] ]       # 5 - UUV L/D Ratio

    # Creates a 2D plot by holding 4 of the six input variables as a constant
    # Specify variables to be kept constant as a list of (index, value)
    # fixed_vars = [ (2, 3.5), (3, 0), (4, 5), (5, 5) ]  # 1 - R_long vs R_lat
    # fixed_vars = [ (1, 0.3), (3, 0), (4, 20), (5, 8) ]  # 2 - R_long vs Speed
    # fixed_vars = [ (1, 0.3), (2, 3.5), (4, 20), (5, 8) ]  # 3 - R_long vs Angle
    # fixed_vars = [ (1, 0.3), (2, 3.5), (3, 0), (5, 8) ]  # 4 - R_long vs Diameter Ratio
    # fixed_vars = [ (1, 0.3), (2, 3.5), (3, 0), (4, 20) ]  # 5 - R_long vs UUV L/D
    # fixed_vars = [ (0, 0), (3, 0), (4, 20), (5, 8) ]  # 6 - R_lat vs Speed
    # fixed_vars = [ (0, 0), (2, 3.5), (4, 20), (5, 8) ]  # 7 - R_lat vs Angle
    # fixed_vars = [ (0, 0), (2, 3.5), (3, 0), (5, 8) ]  # 8 - R_lat vs Diameter Ratio
    # fixed_vars = [ (0, 0), (2, 3.5), (3, 0), (4, 20) ]  # 9 - R_lat vs UUV L/D
    # fixed_vars = [ (0, 0), (1, 0.3), (4, 20), (5, 8) ]  # 10 - Speed vs Angle
    # fixed_vars = [ (0, 0), (1, 0.3), (3, 0), (5, 8) ]  # 11 - Speed vs Diameter Ratio
    # fixed_vars = [ (0, 0), (1, 0.3), (3, 0), (4, 20) ]  # 12 - Speed vs UUV L/D
    # fixed_vars = [ (0, 0), (1, 0.3), (2, 3.5), (5, 8) ]  # 13 - Angle vs Diameter Ratio
    # fixed_vars = [ (0, 0), (1, 0.3), (2, 3.5), (4, 20) ]  # 14 - Angle vs UUV L/D
    # fixed_vars = [ (0, 0), (1, 0.3), (2, 3.5), (3, 0) ]  # 15 - Diameter Ratio vs UUV L/D

    # Plot results
    # plot_results(domain, fixed_vars)

    # Predict results at the following inputs
```

```
predict_vars = [ 1.5, 0.65, 5, 9.1, 54.54, 7 ]
predict_results(domain, predict_vars)
```

7.2 Raw Data from OED Simulations

Run	Long Ratio	Lat Ratio	Speed (knots)	Angle (Deg)	D_{sub}/D_{uuv}	L/D_{uuv}	X'	Y'	N'	Optimized Variable
1	8.77692E-01	5.59275E-01	3.08102E+00	1.36462E+00	7.38281E+01	1.19809E+01	-4.17583E-04	5.65024E-05	1.89956E-04	Random
2	-1.36556E+00	4.92977E-01	3.98474E+00	9.66988E+00	8.34310E+01	9.87772E+00	-6.12726E-04	1.63817E-03	1.48301E-03	Random
3	-1.42324E+00	9.33200E-02	4.90136E+00	-5.03410E+00	8.91009E+01	1.13602E+01	-6.73912E-04	-4.69831E-04	-6.47667E-04	Random
4	4.16718E-01	6.19378E-01	2.29323E+00	1.15613E+00	3.06719E+01	1.22462E+01	-5.91641E-04	8.22620E-05	1.48051E-04	Random
5	8.94140E-01	6.47373E-01	4.91164E+00	2.25330E-01	8.99686E+01	7.27261E+00	-1.21449E-03	4.55765E-05	8.63316E-05	Random
6	-8.46363E-01	2.39378E-01	4.41014E+00	-8.08423E+00	4.38666E+01	8.32869E+00	-7.84047E-04	-1.24708E-03	-1.89930E-03	Random
7	-2.64890E-02	5.22746E-01	3.36421E+00	-1.78168E+00	5.88165E+01	6.88735E+00	-1.39239E-03	-2.97995E-04	-6.22702E-04	X'
8	-1.43768E-01	2.18996E-01	2.77907E+00	9.76612E+00	3.21428E+01	9.31821E+00	-5.94773E-04	1.30099E-03	1.83216E-03	Y'
9	-1.22820E+00	5.29220E-01	2.11428E+00	-7.27855E+00	5.63986E+01	7.74492E+00	-9.10519E-04	-1.40847E-03	-1.90472E-03	N'
10	1.24505E+00	3.89231E-01	2.19059E+00	-8.98225E+00	2.43343E+01	6.34308E+00	-1.07054E-03	-1.79614E-03	-3.54529E-03	X'
11	-1.37169E+00	3.40099E-01	4.12650E+00	-4.43079E+00	7.74107E+01	1.24757E+01	-4.74254E-04	-2.97012E-04	-5.01569E-04	Y'
12	1.45221E-01	6.01890E-01	3.65510E+00	7.91053E+00	6.52652E+01	7.17239E+00	-9.26432E-04	1.42571E-03	2.50211E-03	N'
13	1.20105E+00	4.08997E-01	3.58144E+00	-8.40490E+00	8.32293E+01	1.04419E+01	-5.73122E-04	-1.17250E-03	-1.19724E-03	X'
14	-1.31832E+00	9.12170E-02	4.61064E+00	-1.25157E+00	4.96085E+01	9.89137E+00	-7.99262E-04	-1.17334E-04	-2.20228E-04	Y'
15	-4.54100E-01	6.03855E-01	2.83768E+00	9.02005E+00	3.85970E+01	7.48637E+00	-8.10727E-04	1.50421E-03	2.57679E-03	N'
16	-5.62485E-01	6.15230E-01	4.08641E+00	3.50388E+00	7.08863E+01	1.02643E+01	-5.99080E-04	2.56725E-04	5.74906E-04	X'
17	4.11990E-02	4.88035E-01	2.38012E+00	-6.94359E+00	8.70569E+00	1.02446E+01	-7.00542E-04	-7.99813E-04	-1.10003E-03	Y'
18	-1.29966E+00	4.79323E-01	2.60030E+00	1.61574E+00	8.48917E+01	7.22911E+00	-9.78902E-04	2.89507E-04	5.07683E-04	N'
19	-1.10939E+00	5.40725E-01	2.05350E+00	3.82875E+00	8.15936E+01	1.21396E+01	-4.20697E-04	3.08555E-04	4.45814E-04	X'
20	4.81781E-01	3.77422E-01	4.46640E+00	-9.52380E+00	6.91593E+01	9.13845E+00	-6.26969E-04	-1.34388E-03	-1.77130E-03	Y'
21	4.14320E-02	4.88076E-01	2.12828E+00	-6.94103E+00	1.25873E+01	4.30000E+00	-2.88959E-03	-2.96248E-03	-5.24917E-03	N'
22	9.73947E-01	4.25728E-01	2.98833E+00	7.66355E+00	8.96275E+01	1.09605E+01	-5.69776E-04	1.10180E-03	9.78839E-04	X'
23	1.43835E+00	4.56350E-01	2.70753E+00	4.16859E+00	2.63193E+01	6.62943E+00	-1.39191E-03	7.91402E-04	1.53353E-03	Y'
24	1.08108E-01	5.80310E-01	3.67536E+00	1.86678E+00	9.99825E+01	1.16198E+01	-4.00037E-04	9.09250E-05	2.69770E-04	N'
25	-2.81005E-01	3.68169E-01	3.93602E+00	2.78074E+00	5.39548E+01	1.25895E+01	-5.46323E-04	1.58659E-04	2.81465E-04	X'
26	-6.47197E-03	2.34764E-01	3.45238E+00	8.65115E-01	1.44936E+01	1.11700E+01	-7.15145E-04	4.55077E-05	1.28204E-04	Y'
27	1.45343E+00	3.92111E-01	3.15768E+00	-2.60643E+00	2.09686E+01	6.24602E+00	-1.54531E-03	-5.09704E-04	-1.07085E-03	N'
28	5.69131E-01	5.88357E-01	4.17577E+00	-5.08314E+00	6.35447E+01	9.46085E+00	-6.90488E-04	-4.90103E-04	-9.57556E-04	X'
29	3.18791E-01	3.02363E-01	4.21817E+00	-5.47479E+00	3.36174E+01	9.77496E+00	-7.90038E-04	-5.57080E-04	-8.91380E-04	Y'
30	-3.58018E-01	4.65019E-01	4.01266E+00	1.17639E+00	3.72287E+01	1.06968E+01	-7.00078E-04	7.94311E-05	1.51296E-04	N'
31	8.67392E-01	5.59937E-01	4.67818E+00	2.91901E+00	8.66394E+00	1.02121E+01	-7.08040E-04	2.40915E-04	5.04749E-04	X'
32	4.20544E-01	1.90918E-01	2.92970E+00	-7.85650E+00	1.90841E+01	1.28371E+01	-6.69143E-04	-5.78408E-04	-6.57524E-04	Y'
33	2.18916E-01	1.30217E-01	2.79893E+00	-3.81664E+00	7.42844E+01	7.11903E+00	-1.02976E-03	-4.45815E-04	-1.11468E-03	N'
34	8.66978E-01	5.60387E-01	4.67347E+00	2.91999E+00	5.27404E+00	4.30000E+00	-2.38872E-03	9.22504E-04	2.38157E-03	X'
35	-7.96154E-01	1.34813E-01	4.71972E+00	8.70442E+00	1.26205E+01	8.28823E+00	-1.00637E-03	1.44021E-03	1.99014E-03	Y'
36	1.32417E+00	1.72986E-01	4.34601E+00	6.87407E+00	9.54986E+01	1.01152E+01	-5.75290E-04	7.73987E-04	1.12160E-03	N'
37	-1.20418E+00	1.59605E-01	4.53012E+00	5.11088E-01	4.44480E+01	6.52767E+00	-1.47823E-03	2.09833E-04	1.89533E-04	X'
38	-5.80057E-01	4.29905E-01	4.45602E+00	6.71821E+00	4.71735E+01	6.61273E+00	-1.23562E-03	1.29624E-03	2.38264E-03	Y'
39	-6.66988E-01	2.65395E-01	2.65313E+00	9.57460E-02	6.61529E+01	7.65327E+00	-8.32023E-04	6.83739E-05	-7.88589E-05	N'
40	-1.04079E+00	5.00746E-01	2.29652E+00	-2.96813E+00	9.77104E+01	1.21990E+01	-3.89227E-04	-2.38458E-04	-3.51567E-04	X'
41	-8.44744E-01	5.46995E-01	4.90123E+00	5.69931E+00	7.87420E+01	9.22393E+00	-6.64853E-04	5.59157E-04	1.14862E-03	Y'
42	5.24658E-01	3.58723E-01	2.21409E+00	-9.16827E+00	6.79404E+01	1.28857E+01	-4.84798E-04	-1.28869E-03	-7.44263E-04	N'
43	-4.05800E-01	2.78127E-01	3.24514E+00	4.58850E+00	4.12881E+01	8.37093E+00	-8.49082E-04	4.64896E-04	9.75258E-04	X'
44	3.48158E-01	4.45031E-01	3.84887E+00	1.00000E+01	1.09994E+01	8.64658E+00	-9.59643E-04	1.89682E-03	2.13240E-03	Y'
45	1.28290E+00	2.90247E-01	2.00859E+00	1.00000E+01	1.73869E+01	4.30000E+00	-3.06338E-03	4.83883E-03	7.29789E-03	N'
46	1.28283E+00	2.90358E-01	2.00864E+00	7.15800E+00	2.22837E+01	5.42405E+00	-1.97811E-03	2.21085E-03	3.62824E-03	X'
47	1.50000E+00	2.49172E-01	2.47645E+00	1.00000E+01	2.83105E+01	1.30000E+01	-3.88408E-04	1.00018E-03	9.60942E-04	Y'

48	-2.85074E-01	3.68169E-01	3.93602E+00	2.77048E+00	5.39550E+01	1.30000E+01	-5.36418E-04	1.53365E-04	2.61644E-04	N'
49	1.10683E+00	8.51440E-02	2.44101E+00	-6.32273E+00	6.56481E+00	5.90908E+00	-1.40789E-03	-1.41140E-03	-2.84440E-03	X'
50	1.24675E+00	6.50000E-01	2.26389E+00	-1.00000E+01	1.63690E+01	4.30000E+00	-3.02194E-03	-4.67840E-03	-7.30763E-03	Y'
51	9.33092E-01	5.15063E-01	4.97259E+00	9.48887E+00	3.50988E+01	1.10688E+01	-6.25928E-04	1.31208E-03	1.19974E-03	N'
52	-1.04087E+00	5.00841E-01	2.29580E+00	-2.96814E+00	9.77545E+01	1.30000E+01	-3.65256E-04	-2.07492E-04	-3.13851E-04	X'
53	-1.50000E+00	6.40000E-02	5.00000E+00	1.00000E+01	1.00000E+02	1.30000E+01	-6.30547E-04	1.33908E-03	8.52601E-04	Y'
54	-1.46480E+00	6.41479E-01	3.50315E+00	-9.71815E+00	4.23710E+01	6.45549E+00	-1.01730E-03	-2.06672E-03	-3.67443E-03	N'
55	1.50000E+00	6.50000E-01	2.00000E+00	-1.00000E+01	1.09158E+01	1.16124E+01	-7.03176E-04	-1.39104E-03	-1.14495E-03	X'
56	1.50000E+00	6.40000E-02	4.28184E+00	-1.00000E+01	1.00000E+02	7.34558E+00	-1.00934E-03	-2.66406E-03	-2.68348E-03	Y'
57	-6.48867E-01	3.47941E-01	3.91378E+00	-4.32563E+00	1.34139E+01	5.18383E+00	-2.00826E-03	-1.13229E-03	-2.60231E-03	N'
58	-8.07655E-01	1.22876E-01	5.00000E+00	8.88470E+00	1.24225E+01	4.30000E+00	-2.72967E-03	3.40273E-03	6.64956E-03	X'
59	1.50000E+00	6.70750E-02	5.00000E+00	-1.00000E+01	1.76868E+01	4.30000E+00	-2.77258E-03	-4.24495E-03	-7.46929E-03	Y'
60	8.51571E-01	6.40000E-02	4.03726E+00	8.64026E+00	9.32143E+01	1.07727E+01	-5.50009E-04	1.20909E-03	1.14776E-03	N'
61	-1.50000E+00	8.39380E-02	5.00000E+00	-1.00000E+01	6.02271E+00	7.23529E+00	-1.05134E-03	-1.96332E-03	-2.96380E-03	X'
62	4.81556E-01	3.73913E-01	4.49404E+00	-1.00000E+01	6.92562E+01	1.30000E+01	-3.94567E-04	-9.86142E-04	-9.20567E-04	Y'
63	-1.00944E+00	6.43580E-02	3.16868E+00	8.43306E+00	3.94097E+01	6.33944E+00	-1.58877E-03	2.25361E-03	3.11725E-03	N'
64	-9.61818E-01	6.50000E-01	2.00000E+00	-1.00000E+01	1.00000E+02	8.68762E+00	-1.08359E-03	-4.23238E-03	-1.37871E-03	X'
65	-1.50000E+00	6.40000E-02	2.00000E+00	1.00000E+01	1.00000E+02	7.34558E+00	-1.43735E-03	4.74149E-03	2.00887E-03	Y'
66	1.31523E+00	6.75210E-02	2.00000E+00	5.40761E+00	2.83300E+01	1.12509E+01	-5.71549E-04	4.78280E-04	7.27796E-04	N'
67	8.67392E-01	6.50000E-01	5.00000E+00	1.00000E+01	1.36352E+01	1.26869E+01	-5.87721E-04	1.18469E-03	9.81142E-04	X'
68	-1.50000E+00	6.50000E-01	2.00000E+00	1.00000E+01	1.19845E+01	1.20928E+01	-6.73269E-04	1.34301E-03	1.05323E-03	Y'
69	4.20544E-01	1.28607E-01	2.92970E+00	-7.85288E+00	1.90807E+01	1.30000E+01	-7.78767E-04	-4.01588E-04	-5.14938E-04	N'
70	8.67398E-01	8.25650E-02	5.00000E+00	-1.00000E+01	7.25301E+00	8.89164E+00	-7.79126E-04	-1.59697E-03	-1.98542E-03	X'
71	-1.50000E+00	6.50000E-01	5.00000E+00	-1.00000E+01	1.47025E+01	1.30000E+01	-5.75496E-04	-1.14451E-03	-9.33474E-04	Y'
72	-7.16580E-01	6.50000E-01	4.81110E+00	-3.72056E+00	4.62456E+01	6.81276E+00	-1.36069E-03	-6.94249E-04	-1.35568E-03	N'
73	-1.50000E+00	6.50000E-01	5.00000E+00	1.00000E+01	5.00000E+00	5.05079E+00	-1.73565E-03	2.87939E-03	5.84420E-03	X'
74	1.50000E+00	6.40000E-02	2.00000E+00	-1.00000E+01	1.00000E+02	1.30000E+01	-5.71608E-04	-2.94389E-03	-5.31946E-04	Y'
75	4.11980E-02	6.50000E-01	2.33396E+00	-6.92810E+00	1.05151E+01	8.17030E+00	-1.05647E-03	-1.09875E-03	-1.69816E-03	N'
76	4.20544E-01	1.68570E-01	2.92895E+00	-7.85847E+00	1.90806E+01	1.30000E+01	-7.02793E-04	-5.32961E-04	-6.11665E-04	X'
77	9.73955E-01	6.50000E-01	2.00000E+00	1.00000E+01	1.00000E+02	1.30000E+01	-5.70846E-04	2.97047E-03	5.34375E-04	Y'
78	-1.46480E+00	6.50000E-01	3.50385E+00	-9.71921E+00	4.23709E+01	6.45549E+00	-1.01392E-03	-2.06279E-03	-3.67673E-03	N'
79	4.20544E-01	1.90918E-01	2.92970E+00	-7.85650E+00	1.90805E+01	1.30000E+01	-6.82989E-04	-5.84367E-04	-6.42581E-04	X'
80	-9.61821E-01	6.50000E-01	5.00000E+00	-1.00000E+01	1.00000E+02	1.30000E+01	-4.17995E-04	-1.26669E-03	-8.88163E-04	Y'
81	-7.96186E-01	7.29130E-02	4.73084E+00	8.70808E+00	1.26200E+01	8.27847E+00	-1.02238E-03	1.46084E-03	2.00298E-03	N'
82	6.36703E-01	2.73453E-01	4.36565E+00	-6.34457E-01	9.48926E+01	7.31035E+00	-1.18628E-03	-4.58695E-05	-1.04181E-04	X'
83	-1.50000E+00	6.50000E-01	2.00000E+00	2.98374E+00	5.00000E+00	4.30000E+00	-2.66609E-03	9.86176E-04	2.34772E-03	Y'
84	9.33092E-01	5.15063E-01	4.97259E+00	9.48887E+00	3.50988E+01	1.10688E+01	-6.24773E-04	1.30786E-03	1.20088E-03	N'
85	1.10683E+00	7.38250E-02	2.44101E+00	-5.76631E+00	9.64549E+00	5.87458E+00	-1.67819E-03	-1.29499E-03	-2.62312E-03	X'
86	-1.50000E+00	6.50000E-01	5.00000E+00	-1.00000E+01	1.00000E+02	7.34558E+00	-9.48155E-04	-2.41074E-03	-2.76624E-03	Y'
87	1.28283E+00	2.90358E-01	2.00864E+00	7.15800E+00	2.22837E+01	5.42405E+00	-1.96225E-03	2.20245E-03	3.62999E-03	N'
88	4.20544E-01	1.90918E-01	2.92970E+00	-7.85650E+00	1.90802E+01	1.30000E+01	-6.84242E-04	-5.84511E-04	-6.42601E-04	X'
89	1.50000E+00	6.40000E-02	2.00000E+00	1.35244E+00	1.00000E+02	1.30000E+01	-3.07182E-04	1.34868E-04	1.20936E-04	Y'
90	1.39666E+00	1.88262E-01	2.26997E+00	2.29660E+00	6.04055E+01	8.86021E+00	-6.72245E-04	1.71156E-04	5.37830E-04	N'
91	-9.25488E-03	7.39728E-02	3.45079E+00	8.64815E-01	1.44553E+01	1.16586E+01	-6.92994E-04	5.80464E-06	1.39177E-04	X'
92	1.50000E+00	6.50000E-01	5.00000E+00	1.00000E+01	1.00000E+02	1.30000E+01	-4.18853E-04	1.26157E-03	8.84521E-04	Y'
93	-6.48867E-01	3.47941E-01	3.91378E+00	-4.32563E+00	1.34139E+01	5.18383E+00	-2.01035E-03	-1.13024E-03	-2.60092E-03	N'
94	-1.06879E+00	5.03969E-01	2.00000E+00	-2.98061E+00	9.78806E+01	9.46052E+00	-5.83559E-04	-6.03845E-04	-4.78394E-04	X'
95	1.50000E+00	6.40000E-02	5.00000E+00	1.00000E+01	1.00000E+02	7.34558E+00	-9.46845E-04	2.39856E-03	2.76498E-03	Y'
96	-9.61811E-01	3.23644E-01	4.76954E+00	-7.45663E+00	8.69925E+01	1.03913E+01	-5.38650E-04	-8.07845E-04	-1.16378E-03	N'
97	1.50000E+00	6.40122E-02	5.00000E+00	1.00000E+01	6.93025E+01	1.30000E+01	-3.84355E-04	1.02003E-03	9.51331E-04	X'
98	1.50000E+00	6.50000E-01	5.00000E+00	-3.19035E+00	1.47025E+01	1.30000E+01	-5.64189E-04	-1.98080E-04	-3.33202E-04	Y'
99	-1.43768E-01	2.18996E-01	2.77907E+00	9.76612E+00	3.21428E+01	9.31821E+00	-6.10703E-04	1.34017E-03	1.82417E-03	N'
100	3.79690E-02	6.50000E-01	2.00000E+00	-6.95049E+00	9.40639E+00	9.38486E+00	-8.95436E-04	-9.36567E-04	-1.30120E-03	X'
101	-1.50000E+00	8.42930E-02	2.00000E+00	1.00000E+01	5.37844E+00	6.06559E+00	-1.51454E-03	2.69880E-03	4.06792E-03	Y'
102	-1.41871E+00	4.75604E-01	2.50939E+00	4.77126E-01	2.76181E+01	8.14490E+00	-1.01455E-03	6.02485E-05	1.17506E-04	N'
103	-6.48903E-01	3.47941E-01	5.00000E+00	-4.32564E+00	1.33777E+01	5.54793E+00	-1.75237E-03	-9.87179E-04	-2.32206E-03	X'
104	1.50000E+00	6.50000E-01	5.00000E+00	5.67909E+00	1.47025E+01	1.30000E+01	-5.70701E-04	4.35492E-04	5.77198E-04	Y'

105	3.48157E-01	4.45031E-01	3.84887E+00	6.37282E+00	1.09994E+01	8.64658E+00	-9.66602E-04	8.95440E-04	1.47173E-03	N'
106	-6.60591E-01	6.50000E-01	5.00000E+00	-4.32922E+00	1.33664E+01	5.36418E+00	-1.84781E-03	-1.03540E-03	-2.39986E-03	X'
107	1.50000E+00	6.50000E-01	2.00000E+00	-1.56456E+00	9.22509E+00	4.30000E+00	-2.66207E-03	-6.37908E-04	-1.19170E-03	Y'
108	7.03894E-01	1.08415E-01	3.04757E+00	-4.90961E+00	1.82424E+01	1.23345E+01	-6.14497E-04	-3.54339E-04	-5.27140E-04	N'
109	-1.04648E+00	6.50000E-01	2.00000E+00	-2.96813E+00	9.77301E+01	1.19385E+01	-3.98703E-04	-2.89047E-04	-3.53618E-04	X'
110	1.50000E+00	6.50000E-01	5.00000E+00	1.10214E+00	5.91605E+00	7.05925E+00	-1.09307E-03	1.47729E-04	3.80032E-04	Y'
111	-2.33696E-01	2.16247E-01	4.28184E+00	-2.05326E+00	9.17180E+01	7.99529E+00	-8.06310E-04	-2.12410E-04	-7.24434E-04	N'
112	4.11560E-02	4.88035E-01	2.00000E+00	-6.94359E+00	8.71933E+00	1.02552E+01	-8.09386E-04	-8.46010E-04	-1.09387E-03	X'
113	-1.50000E+00	6.50000E-01	5.00000E+00	-4.03699E+00	7.56147E+00	9.22241E+00	-7.88229E-04	-3.87422E-04	-8.28782E-04	Y'
114	1.28283E+00	2.90358E-01	2.00864E+00	7.15800E+00	2.22837E+01	5.42405E+00	-1.96927E-03	2.20595E-03	3.62798E-03	N'
115	-1.37178E+00	6.40000E-02	5.00000E+00	-4.43079E+00	7.74410E+01	1.18710E+01	-6.96205E-04	-3.96922E-04	-5.19233E-04	X'
116	1.02279E+00	6.50000E-01	2.00000E+00	6.14693E+00	2.83329E+01	1.30000E+01	-4.93473E-04	5.02706E-04	6.10889E-04	Y'
117	-9.06511E-01	1.65541E-01	4.91293E+00	3.38938E+00	5.09736E+01	6.71615E+00	-1.39137E-03	6.03530E-04	1.19327E-03	N'
118	1.50000E+00	7.95940E-02	5.00000E+00	-1.00000E+01	9.58853E+00	1.08666E+01	-6.61962E-04	-1.33553E-03	-1.33889E-03	X'
119	1.50000E+00	6.40000E-02	5.00000E+00	-1.00000E+01	5.28507E+01	6.76175E+00	-9.20933E-04	-2.00713E-03	-3.45959E-03	Y'
120	-9.52740E-02	7.72570E-02	3.12492E+00	-6.16599E+00	3.09135E+01	5.88306E+00	-1.66112E-03	-1.51285E-03	-2.80198E-03	N'
121	-1.50000E+00	2.18973E-01	2.00000E+00	1.00000E+01	8.94986E+00	1.04289E+01	-7.86508E-04	1.55407E-03	1.42382E-03	X'
122	1.09745E+00	6.77150E-02	2.00000E+00	-1.00000E+01	2.42462E+01	9.29166E+00	-5.73087E-04	-1.43201E-03	-1.85897E-03	Y'
123	5.24658E-01	3.58723E-01	2.21409E+00	-9.16827E+00	6.79404E+01	1.28857E+01	-4.84662E-04	-1.28870E-03	-7.44263E-04	N'
124	1.50000E+00	6.50000E-01	5.00000E+00	1.91764E+00	1.00000E+02	8.83754E+00	-7.06421E-04	1.22888E-04	4.54801E-04	X'
125	-3.22278E-01	6.50000E-01	5.00000E+00	-7.04980E+00	1.47025E+01	1.30000E+01	-5.72938E-04	-6.28267E-04	-7.06553E-04	Y'
126	-1.29970E+00	4.79500E-01	2.60009E+00	1.61577E+00	8.48918E+01	7.22911E+00	-9.74982E-04	2.93281E-04	5.08341E-04	N'
127	-6.96757E-01	6.89800E-02	5.00000E+00	-4.37508E+00	1.34008E+01	4.30000E+00	-2.83944E-03	-1.50152E-03	-3.51772E-03	X'
128	8.64562E-01	6.40720E-02	2.00000E+00	-3.79815E+00	6.19875E+01	1.14020E+01	-4.67817E-04	-2.69334E-04	-5.15755E-04	Y'
129	8.67447E-01	5.60264E-01	4.67868E+00	2.91907E+00	8.66400E+00	1.02121E+01	-7.12588E-04	2.46102E-04	5.04917E-04	N'
130	1.50000E+00	6.40000E-02	5.00000E+00	7.05241E+00	9.59453E+01	8.81924E+00	-6.84468E-04	8.93858E-04	1.51972E-03	X'
131	9.57325E-01	6.50000E-01	3.72229E+00	8.03229E+00	2.82354E+01	1.30000E+01	-5.27593E-04	8.05497E-04	7.61589E-04	Y'
132	1.08108E-01	5.80310E-01	3.67536E+00	1.86678E+00	9.99825E+01	1.16198E+01	-3.85260E-04	9.54641E-05	2.68516E-04	N'
133	1.50000E+00	6.50000E-01	2.00000E+00	-5.88985E+00	9.33371E+00	7.29426E+00	-1.23660E-03	-9.93837E-04	-1.80322E-03	X'
134	-1.50000E+00	6.40000E-02	2.00000E+00	7.90621E+00	5.55488E+01	8.79357E+00	-1.02013E-03	1.40688E-03	1.54796E-03	Y'
135	1.20105E+00	4.08997E-01	3.58144E+00	-8.40490E+00	8.32293E+01	1.04419E+01	-5.75589E-04	-1.18426E-03	-1.19537E-03	N'
136	1.50000E+00	6.62200E-02	2.00000E+00	7.15800E+00	2.22912E+01	5.06421E+00	-2.24678E-03	2.46318E-03	4.07447E-03	X'
137	-1.50000E+00	6.50000E-01	2.00000E+00	1.00000E+01	5.58825E+01	1.30000E+01	-4.74597E-04	1.60127E-03	7.95572E-04	Y'
138	4.81781E-01	3.77422E-01	4.46640E+00	-9.52380E+00	6.91593E+01	9.13845E+00	-6.31343E-04	-1.35940E-03	-1.77279E-03	N'
139	-1.50000E+00	6.48360E-02	5.00000E+00	2.82945E+00	5.39464E+01	1.30000E+01	-6.14068E-04	2.03063E-04	2.85411E-04	X'
140	-1.50000E+00	6.50000E-01	3.57326E+00	-1.00000E+01	1.94266E+01	1.11178E+01	-7.38455E-04	-1.47106E-03	-1.24999E-03	Y'
141	-5.00283E-01	6.36665E-01	3.79238E+00	-6.53928E+00	7.29632E+01	7.10308E+00	-9.61960E-04	-1.07775E-03	-2.16653E-03	N'
142	-1.50000E+00	7.22460E-02	5.00000E+00	8.77185E+00	1.25554E+01	7.44211E+00	-1.11652E-03	1.67181E-03	2.47376E-03	X'
143	1.50000E+00	6.50000E-01	2.00000E+00	-2.63397E+00	8.93119E+01	7.26726E+00	-1.14821E-03	-7.15200E-04	-7.36574E-04	Y'
144	-1.41871E+00	4.75604E-01	2.50939E+00	4.77126E-01	2.76181E+01	8.14490E+00	-1.01506E-03	6.06728E-05	1.17418E-04	N'
145	1.50000E+00	6.50000E-01	2.00000E+00	7.80026E+00	8.97099E+01	1.03140E+01	-7.24719E-04	1.95493E-03	9.15204E-04	X'
146	-4.35102E-01	6.50000E-01	5.00000E+00	1.00000E+01	4.70737E+01	6.60979E+00	-1.02382E-03	2.15018E-03	3.56360E-03	Y'
147	9.33092E-01	5.15063E-01	4.97259E+00	9.48887E+00	3.50988E+01	1.10688E+01	-6.35176E-04	1.32181E-03	1.19941E-03	N'
148	1.50000E+00	6.50000E-01	5.00000E+00	2.95067E+00	1.33745E+01	4.30000E+00	-2.69027E-03	1.00008E-03	2.33213E-03	X'
149	-1.18605E+00	6.40000E-02	3.73080E+00	-3.02185E+00	9.78292E+01	1.13728E+01	-7.30759E-04	-2.71941E-04	-3.90966E-04	Y'
150	1.24505E+00	3.89231E-01	2.19059E+00	-8.98225E+00	2.43343E+01	6.34308E+00	-1.07850E-03	-1.80861E-03	-3.54885E-03	N'
151	-1.50000E+00	6.89780E-02	4.14155E+00	-4.32563E+00	1.34029E+01	4.30000E+00	-2.73310E-03	-1.43756E-03	-3.34502E-03	X'
152	1.46772E-01	7.84550E-02	3.69195E+00	-6.96641E+00	9.36333E+00	9.51165E+00	-6.57973E-04	-1.08197E-03	-1.33867E-03	Y'
153	8.51571E-01	9.98680E-02	4.03726E+00	8.63450E+00	9.32142E+01	1.07622E+01	-5.48520E-04	1.23536E-03	1.14420E-03	N'
154	-1.50000E+00	6.50000E-01	3.99081E+00	-4.46130E+00	1.34082E+01	4.30000E+00	-2.73200E-03	-2.87852E-03	-3.48008E-03	X'
155	-1.50000E+00	6.40000E-02	2.00000E+00	-1.00000E+01	1.00000E+02	1.02102E+01	-8.23152E-04	-3.60622E-03	-9.11029E-04	Y'
156	-1.10939E+00	5.40725E-01	2.05350E+00	3.82875E+00	8.15936E+01	1.21396E+01	-4.24451E-04	3.11165E-04	4.46069E-04	N'
157	-1.50000E+00	6.73820E-02	2.77906E+00	1.00000E+01	3.20111E+01	1.30000E+01	-6.30883E-04	1.28411E-03	8.72134E-04	X'
158	-1.50000E+00	6.40000E-02	2.00000E+00	-1.00000E+01	1.00000E+02	7.34558E+00	-1.46148E-03	-4.78905E-03	-1.98986E-03	Y'
159	1.10647E+00	2.49489E-01	2.47672E+00	5.20948E+00	2.83645E+01	1.14134E+01	-5.94761E-04	4.65621E-04	6.80832E-04	N'
160	-1.50000E+00	7.48090E-02	5.00000E+00	9.14918E-01	1.39194E+01	1.20924E+01	-6.05220E-04	6.55253E-05	1.10119E-04	X'
161	1.50000E+00	6.50000E-01	5.00000E+00	1.00000E+01	1.00000E+02	1.08091E+01	-5.31433E-04	1.55855E-03	1.28244E-03	Y'

162	-9.61811E-01	3.23644E-01	4.76954E+00	-7.45663E+00	8.69925E+01	1.03913E+01	-5.38654E-04	-8.07793E-04	-1.16387E-03	N'
163	-1.50000E+00	6.50000E-01	2.00000E+00	-3.06974E+00	9.86114E+01	8.64409E+00	-8.12846E-04	-6.41518E-04	-6.12058E-04	X'
164	-1.50000E+00	6.40000E-02	2.00000E+00	4.29126E+00	1.00000E+02	9.53649E+00	-7.22073E-04	6.37426E-04	7.36587E-04	Y'
165	3.48157E-01	4.45031E-01	3.84887E+00	6.37282E+00	1.09994E+01	8.64658E+00	-9.66600E-04	8.95444E-04	1.47173E-03	N'
166	1.50000E+00	6.40000E-02	5.00000E+00	6.93568E+00	9.57233E+01	8.54228E+00	-7.14266E-04	8.99063E-04	1.59059E-03	X'
167	1.50000E+00	6.50000E-01	5.00000E+00	-1.00000E+01	5.00000E+00	4.30000E+00	-2.35616E-03	-3.55151E-03	-7.68431E-03	Y'
168	-4.54100E-01	6.03855E-01	2.83768E+00	9.02005E+00	3.85970E+01	7.48637E+00	-8.14658E-04	1.51348E-03	2.57540E-03	N'
169	1.50000E+00	6.62290E-02	5.00000E+00	-1.00000E+01	3.92339E+01	1.30000E+01	-4.97788E-04	-1.18015E-03	-8.96151E-04	X'
170	1.50000E+00	6.50000E-01	5.00000E+00	1.78048E+00	1.00000E+02	1.30000E+01	-4.58179E-04	9.06371E-05	1.92614E-04	Y'
171	5.24658E-01	3.58723E-01	2.21409E+00	-9.16827E+00	6.79404E+01	1.28857E+01	-4.84662E-04	-1.28870E-03	-7.44263E-04	N'
172	1.50000E+00	6.50000E-01	2.00000E+00	-1.00000E+01	5.13962E+01	1.10524E+01	-5.66579E-04	-1.84701E-03	-1.13219E-03	X'
173	1.50000E+00	6.50000E-01	5.00000E+00	-1.00000E+01	6.44136E+00	7.86993E+00	-9.46862E-04	-1.83549E-03	-2.54694E-03	Y'
174	-9.06410E-01	1.65449E-01	4.91262E+00	3.38947E+00	5.09736E+01	6.71615E+00	-1.38445E-03	6.05003E-04	1.19149E-03	N'
175	1.50000E+00	6.40000E-02	5.00000E+00	1.00000E+01	6.78329E+01	1.00552E+01	-5.28353E-04	1.35940E-03	1.58315E-03	X'
176	-1.50000E+00	6.50000E-01	2.00000E+00	-4.66282E+00	1.47025E+01	1.30000E+01	-5.75354E-04	-3.45725E-04	-4.73945E-04	Y'
177	6.36703E-01	2.73487E-01	4.36597E+00	-6.34424E-01	9.48923E+01	7.31035E+00	-1.18267E-03	-4.25451E-05	-1.04949E-04	N'
178	-1.50000E+00	6.50000E-01	2.00000E+00	1.00000E+01	5.15997E+01	1.00273E+01	-6.58231E-04	2.07299E-03	1.33898E-03	X'
179	1.50000E+00	8.34840E-02	5.00000E+00	1.38671E+00	6.48636E+00	7.93327E+00	-9.39990E-04	1.51904E-04	3.83027E-04	Y'
180	-1.22820E+00	5.29220E-01	2.11428E+00	-7.27855E+00	5.63986E+01	7.74492E+00	-9.21011E-04	-1.40767E-03	-1.90577E-03	N'
181	1.50000E+00	6.40000E-02	2.00000E+00	1.00000E+01	8.03117E+01	8.99300E+00	-9.55316E-04	3.86717E-03	1.29827E-03	X'
182	1.50000E+00	7.47540E-02	5.00000E+00	1.00000E+01	1.47025E+01	1.30000E+01	-5.74328E-04	1.14217E-03	9.32387E-04	Y'
183	-1.46480E+00	6.42118E-01	3.50323E+00	-9.71795E+00	4.23710E+01	6.45549E+00	-1.01683E-03	-2.06356E-03	-3.67561E-03	N'
184	1.50000E+00	6.50000E-01	5.00000E+00	1.00000E+01	2.98266E+01	8.69130E+00	-9.42493E-04	1.92296E-03	2.02554E-03	X'
185	1.50000E+00	6.40000E-02	2.00000E+00	4.52589E+00	1.00000E+02	7.34558E+00	-1.21902E-03	1.38921E-03	1.16826E-03	Y'
186	7.03894E-01	1.08415E-01	3.04757E+00	-4.90961E+00	1.82424E+01	1.23345E+01	-6.14029E-04	-3.54389E-04	-5.27102E-04	N'
187	-1.50000E+00	6.54090E-02	2.00000E+00	-1.00000E+01	4.67314E+01	1.30000E+01	-6.49625E-04	-1.37833E-03	-8.46421E-04	X'
188	-1.50000E+00	8.21860E-02	2.00000E+00	1.68340E+00	5.00000E+00	4.30000E+00	-2.78541E-03	2.29264E-05	1.49100E-03	Y'
189	8.67392E-01	5.60219E-01	4.67852E+00	2.91905E+00	8.66399E+00	1.02121E+01	-7.12636E-04	2.46135E-04	5.04893E-04	N'
190	-1.50000E+00	6.50000E-01	5.00000E+00	1.00000E+01	7.47104E+01	1.30000E+01	-3.88732E-04	1.04960E-03	9.40679E-04	X'
191	1.50000E+00	6.50000E-01	2.00000E+00	4.59122E+00	7.95184E+00	9.60422E+00	-8.55148E-04	4.91635E-04	8.54078E-04	Y'
192	-1.37169E+00	3.40099E-01	4.12650E+00	-4.43079E+00	7.74107E+01	1.24757E+01	-4.75201E-04	-2.99929E-04	-5.01458E-04	N'
193	-1.50000E+00	6.40000E-02	2.00000E+00	1.00000E+01	7.64505E+01	1.30000E+01	-5.45255E-04	2.09534E-03	7.00116E-04	X'
194	1.50000E+00	6.40000E-02	5.00000E+00	4.67976E+00	1.00000E+02	1.30000E+01	-4.41113E-04	2.99750E-04	4.88713E-04	Y'
195	1.24505E+00	3.89231E-01	2.19059E+00	-8.98225E+00	2.43343E+01	6.34308E+00	-1.07902E-03	-1.81041E-03	-3.54872E-03	N'
196	-1.50000E+00	6.40000E-02	5.00000E+00	1.00000E+01	7.71422E+01	7.15167E+00	-1.34004E-03	2.56797E-03	2.83406E-03	X'
197	1.50000E+00	6.40000E-02	2.00000E+00	-5.37459E+00	1.00000E+02	1.30000E+01	-4.57838E-04	-6.77912E-04	-4.74037E-04	Y'
198	4.81781E-01	3.77422E-01	4.46640E+00	-9.52380E+00	6.91593E+01	9.13845E+00	-6.31817E-04	-1.36114E-03	-1.77258E-03	N'
199	1.50000E+00	6.50490E-02	2.00000E+00	1.00000E+01	5.10146E+01	1.30000E+01	-4.54952E-04	1.53077E-03	8.14178E-04	X'
200	-1.50000E+00	7.47540E-02	2.00000E+00	3.29736E+00	1.47025E+01	1.30000E+01	-6.13547E-04	2.39103E-04	3.34304E-04	Y'